UNIVERSITÀ degli STUDI di CATANIA

DEPARTMENT OF ELECTRICAL ELECTRONIC AND COMPUTER ENGINEERING
PH.D. SCHOOL IN SYSTEMS ENGINEERING, ENERGY ENGINEERING, AND COMPUTER AND TELECOMMUNICATIONS ENGINEERING
CYCLE XXXVIII

Claudio Francesco Nicolosi

PHD THESIS

PROBABILISTIC AND STATISTICAL METHODS FOR STUDYING THE IMPACTS OF WEATHER AND CLIMATE CHANGE ON THE ADEQUACY OF POWER SYSTEMS

PhD Supervisor:
Prof. Giuseppe Marco Tina

PhD Coordinator:
Prof. Paolo Pietro Arena

Academic Year 2025/2026

Index

List of Figures

List of Tables

1. Energy-climate nexus

In recent years, increasing interest has been devoted to studying the relationship between energy production and demand and weather conditions. This is because, in electric power systems (EPS) there is a growing presence of plants whose production is directly linked to weather conditions, such as non-dispatchable renewable energy plants. Furthermore, over the past decades the effects of climate change on EPSs have already begun to be observed, which has attracted the attention of the scientific community to studies on the impact of climate on electricity production and demand. The following paragraphs introduce in detail this increasingly crucial topic in power systems, namely the energy–climate nexus.

1.1 The relationship between climate change and the ongoing energy transition in Europe

The World Meteorological Organization (WMO) defines climate as the average state of weather. More precisely, climate is the condition of the climate system described through relevant meteorological variables over a given reference period, which the WMO sets at 30 years [1]. The climate system is an interactive framework made up of five components: the atmosphere, hydrosphere, cryosphere, biosphere, and land surface, all of which are influenced by external forcings such as solar radiation and human activities [2]. On this basis, climate change is defined as a statistically significant shift in the mean state of the climate or in its variability. The most recent Intergovernmental Panel on Climate Change (IPCC) Sixth Assessment Report (AR6, August 2021) from Working Group I identified human influence on climate change as “unequivocal” [3] and introduced five new illustrative emissions scenarios compared with AR5.

Among human activities, power generation is one of the most critical drivers of climate change. In 2024, global energy-related CO_2 emissions reached 37.8 Gt [4]. At the same time, electricity demand continues to rise worldwide. However, according to the "Evolving Transaction" scenario, i.e., a scenario in which government policies, technology, and societal preferences continue to evolve in a manner and at a rate that has been observed in the recent past [5]. From the "Evolving Transaction" scenario point of view, the following remarks are of greatest relevance:

- Around three-quarters of total primary energy growth will be used for electricity generation, with the power sector absorbing about half of total primary energy by 2040;

- Nearly all future growth in electricity demand will come from developing economies, led by China and India, while Organization for Economic Co-operation and Development (OECD) countries will see slower growth due to more mature markets;
- The global electricity mix is shifting toward renewable energy sources (RES), which are gaining share at the expense of coal, nuclear, and hydropower. Natural gas is expected to remain roughly constant at about 20%. By 2040, two-thirds of the increase in electricity generation will come from RES, raising their share of the power sector to about 30%, while coal will decline and be overtaken by renewables.

Over the past two decades, global electricity generation from RES has been dominated by hydropower (4321 GWh in 2019), followed by wind (1412 GWh) and photovoltaics, PV, (693 GWh) [6]. This reflects the high capacity factors of hydropower plants (about 3653 h/y), compared with wind (2199 h/y) and PV (1241 h/y in 2019). While hydropower still leads, wind and PV are rapidly increasing their role.

In terms of installed capacity in 2024, global hydropower reaches 1425 GW, wind power 1132 GW and solar power 1865 GW; focusing on Europe, these capacity values amount to 225 GW, 269 GW (of which 36 GW offshore), and 338 GW, for hydropower, wind, and solar power, respectively [7]. It is noteworthy that in Europe the combined wind and solar capacity is three times that of hydropower. Moreover, considering the period from 2015 to 2024, the installed hydropower capacity in Europe experienced a growth trend of only 5%, while wind and PV capacity increased by 88% and 224%, respectively. This is because the available basins in Europe have already been largely exploited, and European energy transition policies have proven to be effective.

The downside of such a strong installation of new wind and PV capacity is that these technologies are non-dispatchable and are intermittent, meaning their output cannot be easily adjusted to follow demand and is subject to short-term variability. At the same time, climate change is a major driver of transformation in power systems. It affects both electricity demand and generation, conventional and renewable, by altering environmental conditions. For example, studies show that a +2 °C temperature increase would affect Europe’s electricity system more strongly than a +1.5 °C rise [8]. Climate models can help estimate future production and efficiency of power plants, but their projections carry significant uncertainty, which in turn influences assessments of reserve margins needed to ensure system adequacy.

Climate change would also be uneven across regions. The higher-latitude areas of the Northern Hemisphere are expected to experience larger climate variations, while Mediterranean regions are projected to warm about 20% more than the global average and suffer major reductions in precipitation. Regarding Italy, central and southern regions are likely to face more frequent summer droughts, whereas northern regions may see more intense winter rainfall without a corresponding increase in total precipitation. Overall, climate change is expected to increase the frequency, severity, and persistence of extreme weather events, already affecting the resilience and reliability of power systems [9]. Projections of temperature and precipitation depend strongly on the emissions scenario considered, with Shared Socioeconomic Pathways (SSPs) being among the most widely used frameworks for climate impact analysis [10].

Climate model projections can serve as inputs for power generation and electricity demand models, allowing the estimation of future generation profiles for different technologies and the corresponding demand patterns. These projections reveal that the impact of climate change on power generation varies geographically and depends on the type of generation technology. For instance, global warming is expected to increase the frequency and intensity of heat waves and droughts, which would affect thermoelectric generation more in southern Europe than in northern regions such as Scandinavia. Specifically for Italy, projections indicate a likely reduction in annual PV and wind energy generation, accompanied by a derating of thermoelectric plant efficiency. Such findings suggest that European Union (EU) energy policy should account for these regional disparities, promoting additional RES capacity where climate impacts are most severe, particularly in southern Europe.

Against this backdrop, power systems must adapt while considering cost reduction, energy security, reliability, resilience, and both local and global environmental objectives, particularly the reduction of greenhouse gas emissions. Modern power systems are inherently evolving, capable of integrating incremental changes in demand, technology, and consumer behavior [11]. The gradual replacement of conventional programmable generation, primarily thermoelectric plants, with non-programmable renewable sources such as wind and PV introduces new challenges for system adequacy and security. A power system is deemed adequate only if it can reliably supply electricity to meet demand in each hour across all market zones. In this context, the uncertainty associated with RES generation presents a significant challenge.

Climate change is expected to increase average temperatures worldwide, which can impact power system operations since several components are sensitive to ambient conditions. The effect varies by technology: transformers have maximum operating temperatures, and global warming could compromise their nominal operation. Higher temperatures also reduce the efficiency and output of thermoelectric plants, especially those using run-of-river cooling systems. Extended heat waves and droughts affect water availability, limiting hydropower and thermoelectric generation. Elevated temperatures can also decrease PV module efficiency.

Climate change will additionally alter electricity demand patterns. Air temperature is the most influential factor affecting demand, as it drives heating and cooling requirements in buildings, modifying both the magnitude and timing of electricity consumption. To quantify these impacts, researchers have applied both top-down approaches, which regress historical load against temperature or degree-days to estimate economy-wide demand, and bottom-up approaches, which use building energy models to estimate demand for specific sectors or building types. Combining these methods provides a more comprehensive assessment by capturing both macroeconomic and detailed thermodynamic effects [12]. Electricity demand varies seasonally, and the increasing use of electric heating and cooling amplifies this effect. Inter-annual variations in temperature further influence yearly demand profiles. The projected impact of climate change on electricity demand differs across countries, depending on macroeconomic factors and national developments in technology and energy efficiency. Overall, rising temperatures are likely to reduce seasonal electricity demand in autumn, winter, and spring, with this effect being more pronounced in northern than in southern Europe.

In 2019, the EU introduced the European Green Deal [13], an agreement among the 27 member states to achieve ambitious sustainable development goals. These include reducing greenhouse gas (GHG) emissions by 55% relative to 1990 levels by 2030 and reaching net-zero emissions by 2050, thereby achieving climate neutrality. The Green Deal policies are justified by the fact that in the EU, the energy supply and transport sectors are the largest contributors to CO_2 emissions [14].

If CO_2 emission intensity is defined as the ratio of CO_2 emissions from electricity generation to gross electricity generation [15], this intensity has declined significantly since 1990. By 2020, the CO_2 emitted per kilowatt-hour generated was roughly half of the 1990 level, largely due to extensive investments in and deployment of renewable energy sources. Between 2009 and 2019, the growth of renewables in the EU was mainly driven by PV, wind power, and solid biofuels [16]. Although hydropower capacity experienced only a slight increase during this period [17], in 2019 wind and hydropower together accounted for two-thirds of the total electricity generated from RESs [16]. The remaining third was produced by solar PV (13%), solid biofuels (8%), and other RES (9%). Notably, PV generation grew from 1% (7.4 TWh) in 2008 to 13% (125.7 TWh) in 2019, making solar PV the fastest-growing renewable technology in the EU-27.

Looking forward, the share of RES in electricity generation is expected to increase further to meet the EU's climate targets of net-zero GHG emissions by 2050. This growing penetration of renewable sources, while environmentally necessary, poses challenges for the safe and adequate operation of EPSs. To ensure a reliable, resilient, and economically sustainable electricity supply, it is essential to evaluate the interactions and impacts of climate change on power generation and demand and integrate them into planning and operational strategies.

Such assessments must account for significant uncertainties. Weather variables are inherently random, future climate conditions and projections are uncertain, and the phase-out of coal-fired plants alongside the growth of other generation technologies will affect GHG emissions (beyond CO_2) in ways that are not yet fully understood. Evaluating climate change impacts on future EPSs therefore requires considering the combined uncertainties of climate models, emission pathways, and intrinsic climate dynamics. Moreover, as seen above, the spatial variability of climate change impacts is significant: because climate change affects regions unevenly, analyses of EPS operation and planning must be performed on a country-by-country basis.

1.2 Influence of weather conditions on power systems

The energy production from RESs is strongly influenced by climate and weather variability, with both the magnitude and direction of these effects depending heavily on seasonal atmospheric conditions. Consequently, the impact of climate and weather on the adequacy of EPSs varies significantly across different seasons. The following provides a review of the relevant literature on this aspect of power systems.

In [18], the effects of inter-annual climate variability on the British EPS are analyzed. The study examines the sensitivity of electricity supply and demand in Great Britain using the installed wind power capacity as of 2016, omitting PV for simplicity. The response of the power system to climate variability is also evaluated under scenarios with higher wind power penetration. The results indicate that in a scenario with no wind power, inter-annual climate variability primarily affects peaking plants rather than baseload plants. In a scenario with 15 GW of wind capacity (in 2016), inter-annual climate variability begins to reduce mean baseload energy supply while increasing energy from peaking plants. This effect intensifies in scenarios with further wind capacity expansion. These findings suggest that increasing wind power supports decarbonization by reducing reliance on baseload plants such as coal but simultaneously increases the system's sensitivity to inter-annual climate variability, as the variability of baseload plant output grows. Including PV production could further refine these conclusions.

In [19], the daily variability of total power output from onshore wind and solar PV is studied with a focus on climatological factors rather than detailed EPS modeling. The correlated variability of solar irradiance and wind speed across different regions of Britain is examined. Using the Pearson correlation coefficient, the study finds that irradiance and wind speed are generally anticorrelated, with the magnitude of anticorrelation varying by region and season. By analyzing the joint distribution of irradiance and wind speed, the study highlights how PV and wind outputs can balance each other. Specifically, the results suggest that a solar PV-to-wind ratio of 70:30 reduces overall variability for all months. Exceeding this ratio could decrease variability in winter but increase it during summer. These studies underscore the importance of examining the impact of climate and weather on electricity generation at a seasonal scale, as the interactions between different RES technologies and atmospheric conditions can significantly influence system adequacy and reliability.

In [20], the authors evaluated the average effects of large-scale weather regimes on PV and wind energy production and electricity demand across Europe. Weather regimes, patterns of atmospheric circulation, affect surface weather conditions and thus influence both renewable energy output and electricity demand. Four regimes are considered: North Atlantic Oscillation positive (NAO+), NAO negative (NAO-), Scandinavian Blocking (SB), and Atlantic Ridge (AR). Focusing on inter-daily variability during winter, the study found that wind and PV production generally benefit from NAO+ and AR regimes, while NAO- and SB regimes have a negative impact on wind and PV production. Electricity demand tends to be higher during SB, NAO-, and AR regimes. Consequently, the residual load, that is the difference between demand and RES generation, is elevated during SB and NAO- events. These results reflect average effects, which smooth over high meteorological variability and energy production fluctuations within each regime. Extreme residual load events, however, are driven by rare circulation patterns and smaller-scale synoptic phenomena. Therefore, while large-scale weather regimes are useful for seasonal forecasting and EPS planning, higher-resolution meteorological analyses are necessary to capture extreme events and refine power system assessments.

In [21], the authors investigate episodes of extremely low renewable energy generation and extremely high residual load in European power systems, also considering their duration over 1, 7, and 14 days. Their results show that one-day events of very low renewable production mainly occur in autumn and winter (October to February), when persistent high-pressure systems dominate central Europe and 10 m wind speeds are lower than usual, reducing wind power output. Longer events lasting 7 or 14 consecutive days are associated with large-scale atmospheric blocking and tend to peak in late summer. As for extreme high residual load events, one-day episodes mainly take place from November to March, again under high-pressure conditions with weak winds, but combined with colder-than-average temperatures that increase electricity demand for heating. The combination of low renewable generation and high demand leads to very high residual loads. Similar to low-production events, high residual load events lasting 7 or 14 days are linked to blocking regimes. The authors also note that about one fifth of the selected events were characterized by both low renewable production and high residual load.

In [22], Marinelli et al. assess hourly wind and PV production forecasting at regional scale. Using two large-scale European models and mesoscale meteorological inputs, they estimate renewable generation while accounting for plant technology and spatial distribution. The simulated results are consistent with historical trends, although the authors highlight that the limited public availability of historical wind and PV generation data restricts more detailed validation. Overall, the literature shows that the growing share of RES in generation mixes makes it essential to quantify how weather and climate change affect the safety and adequacy of electric power systems. These impacts depend on plant location, seasonal conditions, and the proportion of non-dispatchable generation. From large-scale circulation patterns down to local phenomena such as breezes, electricity generation and demand are increasingly uncertain, requiring more stochastic approaches for future EPS planning. At the same time, planning must respect zero-emission targets, implying the replacement of thermoelectric plants with RES. This transition increases operational complexity and uncertainty in medium- to long-term planning.

As highlighted by the studies reviewed above, the growing share of RESs in generation mixes worldwide makes it essential to quantify how climate variability and climate change affect the safety and adequacy of EPSs. These impacts depend on several factors: the geographic location of RES plants (and thus the correlations among local weather variables), the season of the year, and the proportion of non-programmable generation in the mix. From large-scale circulation patterns down to local phenomena such as breezes, electricity generation and demand are increasingly difficult to predict, making stochastic approaches indispensable for future EPS planning.

At the same time, planning cannot ignore zero-CO_2 emission targets, which require the progressive decommissioning of thermoelectric plants and their replacement with RES. A higher penetration of RES increases the complexity of power system management, further exacerbated by the large uncertainties that characterize medium- and long-term planning and climate projections. One effective way to address operational issues such as system adequacy is to use stochastic analyses based on probabilistic models, for example, Monte Carlo simulations (MCS) with distributions such as normal or Weibull ones, which yield statistically robust results.

In this context, statistics becomes a key tool for managing the uncertainties inherent in future climate and energy scenarios. Reliable assessments of future power systems therefore cannot be separated from probabilistic methods. Finally, several of the cited studies show that sufficient storage capacity and reserve margins can mitigate, and in some cases eliminate, many of the critical issues in highly renewable systems. Once again, statistical analyses are essential to determine the amount of storage needed to ensure the adequacy, resilience, and safety of the power system.

1.3 How is climate change impacting and how will it impact power systems?

Recently, an increasing number of studies have addressed the impact of climate change on the planning and operation of power systems [12] [23], on the resilience of power systems [9] [24], on the electricity markets [25], and on the adequacy of a power system [26]. By evaluating the adequacy indices, the authors in [26] find that, due to rising temperatures, winter demand would decrease, and this should reduce the hours in which demand is not met. Looking instead at the effects of climate change on hydrological conditions, these are expected to increase the hours in which the system fails to meet demand.

In [27], the authors examined the impact of climate change on both the present-day (2021) and future Italian electric power systems, including electricity supply and demand. Drawing on a literature review, they assessed the adequacy of the Italian EPS using climate projections for Italy from previous studies, alongside future energy scenarios developed by Terna and Snam, the Italian transmission system operators (TSO) for electricity and gas. The study highlighted several key points: the magnitude and direction of climate-energy impacts vary depending on the generation technology considered (e.g., wind, PV, hydro, or thermoelectric); increasing the share of RES in the generation mix, coupled with adequate storage, could enhance system resilience to the effects of global warming; and the replacement of thermoelectric power plants, most sensitive to rising average temperatures [28], with RES would improve overall system performance. The study also emphasized that climate change impacts differ between Northern and Southern Europe, suggesting that EU energy policy should account for these regional disparities. Finally, the effects on future energy scenarios depend strongly on the SSPs used to force climate models.

To the author's knowledge, little has been written on the impacts of climate change on the adequacy of a power system. Moreover, the few articles that address the topic are limited to extracting generation plant unavailability profiles using Monte Carlo methods, without any probabilistic modeling of atmospheric variables and their impact on energy production and demand. The studies presented in this thesis therefore aim to fill this gap in the literature. The following sections explain what the adequacy of a power system is, which indices are used to calculate it, and the state of the art of adequacy analyses, before presenting specific studies in which statistical methods have been used to model the impact of climate change on energy production and demand. The final chapter then presents an algorithm for the stochastic generation of correlated time series of atmospheric variables.

2. Adequacy analysis in power systems

In this phase of the energy transition of European power systems, the issue of adequacy is taking on increasing importance. This is because, as seen in the previous chapter, on the one hand there is a strong penetration of non-dispatchable renewable energy sources (ND-RES) in European energy mixes, and on the other hand polluting but still dispatchable thermoelectric plants are being decommissioned. The various adequacy analyses of European TSOs increasingly show that in the coming years (2026–2035) there may be adequacy problems in different European market zones, where demand is not met due to a shortage of available capacity to cover load requirements.

This section explains what the adequacy of a power system is, which indices are used to quantify the level of adequacy of such a system, and which methodologies are used to evaluate these indices. It then investigates in the scientific and technical literature which aspects are modeled as impacting the adequacy of a power system.

2.1 The adequacy of a power system and the indices for quantifying it

The operation of an EPS goes beyond simply supplying electricity to users; it relies on a set of parameters and operating standards aimed at ensuring a safe, resilient, and reliable system. This thesis focuses on the adequacy of a power system and on the stochastic models used to assess this aspect of the EPSs.

Adequacy is defined as the ability of an EPS to meet electricity demand in each hour and in each market zone of a country using the available generation capacity [29]. To quantify the adequacy level of a given EPS, two main indices are commonly adopted: the Expected Energy Not Supplied (EENS), expressed in MWh, and the Loss of Load Expectation (LOLE) expressed in hours. These indices are evaluated annually in adequacy studies. The EENS is given by the following expression:

$$EENS = \frac{\sum_{k=1}^{n} ENS_k}{n} \tag{2.1}$$

Where k are the hours over which the EENS is calculated and ENS stands for Energy Not Supplied (MWh). In other words, equation (2.1) says that the EENS is the expected value of the ENS, which represents the portion of demand that is not met. If ENS is calculated for N different years, EENS is obtained as the average of those values [29]. The system is considered inadequate whenever ENS in the k-th hour is greater than zero, since ENS > 0 indicates that the load is not fully served in that hour. Once ENS is computed for every hour of a year, the total number of annual hours in which the system is inadequate is known. Taking the average of these hours over the years considered yields the LOLE. In fact, LOLE is calculated as the average number of hours in which ENS is greater than zero [29], as clarified by the following expression:

$$LOLE = \frac{\sum_{k=1}^{n} h_{ENS,k}}{n} \tag{2.2}$$

Where $h_{ENS,k}$ represents the k-th hour in which ENS > 0 occurred, and n is the number of hours in which the demand is not satisfied.

Equations (2.1) and (2.2) are those through which the Italian TSO Terna, the various national TSOs of the EU, together with the European Network of Transmission System Operators for Electricity (ENTSO-E), assess adequacy. At the European level, LOLE can also be evaluated using an alternative expression based on economic parameters, namely the Cost of New Entry (CONE, in €/MW), which represents the cost of additional generation capacity required to ensure adequacy, and the Value of Lost Load (VOLL, in €/MWh), which reflects the economic value of unserved energy [30], according to the following expression:

$$LOLE = \frac{CONE}{VOLL} \tag{2.3}$$

Italy, like many others EU-27 countries, sets a target level of adequacy considered acceptable for proper EPS operation. This target level was set by ministerial decree at $LOLE = 3\ h$. This threshold is intended to represent the fact that, for a market zone in Italy, or the Italian power system as a whole, to be considered adequate, the expected number of hours in which demand is not satisfied must not exceed three. Therefore, the Italian TSO, Terna, in its adequacy studies seeks to understand whether simulations for the coming years provide expected values of hours of unmet demand that are lower or higher than three. If the simulations show LOLE values above the ministerial threshold, an adequacy problem is identified and actions to address this issue are suggested and subsequently implemented.

2.2 State of the art of adequacy assessments in Italy and Europe

In the literature, several studies help clarify how adequacy analysis is evolving and what results have been achieved so far. In [31], the authors assess adequacy in power systems with high wind power penetration. They present and apply wind speed data models and wind energy conversion system models to evaluate the adequacy of wind-integrated power systems in two case studies, again using Monte Carlo techniques. The role of energy storage as a mitigation measure for the variability of wind generation is also analyzed.

In [32], a Monte Carlo approach is used to estimate system adequacy under different levels of RES penetration (from 0% to 100%) and for various mixes of wind and PV installed capacity. The authors find that, as conventional generation is decommissioned, increasing RES shares can compromise system adequacy. They therefore examine the contribution of storage technologies, in particular pumped-hydro storage, under different combinations of conventional and RES capacities. Their results show that storage can restore or at least improve adequacy even in scenarios with strong reductions in conventional generation. Several case studies are carried out on a simplified model of the eastern Australian interconnected power system, and the methodology includes the use of availability curves for conventional generating units.

In [33], the authors examine generator failures in the context of resource adequacy. Starting from hourly time series of full availability histories for generating units, they investigate whether failures across different units are correlated and whether outages exhibit seasonal patterns. Their results show that, in most regions, outages of different units are indeed correlated, while no clear seasonal structure is detected (although the authors do not rule out that such a pattern could exist). They also characterize the statistical distributions of unscheduled unavailable capacity, modeled with Weibull and lognormal laws, and of unscheduled derating magnitudes, and they estimate key reliability metrics such as the mean time between failures (MTBF) and the mean time to repair (MTTR). In terms of MTBF, significant differences are found between small and large units across three generation technologies. The authors therefore conclude that correlated outages should be explicitly considered to ensure realistic adequacy and reliability reserve assessments.

The studies reviewed above follow the probabilistic approaches adopted by national TSOs, reinforcing the importance of statistical tools in adequacy analysis. They also show that adequacy is largely driven by the level of reserve margin: the higher the reserve margin in an EPS, the greater the likelihood of maintaining adequacy. At the same time, several works emphasize the role of storage in achieving acceptable standards of adequacy. While increasing RES capacity is essential to reduce

CO_2 emissions, a power system with high RES penetration cannot be reliably operated without a sufficient amount of storage capacity to balance variability and uncertainty.

European TSOs carry out their adequacy analyses by referring the results to the respective adequacy standards set by each country. The methodologies implemented for calculating EENS and LOLE tend to align with those applied at the European level by ENTSO-E. Specifically, the adequacy study conducted by ENTSO-E follows the guidelines of the European Union Agency for the Cooperation of Energy Regulators. Each year, ENTSO-E is tasked with carrying out its adequacy analyses of the interconnected European power system, providing EENS and LOLE index results for each market zone of the interconnected EU-27 electricity system. This adequacy study is called the European Resource Adequacy Assessment (ERAA), and the most recent one just completed is ERAA 25.

In ERAA 25, adequacy indices are evaluated using a Monte Carlo algorithm. Through probabilistic methods, plant availability profiles are derived, thus modeling unplanned outages using probability curves. To account for the influence of climate on adequacy, no probabilistic processing is performed; instead, data from climate projections of three climate models are directly considered, under a given emissions scenario forcing. A basket of several years of climate projections is therefore created. In implementing the Monte Carlo method, Monte Carlo samples are generated. These samples represent a simulation of the state of adequacy of the European system over one year. Each sample is obtained by stochastically generating an annual availability profile of the generation plants and randomly drawing one of the years of climate projection data. This yields a Monte Carlo sample year, for which ENS and the number of hours with ENS > 0 are evaluated. This procedure is repeated for several dozen Monte Carlo simulations, and at the end the ENS and the number of hours with ENS > 0 are averaged, yielding the EENS and LOLE values for each explicitly modeled market zone of the EU-27 European power system. This Monte Carlo methodology is the same as the one used by Terna, the Italian TSO, in its national adequacy report.

2.3 The stochastic simulation of climate change impacts on the adequacy of an EPS

As observed in the previous paragraphs, adequacy analyses consist of stochastic simulations of energy generation and demand scenarios for the purpose of evaluating adequacy indices. Specifically, as reported in 2.2, it is noted that there is no methodology for the stochastic simulation of climate change impacts on adequacy. In other words, in the scenarios of adequacy analyses, climatic conditions that may occur according to a probability-based logic are not simulated stochastically. Instead, historical data or climate projections for certain years are directly considered to simulate the climate in the coming years for the evaluation of adequacy indices for those years. To the author's knowledge, no one in the scientific literature, nor in the technical methodologies of TSOs, has considered simulating climate scenarios using statistical methods, thereby evaluating the impact of multiple stochastic climate scenarios on the values of adequacy indices obtained from the analyses.

Not treating atmospheric variables with stochastic methods deprives adequacy analyses of the ability to simulate the randomness of the impacts that these variables have on electricity generation and demand, as well as on grid infrastructure (lines and transformers). Moreover, considering either historical data or only a few climate projections risks, in practice, not simulating weather scenarios with extreme conditions. For example, as seen in Section 1.3, rising temperature trends imply a higher probability of heatwave periods, which strongly impact: electricity demand (summer peaks keep increasing), transformer windings and power lines (stress on insulation integrity), and energy production (wind droughts or prolonged dry periods).

Considering what has been said above, the importance of simulating the impact that climatic conditions have on the simulated hourly values of electricity generation and demand becomes clear. It is also understood that, since climate evolution is intrinsically uncertain and given the inter-seasonal and inter-annual variability of atmospheric variables, statistical methods must be used to simulate the impact of climate on the adequacy of an EPS.

The studies presented in this thesis therefore focus on the use of statistical methods for the analysis and simulation of the impacts of weather and climate change on energy generation and demand, also considering grid elements such as transformers. In the following section (Chapter 3), the statistical methods implemented are presented in detail, and the subsequent chapters are each devoted to aspects concerning energy generation (Chapter 4), grid transformers (Chapter 5), energy demand (Chapter 6), and the simulation of climate scenarios for the purpose of evaluating adequacy indices (Chapter 7). This is followed by a final Conclusions chapter (Chapter 8).

3. Mathematical tools for data analysis and stochastic simulations

As reported in the previous chapters, adequacy analyses are conducted using statistical methods. In this thesis, statistical techniques and stochastic approaches are applied to assess the impacts of climate on electricity production and demand, and thus on the adequacy of an EPS. For this reason, this chapter presents the statistical methods on which the analyses and simulations carried out in the various studies addressed in the thesis are based. Specifically, the following sections first present the theoretical foundations of correlation analysis and then describe in detail Monte Carlo algorithms for the stochastic generation of profiles of random variables. In the specific case of the analyses carried out and reported in this thesis, correlation analysis is performed on atmospheric variables and their relationship with electricity demand, while Monte Carlo algorithms are implemented for the simulation of energy yields as well as for the generation of synthetic profiles of atmospheric variables, both independent and correlated. The following sections describe in detail the methods adopted.

3.1 Correlation analysis

Often in statistical analyses the aim is to understand whether there is some relationship between two data series. In the medical field as well as in engineering, this involves both a qualitative observation of the data and subsequent quantitative analyses of the degree of relationship between the variables considered. The first step of a correlation analysis in fact starts from the visual inspection of scatter plots, which provide the examiner with an initial idea of whether there is inter-variability between the variables considered and whether such a relationship is linear or not.

However, limiting the analysis to the observation of scatter plots does not make the correlation analysis complete and only allows for qualitative inferences. Moreover, sometimes scatter plots do not show a clear pattern in the relationship between the pairs of variables considered, which can lead to misleading conclusions. For these reasons, the analysis of scatter plots must be complemented with indices that can quantitatively describe the degree of relationship between the variables considered.

In the literature, several indices are used to investigate the correlation between variables, but these are modified versions of the best-known parametric and nonparametric correlation indices, namely the Pearson, Spearman, and Kendall correlation coefficients. In the studies presented in this thesis, Kendall’s coefficient is not used, as the analysis is carried out on “pure” continuous data that do not have ranks to which Kendall’s coefficient can be applied. Regarding the Pearson and Spearman coefficients, in previous studies conducted by the author (not reported in this thesis), it was observed that the evaluation of the degree of correlation between atmospheric variables yielded similar results when using these two correlation indices [34]. This is noteworthy, as the Pearson coefficient requires normality of the variables considered and a linear relationship between them, assumptions that are not required by the Spearman coefficient. In light of this evidence, in most of the studies in this thesis, the Pearson coefficient is used, and only occasionally the Spearman coefficient. The next section reports in detail the mathematical formalism on which the correlation analyses are based.

3.1.1 The sample correlation coefficient

Given two random variables X and Y, the degree of linear relationship between them is expressed through the population correlation coefficient ρ, given by the following expression [35]:

$$\rho = \frac{Cov(X,Y)}{\sigma_X \sigma_Y} \tag{3.1}$$

Where $Cov(X,Y)$ is the covariance of X and Y, and σ_X and σ_Y are the standard deviations (STDs) of populations X and Y, respectively.

$Cov(X,Y)$ is given by the following expression:

$$Cov(X,Y) = E[(X-\mu_X)(Y-\mu_Y)] \tag{3.2}$$

Where E is the expected value, μ_X is the average of population X, and μ_Y is the average of population Y. μ_X and μ_Y are given by the following expressions:

$$\mu_X = E[X] \quad , \quad \mu_Y = E[Y] \tag{3.3}$$

Through (3.3), (3.2) gives the following expression for the covariance:

$$\begin{aligned} Cov(X,Y) &= E[(X-E[X])(Y-E[Y])] = \\ &= E\big[XY - XE[Y] - YE[X] + E[X]E[Y]\big] = \\ &= E[XY] - E[X]E[Y] \end{aligned} \tag{3.4}$$

σ_X and σ_Y are instead given by the following expressions:

$$\sigma_X = \sqrt{E[(X-\mu_X)^2]} \quad , \quad \sigma_Y = \sqrt{E[(Y-\mu_Y)^2]} \tag{3.5}$$

The expressions from (3.1) to (3.5) refer to the populations of the random variables X and Y, which are defined over infinite samples. The values of ρ, μ_X, μ_Y and σ_X, σ_Y are unique but not observable. For statistical analysis, one therefore extracts samples from the populations of X and Y and evaluates the sample statistics of interest. Therefore, instead of evaluating ρ, the sample correlation coefficient r is evaluated; instead of the population STD, the sample STD s is used; and instead of the population expected value, the sample mean m is considered.

Let the elements x_i and y_i of the populations X and Y be considered, and the pairs of points (x_1, y_1), (x_2, y_2), …., (x_n, y_n). From these, the sample means m_x and m_y, as well as the sample STDs s_x and s_y, can be evaluated through the following expressions:

$$m_x = \frac{1}{n}\sum_{i=1}^{n} x_i \quad , \quad m_y = \frac{1}{n}\sum_{i=1}^{n} y_i \tag{3.6}$$

$$s_x = \frac{1}{n-1}\sqrt{\sum_{i=1}^{n}(x_i - m_x)^2} \quad , \quad s_y = \frac{1}{n-1}\sqrt{\sum_{i=1}^{n}\left(y_i - m_y\right)^2} \tag{3.7}$$

In the studies conducted in this thesis, time series of climate data and power system operation (demand profiles) are considered, with a dataset size large enough (N > 30) to regard the sample statistics values as very close to the population statistics values. One implication of this consideration is that the impact of Bessel's correction becomes negligible in the evaluation of the sample standard deviation. Nonetheless, this correction is still applied as a precaution.

After evaluating the sample means and standard deviations with (3.6) and (3.7), each x_i and y_i can be converted into standard units, i.e., the z-scores are computed using the following expressions [36]:

$$\frac{x_i - m_x}{s_x} \quad , \quad \frac{y_i - m_y}{s_y} \tag{3.8}$$

Mathematically, the correlation coefficient is the arithmetic mean of the products of the z-scores [36]:

$$r = \frac{1}{n-1}\sum_{i=1}^{n}\left(\frac{x_i - m_x}{s_x}\right)\left(\frac{y_i - m_y}{s_y}\right) \tag{3.9}$$

By substituting (3.7) into (3.9), the well-known expression for the Pearson sample correlation coefficient is finally obtained:

$$r = \frac{\sum_{i=1}^{n}(x_i - m_x)(y_i - m_y)}{\sqrt{\sum_{i=1}^{n}(x_i - m_x)^2}\sqrt{\sum_{i=1}^{n}(y_i - m_y)^2}} \tag{3.10}$$

The key aspect of expression (3.10) is that the value of r is dimensionless. This allows the results of the correlation analysis to be compared even when considering pairs of variables that are different physical quantities. Moreover, (3.10) shows that the linear correlation coefficient is normalized, specifically taking values within the range $[-1, 1]$, which facilitates the interpretability of the results. $r = 1$ indicates a perfect positive linear correlation between the pairs of variables (x_i, y_i) considered, meaning that as one variable, e.g. x_i, increases, the other variable also increases. Similarly, if x_i decreases, y_i also tends to decrease. $r = -1$ indicates a perfect negative linear correlation (anticorrelation) between the pairs of variables (x_i, y_i), meaning that as one variable, for example x_i, increases, y_i tends to decrease, and vice versa. $r = 0$, on the other hand, indicates that there is no evidence of a linear correlation between the pairs (x_i, y_i) considered. This latter fact does not imply that x_i and y_i are not related at all by some other law; indeed, if the relationship were quadratic, the coefficient r would not reveal it.

Correlation analysis is, in any case, a statistical test and, as such, is based on hypotheses that are tested each time a correlation analysis is performed. Specifically, the null hypothesis, H_0, assumed in this thesis is that there is no correlation between the variables considered, while the alternative hypothesis, H_1, states that there is a correlation between the variables considered. H_0 is rejected when the p-value is below the significance level set here at 0.05. The Student's t-test is used to test the null hypothesis. Specifically, the t statistic, which follows a Student's t distribution with n−2 degrees of freedom, is evaluated using the following expression [36]:

$$t = \frac{r\sqrt{n-2}}{\sqrt{1-r^2}} \tag{3.11}$$

Where n is the sample size. Knowing the value of t, the p-value can then be evaluated, allowing one to determine whether or not to reject H_0.

It is important to emphasize that correlation does not imply causation [37]. Indeed, while it is true that two variables intrinsically linked by a cause-effect relationship will exhibit a certain degree of statistical correlation, the converse is not always true. In other words, the fact that two variables are correlated does not necessarily imply that there is a cause-effect relationship between them. In mathematical terms, statistical correlation is therefore a condition necessary but not sufficient for the interdependence of two variables.

Finally, there are no universal threshold values that objectively separate “strong” from “weak” correlations. The interpretation of r must therefore be context-dependent and supported by domain knowledge and complementary analyses [38].

3.1.2 Applications of correlation analysis in the EPS domain

Understanding the relationships among meteorological variables is important not only from a scientific perspective but also from a technical one. Knowing how one atmospheric parameter is statistically linked to another makes it possible to improve models that simulate the effects of climate on energy production and demand. In addition, analyzing the degree of linear dependence between variables helps to assess the complementarity of different generation technologies.

For instance, if over a year or during a given season in a specific region air temperature and wind speed are found to be negatively correlated, this offers system operators useful information on how wind and photovoltaic generation may complement each other. This, in turn, supports more accurate evaluations of the reserve capacity required to keep the EPS secure and adequate. When climate projections are considered, information on correlations further strengthens their interpretation and statistical relevance. Saying that two variables are positively or negatively correlated means that an increase in one raises the likelihood that the other will increase or decrease, respectively. Therefore, if future temperatures are expected to rise, inferences can be drawn about how other correlated meteorological variables may evolve. Since both electricity demand and generation depend on multiple atmospheric drivers, understanding the interdependence among atmospheric quantities allows better insight into the balance between production sources and load, for present and future EPSs.

In the literature, extensive research has examined the relationships between meteorological variables and economic, social, and health-related phenomena [39, 40, 41]. By contrast, far fewer studies have focused on the correlations among meteorological variables themselves [42, 43]. Within the context of adequacy analyses for EPSs, it has also been shown that explicitly modelling the correlation structure of weather variables can significantly influence the results of statistical simulations [44].

Studying the correlation between atmospheric variables has important implications for the adequacy analysis of an EPS. In fact, the degree of linear dependence between the variables also reveals the degree of complementarity among the generation sources that depend on those atmospheric variables. Within the framework of this thesis, the correlation analysis of atmospheric variables takes on an additional fundamental role. Indeed, following the correlation analysis, the related results are used as inputs for the stochastic generation of correlated time series of atmospheric variables. Overall, within the studies presented in this thesis, correlation analysis has been used to understand the degree of relationship between electricity demand and air temperature during periods of extreme heat, as well as the interdependence of offshore wind production at certain case-study sites, and finally for the stochastic generation of correlated profiles of atmospheric variables, as mentioned above.

3.2 Monte Carlo methods for the generation of synthetic profiles of atmospheric variables

As seen in Chapter 2, the Monte Carlo method is used in adequacy analyses to evaluate the EENS and LOLE indices. However, in the implemented Monte Carlo algorithms, plant availability profiles are drawn using probability distributions, whereas this probabilistic approach is not applied to the atmospheric variables of interest. In the studies presented in this thesis, a Monte Carlo methodology is therefore proposed for the stochastic generation of time series of atmospheric variables. This stochastic generation is carried out both by considering the atmospheric variables as independent from each other and by considering the degree of correlation between them. The following paragraphs detail the Monte Carlo methods used to stochastically simulate the impact of weather and climate change on the adequacy of a power system.

3.2.1 Stochastic approach for the generation of independent time series of atmospheric variables

Stochastic analyses can begin with the statistical characterization of the probability distributions of the relevant meteorological variables for EPS operation. For adequacy analyses, the variables of primary interest are global solar radiation, precipitation, air temperature, and wind speed. In power system studies, an alternative to using historical weather records directly is the synthetic generation of meteorological time series. This approach is particularly useful for producing statistically meaningful medium- and long-term scenarios through probabilistic and stochastic models. It is also advantageous when weather stations provide incomplete or short data records, which is often the case when long-term analyses are required.

In the literature, several approaches are used for the stochastic generation of synthetic profiles of atmospheric variables, which vary depending on the specific variable considered. For global solar radiation (GSR), [45] presents a model for generating daily solar radiation data based on a simple trigonometric function with a single independent variable: the day of the year. This approach is particularly suitable for developing regions or for weather stations without access to complex and costly measurement equipment. After validating the model statistically, the authors show that its outputs are consistent with both historical observations and values reported in the literature. A different method for producing synthetic daily solar radiation data relies on artificial neural networks (ANNs) [46]. In this case, daily GSR is generated using a model that combines meteorological reanalysis data with ANN techniques. The network inputs include four reanalysis-based meteorological variables, together with site latitude and longitude, daily clear-sky global radiation, and the day of the year. The sole model output is daily global solar radiation. One limitation of this approach is its sensitivity to spatial distance and cloud cover. An alternative strategy is described in [47], where two statistical models are proposed to generate hourly global radiation profiles, from which hourly temperature series are then derived. One method is based on fitting probability distribution functions to the data, while the other relies on clear-sky solar radiation. These models are intended for medium- to long-term studies of EPS adequacy and resilience.

Regarding precipitation (Pr), the most common method to generate daily rainfall data is a two-step model combining a first-order Markov chain with a gamma distribution. The Markov chain typically uses two states: dry-to-wet day and wet-to-wet day. Transition probabilities are calculated for a wet day following another wet day and for a wet day following a dry day. The gamma distribution is then used to simulate rainfall intensity, with two parameters, α and β. Parameter α is dimensionless, usually less than one, and represents low rainfall events, while β (mm), greater than one, models extreme rainfall for the given environment [48]. A limitation of this approach is the need for long-term daily rainfall records to calibrate the model. To address this, [48] proposed using monthly summaries instead of daily values to estimate the parameters, justified by empirical relationships between monthly averages and model parameters. However, another limitation is that the gamma distribution captures short-term rainfall variability well but underestimates long-term variability and extreme events, due to its tendency to underestimate the standard deviation of rainfall and the heavy precipitations [49]. Some studies have attempted to overcome the modeling limitations mentioned above by increasing the order of the Markov chain. The authors of [50] explored second- and third order chains but found that higher-order chains increase model complexity without significantly improving results compared to the first-order chain. This conclusion is supported by [51], who observed only minor improvements in long-term variability when using a second-order chain.

Focusing on air temperature, in [47], the authors generate hourly temperature profiles using a physical model, producing simulated temperature data closely matching measured values. An analysis of persistence shows no direct correlation between consecutive clear or cloudy days, nor between consecutive days with low or high temperatures, throughout the year. Additionally, a statistical model for irradiance persistence is used, showing that both methods can simulate extended sequences of clear days; however, the probability distribution–based approach fails to reproduce long sequences of cloudy days. The method used to generate hourly temperature profiles also cannot simulate consecutive days with unusually high or low temperatures. In [52], the authors compare theoretical models for temperature prediction found in the literature and propose a semi-empirical model to capture ambient temperature variations, using minimum and maximum daily temperatures combined with Lagrange interpolation.

Regarding wind speed, in [53] the authors present techniques for generating synthetic wind speed data. They compare a nonparametric wavelet transformation method with parametric approaches, including independent random numbers following normal and Weibull distributions, first- and second-order autoregressive (AR) models, and first-order Markov chains. The normal and Weibull distributions generate independent and identically distributed (i.i.d.) random numbers, while AR models produce time series that incorporate the correlation structure. Markov chains generate wind speed data with a predefined distribution, preserving the autocorrelation of the series. The authors conclude that the wavelet method is most effective for maintaining the correlation structure of the time series. An alternative approach is proposed in [54], where the authors develop a method based on four parameters that control persistence and autocorrelation in the generated time series. These parameters are determined by minimizing a multi-objective function using a stochastic optimization algorithm. The function depends on the number and type of input data, leading the authors to test the method in three case studies with different input sets. The model's validity is further tested for two Italian locations—one onshore and one offshore—by comparing the generated wind speed data to measured data, considering both statistical characteristics of the time series and the kinetic energy available to a generic wind turbine.

From this brief literature review, it can be observed that none of the studies used a Monte Carlo approach based on the inverse method for the generation of synthetic profiles of atmospheric variables. Moreover, some studies generate daily synthetic series, while others produce hourly synthetic series. The choice of time resolution for synthetic profiles generally depends on the resolution of the available historical data; when only daily datasets are available, generating synthetic hourly profiles can result in coarse approximations. Furthermore, the suitability of a synthetic generation method often depends on the specific weather variable considered. Some variables, such as GSR, have a strong deterministic component that cannot be accurately captured by purely statistical approaches. Overall, methods that combine both physical and statistical elements tend to provide the most reliable results for modeling synthetic weather time series. Considering all of the above, the inverse method is here introduced for the first time in the literature (to the author's knowledge) as a Monte Carlo method useful for the stochastic generation of synthetic profiles of atmospheric variables. In this thesis, synthetic hourly time series of GSR, Pr, ambient temperature, and wind speed are independently generated, on a seasonal basis to simulate the weather and climatic seasonal variabilities.

To generate synthetic hourly GSR profiles, a combination of inverse and bootstrap methods is used. Among the weather variables considered in this thesis, solar radiation is the one with the strongest deterministic component. In fact, the alternation between daylight and nighttime hours, together with the seasonal cycle, is governed by the Earth's rotation and revolution. These processes introduce a deterministic structure into hourly solar radiation profiles that cannot be reproduced by a purely statistical model and must therefore be included explicitly in the final synthetic series.

For this reason, zero values are removed from the historical GSR time series, since night-time hours are fixed deterministically and cannot be sampled at random. In addition, to remove the deterministic annual solar cycle from the historical data, the clearness index from the Liu & Jordan model [55] is used. Fitting historical irradiance data (with or without zero values) with a theoretical probability density function (PDF) leads to poor results in terms of goodness of fit (GOF). To overcome this issue, the clearness index dataset can be considered and, together with the historical global irradiance data, the experimental cumulative distribution function (CDF) is derived. Random values in the interval (0,1) are then extracted and used as inputs for the experimental inverse CDF (ICDF). Finally, the bootstrap method is then applied to these synthetic time series thus obtained, yielding synthetic hourly series of global solar radiation. This procedure is repeated for each season.

For the generation of synthetic precipitation profiles, a Monte Carlo method based on random sampling from a Pearson distribution is adopted. This approach relies on generating values according to the Pearson distribution, using the mean, standard deviation, skewness, and kurtosis of the historical rainfall data as inputs. In this way, the Pearson-distributed random numbers are mapped onto physically meaningful rainfall values.

For the generation of synthetic air temperature and wind speed profiles, suitable theoretical probability density functions can be fitted to the historical data for both variables; therefore, the inverse transform method is applied. The first step consists in fitting theoretical PDFs to the available meteorological dataset. Among all the PDFs, the one that provides the best GOF is selected. From this winning PDF, the corresponding CDF is easily derived, and consequently the ICDF. Then, random numbers in the interval (0,1) are generated according to a uniform distribution and used as inputs to the ICDF. In this way, synthetic time series of air temperature and wind speed are obtained.

The atmospheric variables generated using the stochastic approaches described are, however, independent of each other. Physical reality, however, shows that atmospheric variables are correlated, so it would be more realistic to generate mutually correlated atmospheric time series. Moreover, this modeling refinement can provide more realistic analyses of the climate impacts on the adequacy of an EPS. The following section outlines the stochastic approach implemented for the correlated synthetic generation of the atmospheric variables considered so far.

3.2.2 Stochastic approach for the generation of correlated time series of atmospheric variables

The first step for the synthetic generation of correlated time series of the atmospheric variables discussed above is the correlation analysis of the historical hourly joint distributions of the weather variables. This analysis is carried out on a seasonal basis and for each market zone of which an EPS is composed. Through the correlation analysis, the sign and the degree of linear dependence between the pairs of variables considered are thus determined, with the hypotheses and significance level as defined in Section 3.1.1.

Once the correlation coefficients are determined, synthetic correlated weather time series can be generated. To this aim, two methods could be applied, as described in [56] and [57]. The approach adopted in this thesis begins with the independent synthetic generation of two weather variables. The results of the correlation analysis are then used to construct correlated marginal distributions of random numbers drawn from a multivariate Gaussian distribution. In this way, the sign and magnitude of the correlations of these new marginals reproduce those obtained for the original weather variables. Finally, these correlated random numbers are mapped onto the marginal distributions of the original variables, yielding synthetic weather series that are correlated with each other. This method is general and can be applied even when the CDFs and their inverses are experimental rather than theoretical, providing great flexibility in handling both experimental and analytical distributions. Figure 3.1 shows a flowchart that schematically outlines the steps of the stochastic approach just described.

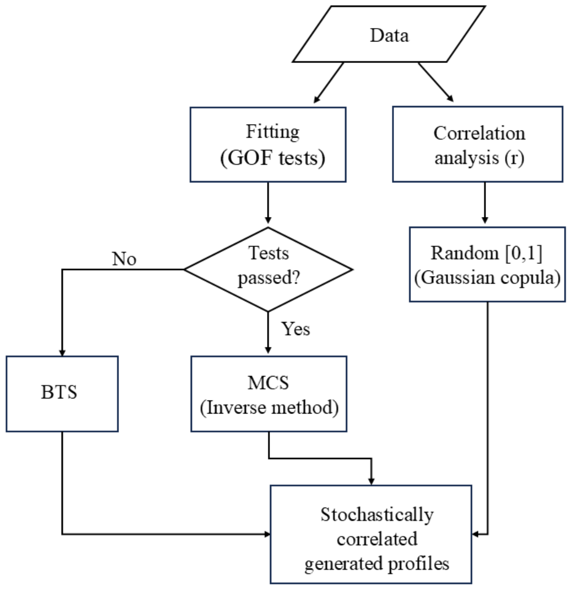

Figure 3.1. Block diagram of the procedure used to stochastically generate hourly profiles of correlated atmospheric variable pairs.

When the marginal distributions of the weather variables can all be described by theoretical CDFs, a second method, not adopted here, can be used. In this case, a multivariate normal distribution is first employed to generate intercorrelated random numbers based on the correlation structure inferred from the data. The CDF of the multivariate normal is then used directly to produce correlated realizations of the original weather variables. This approach requires that the fitting PDFs be theoretical, since their parameters must be specified explicitly. Compared with the first method, the second does not require an initial independent generation of weather variables, but it is limited to cases where theoretical CDFs are available.

To assess the quality of the correlated synthetic series, the centroids (expected values) of the historical and synthetic joint distributions can be computed and the distances between them are evaluated. In addition, as further evidence of the validity of the approach used, two regression analyses are conducted: one for the historic joint distribution and the other for the synthetic joint distribution, with the aim of evaluating the respective R^2 coefficients. The purpose of assessing these coefficients is to understand, from their comparison, how well the implemented algorithm performs. The closer the R^2 values are, the more the algorithm has produced synthetic profiles with a degree of correlation close to that of the physical reality. For these regression analyses, third-degree polynomials are considered, as they provide a good compromise between a linear polynomial and a higher-order polynomial, which would be particularly complex. Moreover, evaluating the coefficients of determination has a further implication in terms of analyzing the interdependence between variables. Indeed, since R^2 quantifies how much of the variability of the output variable is explained by the input variables, R^2, together with the Pearson correlation coefficient r, quantifies the degree of relationship between the atmospheric variables.

4. Studies on the effects of weather and climate change on non-dispatchable renewable plants

In European power systems, an energy transition is underway that is based on PV and wind power plants. Such plants can be defined as non-dispatchable since their output cannot be scheduled in advance, as it depends on the variability of atmospheric conditions. As mentioned earlier, the climate-energy nexus is bidirectional. It is therefore interesting to study how weather and climate change impact and will impact the production from ND-RESs, and how these plants can serve as a solution for mitigating climate change. The following chapters therefore address both how ND-RES plants can mitigate the impacts of climate on energy production (Chapter 4.1) and how climate change would likely affect the production of a specific ND-RES technology (Chapter 4.2).

4.1 Effect of floating photovoltaic modules on evaporation rates of two water reservoirs

In the context of global warming, which is progressively increasing aridity in several regions of the world [58], including the Mediterranean basin [59], the assessment of evaporation rates from natural and artificial reservoirs is becoming increasingly important. Within electric power systems, water management plays a critical role in energy production, both for plants that directly exploit water as a primary energy source, such as hydroelectric facilities, and for those that rely on water for cooling purposes, such as thermoelectric plants [60]. Consequently, studies aimed at reducing water losses due to evaporation have not only environmental relevance but also significant technical and energy-related implications.

Among the strategies adopted to mitigate water evaporation from reservoirs, one widely investigated approach involves partially covering reservoir free surfaces using specific materials and coverage ratios. In the power generation sector, floating photovoltaic (FPV) systems have emerged as a promising solution, as they cover reservoir surfaces, reduce water evaporation [61], and at the same time they produce renewable energy [62]. Moreover, the cooling effect of evaporation on FPV systems would lead to a 3% to 6% increase in energy yield compared to land-based PV systems [63].

Since its first installation in 2007, FPVs has expanded at an average annual growth rate of 132% over the past 15 years, reaching a cumulative installed capacity close to 6 GWp by the end of 2022, with 59 countries having at least one FPV installation [64]. Since 2013 the median capacity of FPV systems increased from 0.09 MWp to 1.40 MWp in 2022, and the median power density has risen from 82 W/m^2 to 123 W/m^2 by 2022 [64]. Currently, research on FPV float designs and materials is ongoing, especially for offshore settings, where high waves, strong winds, and saltwater pose significant challenges. Offshore floating platforms are still nascent, with numerous stakeholders developing, testing, and enhancing pilot and small-scale installations. A 2021 NREL survey [65] found that the CAPEX for 10 MWp and 50 MWp FPV systems is 1.29 and 1.05 USD/Wp, roughly 25% higher than for ground-mounted PV. The increase is mainly due to the cost of floats and anchoring systems. While FPV benefits from lower installation costs because it requires less heavy machinery than ground-mounted PV, the expense of floats, ranging from 0.2 to 0.4 USD/Wp for US-manufactured units, pushes the overall CAPEX upward. Moreover, CAPEX is highly sensitive to float costs, which depend on factors such as wind and snow loads, as well as panel efficiency [64]. Making a further comparison between FPV and land-based PV (LPV) systems, with a focus on the Mediterranean climate, the authors in [66] reveal that FPV deployment at a tilt of 10° reduced evaporation by 83%, and at a tilt angle of 20°, FPVs outperform the power output of an LPV by 9%.

Considering inland reservoirs, assuming that only 10% of the reservoir area would be covered by an FPV system (a conservative estimate of the global FPV potential), and assuming a power density of 100 W/m^2 for all FPV configurations, and considering monofacial solar panels, it is possible to estimate not only the installed capacity and energy produced by the various types of FPV, but also the amount of water not evaporated due to the presence of FPV on the reservoirs. Given these assumptions, the estimates are evaluated at a global level, as well as at the country level, and Table 4.1 reports the global results and those for Italy (63rd in the FPV ranking).

Table 4.1 Estimates of installed capacity, generated power, and water-saving potential (Δ^{Ev}) of FPV

Region	Pmax [GWp] ([%])	EFX0 [TWh] ([%])	EFX0 [TWh] ([%])	EFX10 [TWh] ([%])	EFX20 [TWh] ([%])	EFXEW10 [TWh] ([%])	EFXEW20 [TWh] ([%])	EVSAT10 [TWh] ([%])	EVSAT20 [TWh] ([%])	EHSAT [TWh] ([%])	E2AT [TWh] ([%])	Δ^{Ev} [km3/y] ([%])
World	22206 (24)	26365 (103)	30965 (121)	28381 (111)	29794 (117)	26222 (103)	25808 (101)	30836 (121)	34539 (135)	35553 (139)	40398 (158)	215579 (5.4)
World (Tmin>0°C)	5344 (100)	8613 (34)	8909 (35)	8819 (35)	8839 (35)	8550 (34)	83450 (33)	9595 (38)	10351 (41)	19812(42)	11356 (45)	91417 (2.3)
Italy	21(20)	28(9.2)	32(11)	30(10)	31(10)	27 (9.2)	27 (9.0)	32(11)	36(12)	37(12)	41(14)	280 (0.82)

Where FX0 is a fixed system with a horizontal orientation (0° tilt), FX10 is a fixed system tilted at 10° and oriented toward the equator, FX20 indicates a fixed system tilted at 20° and oriented toward the equator, FXEW10 indicates a fixed 10° tilt with an East–West layout, where half the modules face east and the other half face west, FXEW20 indicates a fixed 20° tilt with an East–West layout, with panels split between east- and west-facing directions, VSAT10 indicates a system with a 10° tilt using a vertical single-axis (azimuth) tracker that rotates to follow the Sun's path, VSAT20 indicates a system with a 20° tilt using a vertical single-axis (azimuth) tracker that rotates to track the Sun's movement, HSAT is a system using a horizontal-axis tracker (north–south axis of rotation) that adjusts the tilt between −60° and 60° while facing east–west to maximize solar irradiance, and finally 2AT indicates a dual-axis tracking system combining both vertical and horizontal tracking to follow the Sun in two dimensions.

Table 4.1 shows that, in addition to the strong energy potential of FPV, they also make it possible to reduce the amount of water evaporation from the reservoirs where they are installed. Several studies in the literature have attempted to quantify the water savings of reservoirs with FPV installed, stating that the actual evaporation reduction due to FPV installation will depend on the float types, water body characteristics, and weather conditions. In [67] it is found that ponds with FPV installed had a 90% reduction in water evaporation compared to ponds without FPV installed. In [68], the authors instead find that the water reservoir has a 17% reduction in evaporation when it is partially covered with FPV systems, while the reduction reaches 28% when it is fully covered. Using the Penman–Monteith model, the authors in [69] studied the amount of water savings achieved for four FPV configurations across more than 4,000 reservoirs in different climates. It is observed that cold desert climates with dry winters exhibit the highest water savings. At the same time, it is also observed that the cooling effect of the reservoir water improves energy production, especially in climates where the temperature gradient is greater. In [70], the authors consider an arid region of Jordan for which water and energy consumption data are available, in order to determine which FPV configuration most reduces water consumption and increases energy yield. Standard floating PV was found to be the preferable option compared to ground-mounted PV and FPV with tracking, both with and without active cooling. Considering 20 lakes in the semi-arid regions of Rajasthan, [71] evaluate the effect of FPV deployment on the energy and water potential of the considered reservoirs for different coverage percentages. It is observed that lakes with larger surface areas have the greatest energy potential and water savings. Using the Linacre method, [72] evaluate the evaporation rates of a reservoir in North Carolina (USA) in the presence of FPV modules, observing that over one year the volume of water not evaporated amounts to 9 million gallons. In [73], the FAO Penman–Monteith method is used to evaluate water savings in five dams in the Tehran region. Using the SPEI index, which reveals an increasing drought trend over the analyzed period, it is observed that in one of these dams water savings reach up to 16 million cubic meters.

In some applications, FPV installations are directly integrated with hydroelectric plants, creating hybrid generation systems. It is estimated that the global potential of coupling FPV systems with hydropower plants ranges from 4.4 TW (6,270 TWh per year) to 5.7 TW (8,039 TWh per year) for hydropower-only reservoirs and multipurpose reservoirs, respectively [74]. Considering the largest 128 U.S. hydropower reservoirs, the authors of [75] observed that covering just 1.2% of the reservoir area with FPV modules would be enough to produce the same amount of electricity as the hydropower plants themselves. Looking at Europe, the authors in [76], considering 337 hydropower reservoirs, evaluate the potential electricity output of FPVs. Given an FPV installed capacity equal to that of the hydropower plants, FPVs can produce up to 40 TWh by covering 2.3% of the total reservoir area, with a water saving of 557 million m^3. The authors in [77] also confirm the beneficial effects in terms of energy production surplus and water savings from hydro-FPV hybridization. In fact, considering 146 hydropower reservoirs in Africa, the authors observe that with FPV coverage below 1%, electricity output grows by 58% (with an additional annual production of 46 TWh) and water savings of 743 million m^3 per year, increasing annual hydroelectricity generation by 170.64 GWh.

Within the framework presented so far, the present study analyzes evaporation rates and the associated water savings on reservoirs that, to the authors' knowledge, have not yet been considered in the literature. Different reservoir coverage percentages and FPV technologies are considered, using satellite-based meteorological data as inputs. Two case studies located in southern Italy are considered: Anapo, in Sicily, and Cesima, on the border between Molise and Campania. These sites are selected due to their relevance to Enel Green Power (EGP), a subsidiary of Enel S.p.A., which owns pumped-storage hydroelectric plants at both locations and has a technical and economic interest in quantifying the potential water savings achievable through partial basin coverage with FPV systems. To address this objective, daily and hourly evaporation rate are evaluated, together with cumulative monthly and annual water savings, expressed both in mm and cm^3. Coverage scenarios of 25%, 30%, and 40% of the basin surface are analyzed. The FPV technologies considered differ by specifically systems developed by Ciel et Terre, NRG, and Ocean Sun [78], [79], [80], and their relative effectiveness in reducing evaporation is assessed.

4.1.1 Methodology

Evaporation rates are evaluated using a modified formulation of the Penman–Monteith (PM) model [81]. In particular, the approach presented in [81] computes the saturated vapor pressure and the slope of the temperature–saturation vapor pressure curve as functions of water temperature, whereas other PM-based models rely on air temperature instead [82].

The model implemented in this study uses hourly meteorological inputs consisting of air temperature at 2 m (T_a, °C), relative humidity at 2 m (RH, %), global solar radiation (GSR, Wh/m²), and wind speed at 10 m (v, m/s). These data are obtained from the publicly available NASA database [83] and cover the period from December 2021 to November 2022. The dataset has a spatial resolution of 0.5° × 0.625° (latitude/longitude) and an hourly temporal resolution.

Table 4.1 summarizes the main physical characteristics of the Anapo and Cesima reservoirs, including the geographic coordinates used to extract the meteorological data and the key basin parameters required for evaporation assessment, namely surface area, elevation, and average depth. For both sites, evaporation rates are computed by considering the maximum regulation area as the reference surface, since using the minimum regulation area leads to negligible differences in the results.

Table 4.2 Details of the physical characteristics of the two case-study basins

	Anapo	Cesima
Geographical position(degrees)	37°06′ latitude and 15°08′ longitude	41°22′ latitude and 14°03′ longitude
Basin area (km²)	0.431	0.312
Basin elevation (m)	643	94.3
Basin depth (m)	25	21.3

The following paragraphs describe the climatological characteristics of the two locations, the FPV technologies considered, and the equations underlying the implemented model.

4.1.1.1 Comparison of the climatic features of the two sites

Before proceeding with the quantitative evaluation of evaporation rates at the two sites, it is useful to examine the climate data to identify any significant differences between Anapo and Cesima. Both locations lie within the Mediterranean climate zone, so major deviations in the trends of key meteorological variables are not expected. However, this comparison also helps to determine whether either site is influenced by a microclimate. Table 4.2 presents the monthly averages of hourly air temperature, wind speed, and relative humidity, along with the monthly average of daily global solar radiation.

Table 4.3 Comparison of the monthly mean values of the atmospheric variables of interest

	Anapo				Cesima			
Month	T_a (°C)	v_{10} (m/s)	RH (%)	GSR (MJ/m²d)	T_a (°C)	v_{10} (m/s)	RH (%)	GSR (MJ/m²d)
Dec - 21	10.47	4.80	84.55	8.34	8.63	3.43	85.44	5.71

Jan - 22	8.81	3.87	83.28	6.46	6.96	3.24	80.89	4.64
Feb - 22	10.10	4.22	80.05	13.52	8.63	3.25	80.40	10.71
Mar - 22	10.03	4.23	79.35	13.92	8.34	3.22	72.99	13.91
Apr - 22	14.11	4.80	72.78	20.48	12.68	3.42	70.48	19.85
May - 22	20.11	3.20	62.77	24.51	19.56	2.61	63.16	22.89
Jun - 22	27.94	2.71	44.51	27.52	26.00	2.53	51.62	26.35
Jul - 22	29.69	2.42	47.09	27.23	27.89	2.57	50.22	27.00
Aug - 22	28.33	2.44	55.83	22.43	26.74	2.17	55.94	21.52
Sep - 22	25.36	3.87	64.58	18.37	21.80	2.93	65.73	15.67
Oct - 22	20.48	2.57	71.71	14.98	18.31	2.12	71.37	13.67
Nov - 22	15.95	4.23	81.51	9.30	13.20	3.23	82.44	7.00

For a quick visual reference, what is reported in Table 4.2 is shown in Figure 4.1.

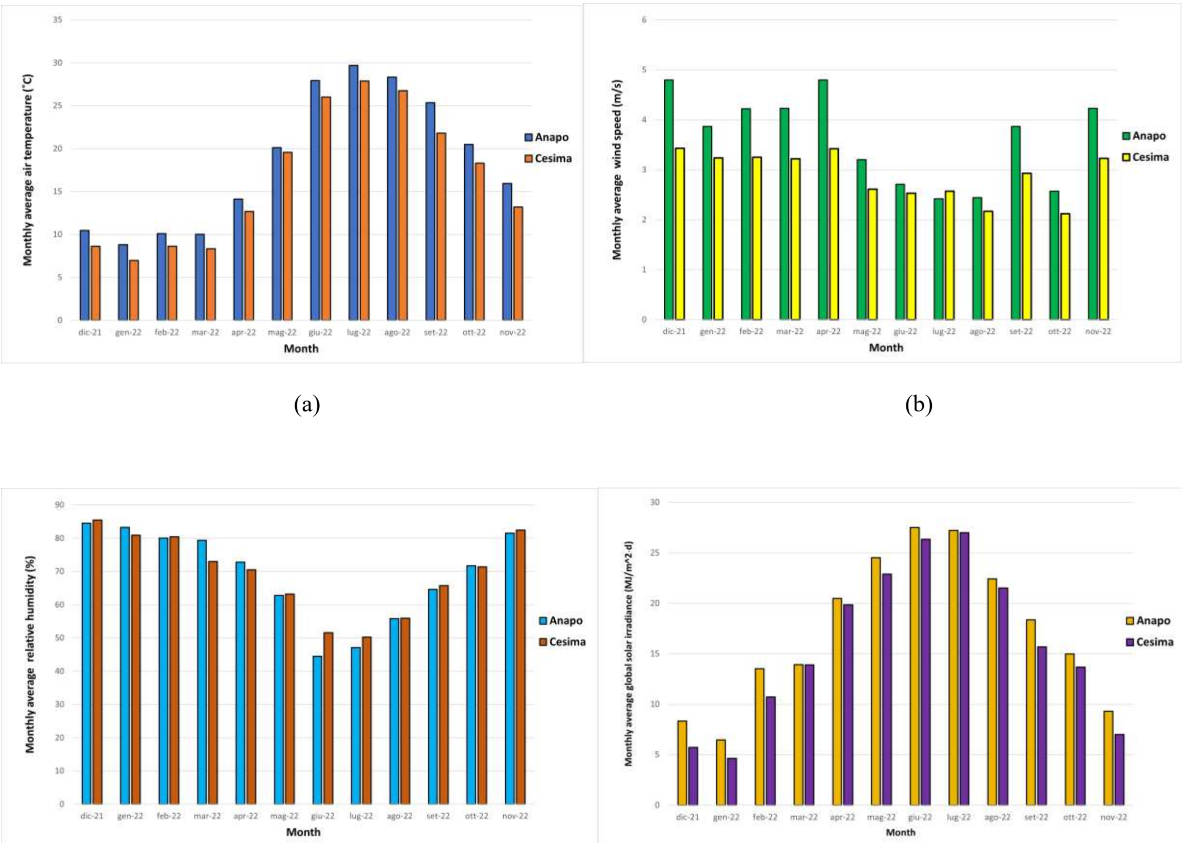

(a) (b)

(c) (d)

Figure 4.1. Comparison of the monthly hourly values of air temperature (a), wind speed (b), and relative humidity (c), together with the monthly average daily values of global solar radiation (d), for the two locations considered.

As can be inferred from Figure 4.1, the average irradiance levels are very similar for the two locations, and the same holds for the average air temperature values. This suggests that no significant microclimatic effects are present at either site. This conclusion is further supported by the relative humidity data, which show no practically relevant differences between Anapo and Cesima.

The only meteorological variable exhibiting more pronounced discrepancies is wind speed. The Anapo site appears to be windier than Cesima, with differences in wind speed magnitude exceeding 1 m/s during the winter and spring months (from November to April). In contrast, during the summer months (June, July, and August), these differences tend to diminish. Since wind speed is a key parameter influencing evaporation rates, the observed differences may explain potential variations in cumulative evaporation amounts between the two locations.

4.1.1.2 The FPV technology case studies

Among the meteorological variables, solar radiation is the factor with the greatest influence on evaporation rates. Solar radiation can be decomposed into three components: direct, diffuse, and reflected. Of these, the direct and diffuse components directly affect evaporation processes. Covering the free surface of reservoirs with FPV modules alters the amount of solar irradiation reaching the underlying water surface compared with an uncovered surface. These variations in incident solar radiation depend strongly on the specific FPV technology adopted.

For this reason, it is useful to provide additional details on the FPV technologies currently available in the literature and on the market. Considering the state of the art of floating systems as of 2025, FPV installations can be broadly classified into four categories:

- A: floating systems with floats that fully cover the water surface beneath the modules;
- B: floating systems with modules anchored to a tubular buoyancy structure;
- C: canal-top solar systems;
- D: flexible floating systems.

Type A systems are designed so that the water surface beneath the FPV modules is completely covered. As a result, the direct component of solar radiation reaching the water is largely blocked, and the diffuse component becomes the dominant contributor to the residual irradiation beneath the modules.

Type B technology consists of FPV modules supported by buoyant structures that occupy only part of the water surface, leaving significant portions of the basin uncovered. Unlike type A systems, both the direct and diffuse components of solar radiation reaching the water are only slightly reduced. In addition, the suspension of the modules above the water surface provides good natural ventilation, which enhances module cooling compared to type A configurations.

In type C systems, the FPV modules are neither floating nor suspended above the water surface. Instead, they are installed on the ground along the edges of canals or basins. In this case, the amount of incident solar radiation on the water surface depends on the spacing between module rows and their tilt angle. Furthermore, the transmitted radiation is influenced by the PV module technology: for instance, modules with gaps between cells, such as bifacial designs, allow a fraction of the radiation to pass through to the water surface.

Type D systems are characterized by FPV modules in direct contact with the water surface through a flexible, lamellar film that allows the structure to adapt to wave motion. This configuration leads to an even greater reduction in solar irradiation compared to type A systems and significantly limits evaporation due to reduced vapor mass exchange at the water–air interface. The direct contact between the modules and the water also promotes module cooling, thereby improving conversion efficiency. For clarity, schematic representations of the four FPV configurations considered are shown in Figure 4.2.

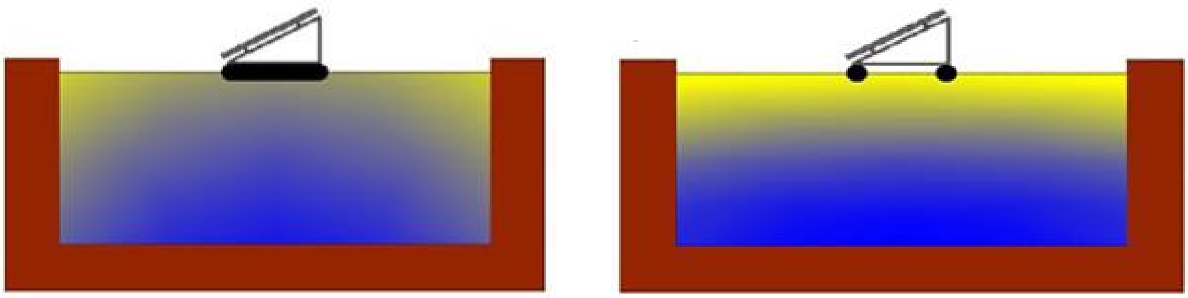

(a) (b)

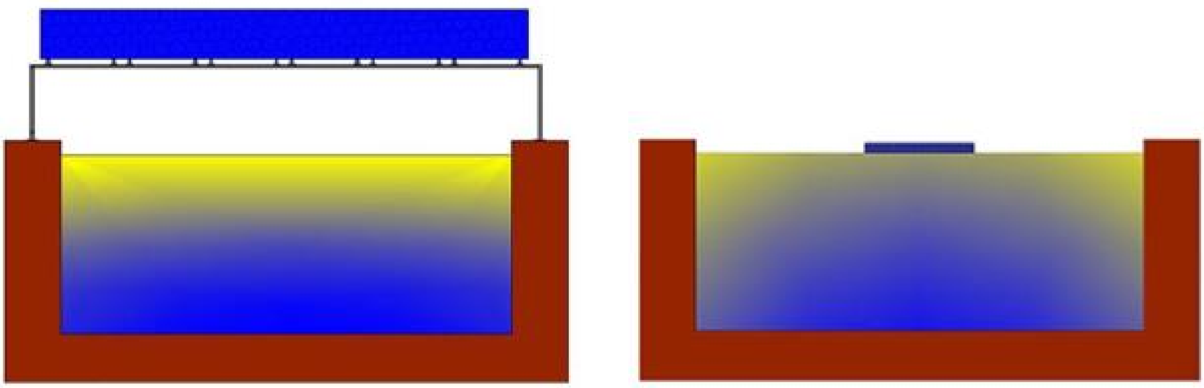

(c) (d)

Figure 4.2. Sketches of the four floating system configurations representing the current state of the art (2025). Panels (a), (b), (c), and (d) correspond to configurations A, B, C, and D described above, respectively.

The floating surface technologies analyzed in this study belong to categories A, B, and D, corresponding to [78], [79], and [80], respectively. Figure 4.3 illustrates the geometric and technical characteristics of the floating system technologies considered.

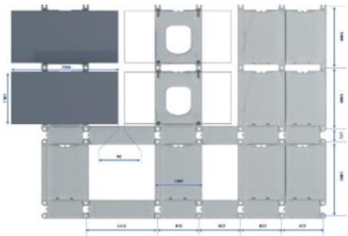

(a)

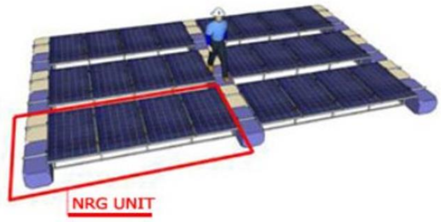

(b)

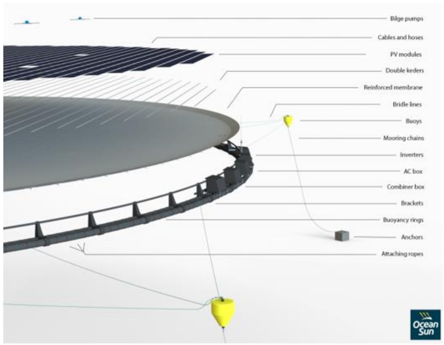

(c)

Figure 4.3. Geometric and technical characteristics of the three floating system technologies analyzed: (a) Ciel et Terre, (b) NRG, and (c) Ocean Sun.

Based on the floating system types described above, it is expected that type D would yield the greatest reduction in evaporative losses, followed by type A, whereas type B would result in the highest cumulative evaporation.

4.1.1.3 The mass and energy balance equations for open water surfaces

As outlined above, the model applied here to assess changes in daily and hourly evaporation rates based on varying percentages of covered surface relies on the PM equation for water evaporation. Key input parameters of this equation, such as net radiation and changes in stored heat, are adjusted according to the type of floating system, as described in Section 4.1.1.2. The PM equation is the one on which the Penman–Monteith model is based. This model can be used to evaluate evaporation rates from an open water surface, as it assumes a saturated surface. It is further assumed that the evaporation rate depends on the water surface temperature, air temperature, wind speed, and vapor pressure. In the Penman–Monteith model, when dealing with an open water surface, the heat storage of the water body must also be included, as variations in the water body's heat storage affect the water surface temperature and, consequently, evaporation. Therefore, a contribution due to the change in heat storage in the water body is added to the PM model equation. Thus, the following equation is considered to model the evaporation rates of open water surfaces, E, expressed in mm/days [84]:

$$E = \frac{1}{\lambda}\left(\frac{\Delta_w\,(Q^* - N) + 86400\rho_a C_a(e_w^* - e_a)/r_a}{\Delta_w + \gamma}\right) \tag{4.1}$$

Where λ is the latent heat of vaporization $(\mathrm{MJ/kg})$; Q^* is the net radiation $(\mathrm{MJ/m^2d})$; N is the change in heat storage in the water body $(\mathrm{MJ/m^2d})$; Δ_w is slope of the temperature saturation water vapor curve at water temperature $(\mathrm{kPa/°C})$; ρ_a is density of air $(\mathrm{kg/m^3})$; C_a is specific heat of air $(\mathrm{MJ/kgK})$; e_a is the vapor pressure (kPa); e_w^* is saturated vapor pressure at water temperature (kPa); γ is the psychometric constant $(\mathrm{kPa/°C})$; r_a is the aerodynamic resistance $(\mathrm{s/m})$.

The numerator of equation (4.1) mathematically represents the two fundamental components of the evaporation process: energy exchange and mass transfer, each described by one of the terms in the numerator. When considering equation (4.1) in its entirety, the terms that vary depending on the type of floating system are Δ_w, Q^*, N, and e_w^*. All these terms, except Q^*, are influenced by the water temperature, which changes according to the fraction of the surface covered. Q^* represents the net radiation, calculated as the difference between incoming short-wave solar radiation and outgoing long-wave radiation. The presence of FPV modules modifies both the short-wave and long-wave radiation reaching the covered water surface, as discussed in Section 4.1.1.2, and also alters the long-wave radiation emitted by the covered portion of the basin.

In general, the energy balance at the water surface can be expressed by the following equation [85]:

$$R_n = H_w - H_s - H_\lambda \tag{4.2}$$

Where R_n $(\mathrm{W/m^2})$ is the broadband net radiation, H_w $(\mathrm{W/m^2})$ is the water heat flux, H_s $(\mathrm{W/m^2})$ is the sensible heat flux, and H_λ $(\mathrm{W/m^2})$ is the latent heat flux. Specifically, H_w is the energy used to heat the water, H_s represents the heat exchange between the atmosphere and the surface, and H_λ represents the energy required for evaporation.

Focusing on solar radiation and considering the uncovered surface as the reference case, the elements of (4.2) relevant for evaporation assessments are the incoming solar radiation, $LW_\downarrow$ $(\mathrm{MJ/m^2d})$, and the outgoing solar radiation, $LW_\uparrow$ $(\mathrm{MJ/m^2d})$. The expressions for these two quantities can be written as follows [84]:

$$LW_{\downarrow} = \left(C_f + (1 - C_f)\left(1 - \left(0.261exp(-7.77 \cdot 10^{-4}T_a^2)\right)\right)\right)\sigma(T_a + 273.15)^4 \tag{4.3}$$

$$LW_{\uparrow} = 0.97\sigma(T_w + 273.15)^4 \tag{4.4}$$

Where C_f is the fraction of cloud cover, whose values range from 0 to 1, with 1 corresponding to 100% sky coverage; T_w is the water temperature (°C), and σ is the Stefan-Boltzmann constant ($\mathrm{MJ/m^2K^{-4}d}$).

In addition to the long-wave radiation emitted by the basin at the water temperature, there is another radiative component associated with emission at the wet-bulb temperature. This long-wave term, denoted as $LW_{\uparrow n}$ ($\mathrm{MJ/m^2d}$), is implemented here using the following expression [84]:

$$LW_{\uparrow n} = \sigma(T_a + 273.15)^4 + 4\sigma(T_a + 273.15)^3(T_n - T_a) \tag{4.5}$$

Where T_n (°C) is the wet-bulb temperature, and the other symbols have the meanings explained in the previous equations. Equations (4.2), (4.3), (4.4), and (4.5) are then suitably adapted to reflect the different types of floating installations.

To obtain hourly evaporation rates (mm/h) from the daily values, the following conversion is applied:

$$E_j(h) = E_j \cdot \frac{T_{a,j}(h)}{24 \cdot T_{a,j}} \tag{4.6}$$

where E_j is the daily evaporation value (mm/d); $T_{a,j}(h)$ represents the hourly air temperature profile for the j-th day (°C); and $T_{a,j}$ is the daily mean air temperature for the j-th day.

4.1.1.4 The mass and energy balance equations for water surfaces covered by floating systems

As outlined in Section 4.1.1.3, FPV installations modify both the short-wave and long-wave radiation reaching the covered part of a reservoir, as well as the long-wave radiation emitted by the water surface. This section therefore explains how the equations introduced in Section 4.1.1.2 are adapted in this study for each floating-system technology.

Type A. For the Ciel et Terre configuration, the direct component of incident short-wave radiation, SW_n, is modeled as the sum of the diffuse radiation and a fraction of the direct component. Both contributions are then slightly reduced by a multiplicative coefficient that reflects the fact that the raft structure does not fully cover the water surface beneath the modules. The same coefficient is applied to the incident long-wave radiation. A different coefficient is instead used in (4.4) to account for the partial blocking of outgoing long-wave radiation at water temperature by the floating modules; this coefficient is also applied to the long-wave radiation emitted at the wet-bulb temperature.

Type B. In this configuration, the FPV modules are suspended above the water surface. As a result, their effect on evaporation is less pronounced than in cases where the modules are in direct contact with the water. Accordingly, the long-wave radiation incident and emitted components (both at water and wet-bulb temperatures) are not reduced, and the incident short-wave radiation is only slightly attenuated compared with the Type A case.

Type D. Here the modules are in direct contact with the water surface. Like Type A, they float on the basin, but they provide a stronger shielding effect on incoming solar radiation. Therefore, both the short-wave and long-wave components of the incident radiation are reduced more than in Type A, using lower multiplicative coefficients. The long-wave radiation emitted at the water and wet-bulb temperatures is modeled as in Type A. In addition, the Ocean Sun configuration includes an elastic film between the modules and the water surface, which limits vapor mass exchange. This physical effect is represented by modifying the mass-transfer term in the Penman–Monteith equation to account for the reduced evaporation.

4.1.2 Results

This section presents the results for the two locations, first separately and then in comparison. Along with point and cumulative evaporation trends, monthly and annual cumulative evaporation values are reported for the three floating-system technologies considered. Results are shown for basin coverage levels of 25%, 30%, and 40%, which are the percentages of greatest practical interest.

4.1.2.1 Anapo basin case study

To examine how daily evaporation rates vary over the year, the first step is to plot the mm/d values evaluated with the model outlined in Section 4.1.1. Figure 4.4 shows the daily evaporation trend for the period from December 2021 to November 2022, both for the uncovered basin and for the case in which 30% of the surface is covered by each of the three floating-system technologies described above. The trends corresponding to other coverage percentages are not shown, since the shape of the curves does not change with coverage; only their amplitude varies.

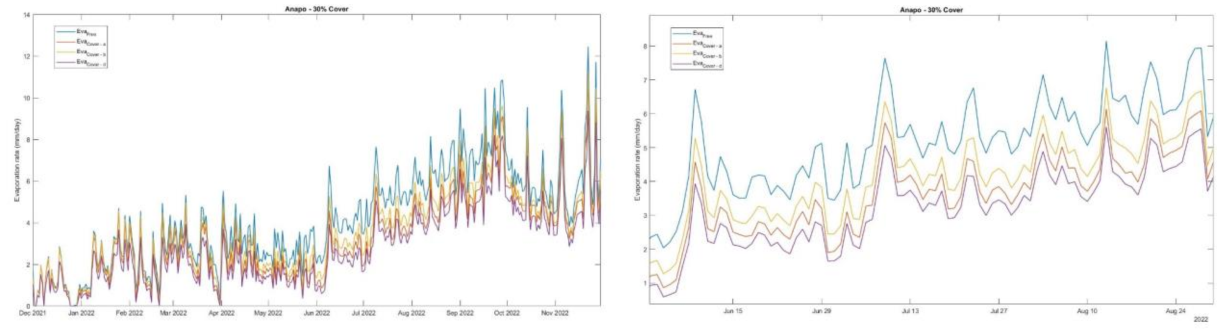

(a) (b)

Figure 4.4. Daily evaporation curves for the Anapo basin over the study year (December 2021–November 2022) (a), and a zoom on the summer period (b), for the free surface and for the surface covered by the three floating-system technologies analyzed here, with 30% coverage.

As expected from the geometric and physical characteristics of the floating systems analyzed here, Figure 4.4 shows that configuration D (Ocean Sun) yields the lowest daily evaporation rates. Among the three technologies, type B (NRG) produces the highest daily evaporation, while type A (Ciel et Terre) represents an intermediate case between B and D.

From Figure 4.4(a) it can be seen, on the one hand, that the mm/d trend of evaporated water increases markedly during the summer months, as intuitively expected. On the other hand, relatively high daily evaporation values are also observed in November. This may be due to unusually low precipitation (and thus higher irradiance), higher-than-average air temperatures, or the thermal inertia of the basin.

For completeness, the cumulative evaporation trends for both the free and covered surface cases are reported in Figure 4.5.

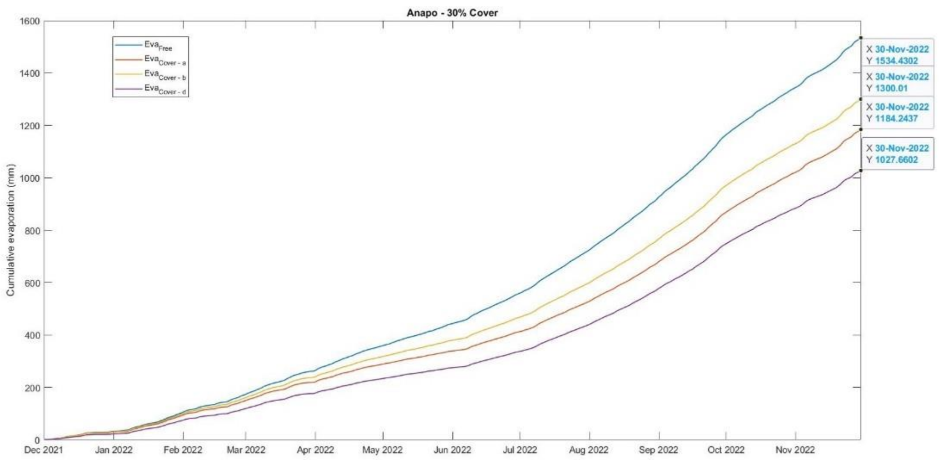

Figure 4.5. Cumulative evaporation curves for the Anapo basin, comparing the free water surface with the case of 30% coverage using the three floating system technologies.

As expected, the cumulative curves confirm the relative performance of the different floating system types observed in the daily trends. As noted in Section 4.1.1, evaporation rates were evaluated for surface coverage levels of 25%, 30%, and 40%. The corresponding results for the three floating technologies are reported in Tables 4.3, 4.4, and 4.5, where monthly cumulative evaporation is provided in both millimeters and cubic meters, along with the annual totals.

Table 4.4 Monthly and annual cumulative evaporation values obtained with the Ciel et Terre floating system (type A) for different surface coverage percentages. The cumulative evaporation for the free-surface case is also included for comparison.

Month	Free		25% coverage		30% coverage		40% coverage	
	E_{cum} (mm)	E_{cum} (m³)	E_{cum} (mm)	E_{cum} (m³)	E_{cum} (mm)	E_{cum} (m³)	E_{cum} (mm)	E_{cum} (m³)
Dec-21	31.47	1.36e+04	28.93	1.25e+04	28.49	1.22e+04	27.63	1.19e+04
Jan - 22	71.14	3.07e+04	64.07	2.76e+04	62.79	2.72e+04	60.28	2.60e+04
Feb - 22	69.46	2.99e+04	58.28	2.51e+04	56.14	2.42e+04	52.02	2.24e+04
Mar-22	91.13	3.93e+04	74.98	3.23e+04	71.88	3.10e+04	65.71	2.83e+04
Apr - 22	95.80	4.13e+04	72.58	3.13e+04	68.06	2.93e+04	59.09	2.55e+04
May-22	84.77	3.65e+04	56.32	2.43e+04	50.76	2.19e+04	39.71	1.71e+04
Jun - 22	114.93	4.95e+04	79.76	3.44e+04	72.95	3.15e+04	59.45	2.56e+04
Jul - 22	163.73	7.06e+04	121.88	5.25e+04	113.80	4.91e+04	97.81	4.22e+04
Aug-22	198.99	8.58e+04	156.62	6.75e+04	148.45	6.40e+04	132.26	5.70e+04
Sep - 22	240.61	1.04e+05	198.07	8.54e+04	189.84	8.18e+04	173.54	7.48e+04
Oct - 22	183.53	7.91e+04	159.18	6.86e+04	154.48	6.66e+04	145.18	6.26e+04
Nov-22	194.40	8.38e+04	171.12	7.38e+04	166.61	7.18e+04	157.67	6.80e+04
Annual	1539.96	6.641e+05	1241.79	5.35e+05	1184.25	5.106e+05	1070.36	4.61e+05

Table 4.5 Monthly and annual cumulative evaporation values obtained with the NRG floating system (type B) for different surface coverage percentages. The cumulative evaporation for the free-surface case is also included for comparison.

Month	Free		25% coverage		30% coverage		40% coverage	
	E_{cum} (mm)	E_{cum} (m³)	E_{cum} (mm)	E_{cum} (m³)	E_{cum} (mm)	E_{cum} (m³)	E_{cum} (mm)	E_{cum} (m³)
Dec - 21	31.47	1.36e+04	29.94	1.29e+04	29.71	1.28e+04	29.25	1.26e+04
Jan - 22	71.14	3.07e+04	67.52	2.91e+04	66.94	2.89e+04	65.82	2.84e+04
Feb - 22	69.46	2.99e+04	63.10	2.72e+04	61.92	2.67e+04	59.58	2.57e+04
Mar - 22	91.13	3.93e+04	81.25	3.50e+04	79.38	3.42e+04	75.66	3.26e+04
Apr - 22	95.80	4.13e+04	81.07	3.50e+04	78.21	3.37e+04	72.51	3.13e+04
May-22	84.77	3.65e+04	66.17	2.85e+04	62.52	2.70e+04	55.24	2.38e+04
Jun - 22	114.93	4.95e+04	91.39	3.94e+04	86.85	3.74e+04	77.81	3.35e+04
Jul - 22	163.73	7.06e+04	135.37	5.84e+04	129.93	5.60e+04	119.14	5.14e+04
Aug - 22	198.99	8.58e+04	169.86	7.32e+04	164.28	7.08e+04	153.23	6.61e+04
Sep - 22	240.61	1.04e+05	210.61	9.08e+04	204.85	8.83e+04	193.43	8.34e+04
Oct - 22	183.53	7.91e+04	165.55	7.14e+04	162.10	6.99e+04	155.27	6.69e+04
Nov - 22	194.40	8.38e+04	176.76	7.62e+04	173.35	7.47e+04	166.60	7.18e+04
Annual	1539.96	6.641e+05	1338.59	5.77e+05	1300	5.60e+05	1223.54	5.28e+05

Table 4.6 Monthly and annual cumulative evaporation values obtained with the Ocean Sun floating system (type D) for different surface coverage percentages. The cumulative evaporation for the free-surface case is also included for comparison.

Month	Free		25% coverage		30% coverage		40% coverage	
	E_{cum} (mm)	E_{cum} (m³)	E_{cum} (mm)	E_{cum} (m³)	E_{cum} (mm)	E_{cum} (m³)	E_{cum} (mm)	E_{cum} (m³)
Dec - 21	31.47	1.36e+04	22.40	9.65e+03	22.00	9.48e+03	21.23	9.15e+03
Jan - 22	71.14	3.07e+04	51.70	2.23e+04	50.46	2.18e+04	48.03	2.07e+04
Feb - 22	69.46	2.99e+04	46.69	2.01e+04	44.85	1.93e+04	41.24	1.78e+04
Mar - 22	91.13	3.93e+04	61.93	2.67e+04	59.33	2.56e+04	54.16	2.34e+04
Apr - 22	95.80	4.13e+04	59.61	2.57e+04	55.95	2.41e+04	48.68	2.10e+04
May-22	84.77	3.65e+04	46.41	2.00e+04	42.02	1.81e+04	33.29	1.44e+04
Jun - 22	114.93	4.95e+04	66.42	2.86e+04	61.06	2.63e+04	50.44	2.18e+04
Jul - 22	163.73	7.06e+04	107.59	4.64e+04	101.26	4.37e+04	88.73	3.83e+04
Aug - 22	198.99	8.58e+04	141.29	6.09e+04	134.87	5.81e+04	122.17	5.27e+04
Sep - 22	240.61	1.04e+05	178.22	7.68e+04	171.74	7.40e+04	158.92	6.85e+04
Oct - 22	183.53	7.91e+04	141.20	6.09e+04	137.51	5.93e+04	130.20	5.61e+04
Nov - 22	194.40	8.38e+04	150.24	6.48e+04	146.64	6.32e+04	139.50	6.01e+04
Annual	1539.96	6.641e+05	1073.69	4.63e+05	1027.69	4.43e+05	936.58	4.04e+05

In addition to the values presented in the previous tables, for clarity and completeness it is useful to report the amount of water saved, both in millimeters and cubic meters, due to the presence of the floating systems. The water savings are therefore provided in detail on a monthly and annual basis in Tables 4.6, 4.7, and 4.8, for each of the three floating system technologies.

Table 4.7 Water savings achieved by covering the basin's free surface with Ciel et Terre (type A) floating systems, shown for the three coverage percentages.

Month	25% coverage		30% coverage		40% coverage	
	E_{cum} (mm)	E_{cum} (m³)	E_{cum} (mm)	E_{cum} (m³)	E_{cum} (mm)	E_{cum} (m³)
Dec - 21	2.54	1.10e+03	2.98	1.40e+03	3.84	1.70e+03
Jan - 22	7.07	3.10e+03	8.35	3.50e+03	10.86	4.70e+03
Feb - 22	11.18	4.80e+03	13.32	5.70e+03	17.44	7.50e+03
Mar - 22	16.15	7.00e+03	19.25	8.30e+03	25.42	1.10e+04
Apr - 22	23.22	1.00e+04	27.74	1.20e+04	36.71	1.58e+04
May-22	28.45	1.22e+04	34.01	1.46e+04	45.06	1.94e+04
Jun - 22	35.17	1.51e+04	41.98	1.80e+04	55.48	2.39e+04
Jul - 22	41.85	1.81e+04	49.93	2.15e+04	65.92	2.84e+04
Aug - 22	42.37	1.83e+04	50.54	2.18e+04	66.73	2.88e+04
Sep - 22	42.54	1.86e+04	50.77	2.22e+04	67.07	2.92e+04
Oct - 22	24.35	1.05e+04	29.05	1.25e+04	38.35	1.65e+04
Nov - 22	23.28	1.00e+04	27.79	1.20e+04	36.73	1.58e+04
Annual	298.17	1.29e+05	355.71	1.535e+05	469.60	2.03e+05

Table 4.8 Water savings obtained by covering the basin's free surface with NRG (type B) floating systems, for the three coverage percentages.

Month	25% coverage		30% coverage		40% coverage	
	E_{cum} (mm)	E_{cum} (m^3)	E_{cum} (mm)	E_{cum} (m^3)	E_{cum} (mm)	E_{cum} (m^3)
Dec - 21	1.53	7.00e+02	1.76	8.00e+02	2.22	1.00e+03
Jan - 22	3.62	1.60e+03	4.2	1.80e+03	5.32	2.30e+03
Feb - 22	6.36	2.70e+03	7.54	3.20e+03	9.88	4.20e+03
Mar - 22	9.88	4.30e+03	11.75	5.10e+03	15.47	6.70e+03
Apr - 22	14.73	6.30e+03	17.59	7.60e+03	23.29	1.00e+04
May-22	18.60	8.00e+03	22.25	9.50e+03	29.53	1.27e+04
Jun - 22	23.54	1.01e+04	28.08	1.21e+04	37.12	1.60e+04
Jul - 22	28.36	1.22e+04	33.8	1.46e+04	44.59	1.92e+04
Aug - 22	29.13	1.26e+04	34.71	1.50e+04	45.76	1.97e+04
Sep - 22	30.00	1.32e+04	35.76	1.57e+04	47.18	2.06e+04
Oct - 22	17.98	7.70e+03	21.43	9.20e+03	28.26	1.22e+04
Nov - 22	17.64	7.60e+03	21.05	9.10e+03	27.80	1.20e+04
Annual	201.37	8.70e+04	240	1.04e+05	316.42	1.37e+05

Table 4.9 Water savings obtained by covering the basin's free surface with Ocean Sun (type D) floating systems, for the three coverage percentages.

Month	25% coverage		30% coverage		40% coverage	
	E_{cum} (mm)	E_{cum} (m^3)	E_{cum} (mm)	E_{cum} (m^3)	E_{cum} (mm)	E_{cum} (m^3)
Dec - 21	9.07	3.95e+03	9.47	4.12e+03	10.24	4.45e+03
Jan - 22	19.44	8.40e+03	20.68	8.90e+03	23.11	1.00e+04
Feb - 22	22.77	9.80e+03	24.61	1.06e+04	28.22	1.21e+04
Mar - 22	29.20	1.26e+04	31.8	1.37e+04	36.97	1.59e+04
Apr - 22	36.19	1.56e+04	39.85	1.72e+04	47.12	2.03e+04
May-22	38.36	1.65e+04	42.75	1.84e+04	51.48	2.21e+04
Jun - 22	48.51	2.09e+04	53.87	2.32e+04	64.49	2.77e+04
Jul - 22	56.14	2.42e+04	62.47	2.69e+04	75.00	3.23e+04
Aug - 22	57.70	2.49e+04	64.12	2.77e+04	76.82	3.31e+04
Sep - 22	62.39	2.72e+04	68.87	3.00e+04	81.69	3.55e+04
Oct - 22	42.33	1.82e+04	46.02	1.98e+04	53.33	2.30e+04
Nov - 22	44.16	1.90e+04	47.76	2.06e+04	54.90	2.37e+04
Annual	466.27	2.01e+05	512.27	2.21e+05	603.38	2.60e+05

4.1.2.2 Cesima basin case study

As in the Anapo case study, Figure 4.6 illustrates the trends in daily evaporation rates estimated by the model for the Cesima site.

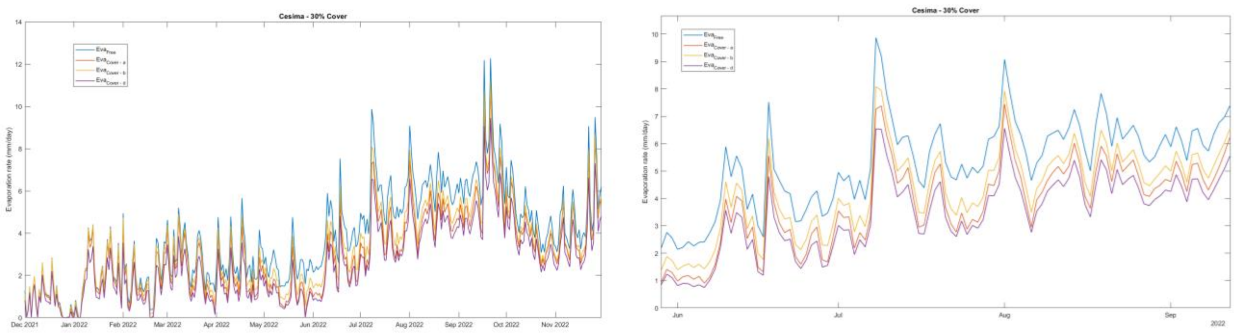

(a) (b)

Figure 4.6. Daily evaporation curves for the Cesima basin over the study year (December 2021–November 2022) (a), and the corresponding summer zoom (b), for the free surface and for the surface covered by the three floating system types analyzed here, with 30% coverage.

Unlike the Anapo basin, the model for the Cesima basin does not show higher evaporation rates in November than in the summer months. This confirms that the November peaks observed at Anapo are not due to a modeling artifact, but rather to the specific weather conditions that occurred in November 2022, as already hypothesized in Section 4.1.2.1. For completeness, the cumulative daily evaporation trends for Cesima are reported in Figure 4.7.

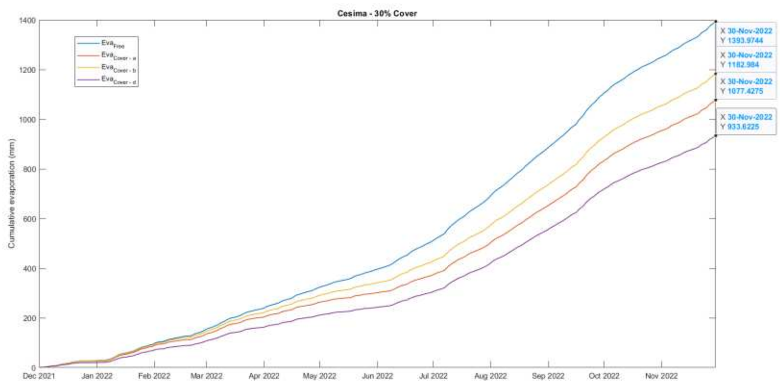

Figure 4.7. Accumulated evaporation curves for both the free water surface and the covered surface (30% coverage) using the three floating system technologies considered, for the Cesima basin.

As for the Anapo basin, the cumulative monthly and annual evaporation values, as well as the monthly and annual water savings for the three floating system technologies considered, are reported below for the three coverage percentages analyzed for the Cesima basin.

Table 4.10. Monthly and annual cumulative evaporation values obtained with the Ciel et Terre floating system (type A) for different coverage percentages, with the free-surface case included for comparison.

Month	Free		25% coverage		30% coverage		40% coverage	
	E_{cum} (mm)	E_{cum} (m³)	E_{cum} (mm)	E_{cum} (m³)	E_{cum} (mm)	E_{cum} (m³)	E_{cum} (mm)	E_{cum} (m³)

Dec - 21	27.72	8.65e+03	25.86	8.07e+03	25.52	7.96e+03	24.87	7.76e+03
Jan - 22	65.27	2.04e+04	60.40	1.89e+04	59.49	1.86e+04	57.71	1.80e+04
Feb - 22	57.19	1.79e+04	48.09	1.50e+04	46.32	1.45e+04	43.05	1.34e+04
Mar - 22	86.83	2.71e+04	73.00	2.28e+04	70.28	2.19e+04	65.10	2.03e+04
Apr - 22	83.97	2.62e+04	63.57	1.98e+04	59.56	1.86e+04	51.61	1.61e+04
May - 22	73.17	2.28e+04	45.00	1.40e+04	39.45	1.23e+04	28.92	9.02e+03
Jun - 22	113.12	3.53e+04	77.21	2.41e+04	70.16	2.19e+04	56.20	1.75e+04
Jul - 22	176.86	5.52e+04	134.32	4.19e+04	125.97	3.93e+04	109.44	3.42e+04
Aug - 22	196.50	6.13e+04	159.01	4.96e+04	151.65	4.73e+04	137.08	4.28e+04
Sep - 22	218.09	6.81e+04	185.79	5.80e+04	179.45	5.60e+04	166.92	5.21e+04
Oct - 22	148.46	4.63e+04	127.84	3.99e+04	123.78	3.86e+04	115.72	3.61e+04
Nov - 22	146.83	4.58e+04	129.25	4.03e+04	125.79	3.93e+04	118.93	3.71e+04
Annual	1394.01	4.35e+05	1129.34	3.52e+05	1077.42	3.36e+05	975.51	3.04e+05

Table 4.11. Monthly and annual cumulative evaporation values obtained with the NRG floating system (type B) for different coverage percentages, with the free-surface case included for comparison.

Month	Free		25% coverage		30% coverage		40% coverage	
	E_{cum} (mm)	E_{cum} (m^3)	E_{cum} (mm)	E_{cum} (m^3)	E_{cum} (mm)	E_{cum} (m^3)	E_{cum} (mm)	E_{cum} (m^3)
Dec - 21	27.72	8.65e+03	26.89	8.39e+03	26.75	8.35e+03	26.49	8.27e+03
Jan - 22	65.27	2.04e+04	63.68	1.99e+04	63.40	1.98e+04	62.90	1.96e+04
Feb - 22	57.19	1.79e+04	52.79	1.65e+04	51.93	1.62e+04	50.22	1.57e+04
Mar - 22	86.83	2.71e+04	79.00	2.47e+04	77.46	2.42e+04	74.42	2.32e+04
Apr - 22	83.97	2.62e+04	71.58	2.23e+04	69.12	2.16e+04	64.24	2.01e+04
May-22	73.17	2.28e+04	55.18	1.72e+04	51.61	1.61e+04	44.48	1.39e+04
Jun - 22	113.12	3.53e+04	89.35	2.79e+04	84.65	2.64e+04	75.33	2.35e+04
Jul - 22	176.86	5.52e+04	147.85	4.61e+04	142.14	4.44e+04	130.82	4.08e+04
Aug - 22	196.50	6.13e+04	170.40	5.32e+04	165.27	5.16e+04	155.11	4.84e+04
Sep - 22	218.09	6.81e+04	194.84	6.08e+04	190.28	5.94e+04	181.25	5.66e+04
Oct - 22	148.46	4.63e+04	132.94	4.15e+04	129.87	4.05e+04	123.78	3.86e+04
Nov - 22	146.83	4.58e+04	133.19	4.16e+04	130.51	4.07e+04	125.17	3.91e+04
Annual	1394.01	4.35e+05	1217.69	3.80e+05	1183	3.69e+05	1114.20	3.48e+05

Table 4.12 Monthly and annual cumulative evaporation values obtained with the Ocean Sun floating system (type D) for varying coverage percentages, including the free-surface case for comparison.

Month	Free		25% coverage		30% coverage		40% coverage	
	E_{cum} (mm)	E_{cum} (m^3)	E_{cum} (mm)	E_{cum} (m^3)	E_{cum} (mm)	E_{cum} (m^3)	E_{cum} (mm)	E_{cum} (m^3)
Dec - 21	27.72	8.65e+03	20.46	6.38e+03	20.11	6.28e+03	19.48	6.08e+03
Jan - 22	65.27	2.04e+04	48.49	1.51e+04	47.50	1.48e+04	45.56	1.42e+04
Feb - 22	57.19	1.79e+04	38.24	1.19e+04	36.68	1.15e+04	33.68	1.05e+04
Mar - 22	86.83	2.71e+04	59.17	1.85e+04	56.81	1.77e+04	52.31	1.63e+04
Apr - 22	83.97	2.62e+04	51.86	1.62e+04	48.55	1.52e+04	42.01	1.31e+04

May - 22	73.17	2.28e+04	36.89	1.15e+04	32.61	1.02e+04	24.24	7.56e+03
Jun - 22	113.12	3.53e+04	66.22	2.07e+04	60.67	1.89e+04	49.67	1.55e+04
Jul - 22	176.86	5.52e+04	119.28	3.72e+04	112.76	3.52e+04	99.86	3.12e+04
Aug - 22	196.50	6.13e+04	142.93	4.46e+04	137.19	4.28e+04	125.84	3.93e+04
Sep - 22	218.09	6.81e+04	166.17	5.19e+04	161.21	5.03e+04	151.41	4.72e+04
Oct - 22	148.46	4.63e+04	112.61	3.51e+04	109.42	3.41e+04	103.10	3.22e+04
Nov - 22	146.83	4.58e+04	112.90	3.52e+04	110.12	3.44e+04	104.60	3.26e+04
Annual	1394.01	4.35e+05	975.22	3.04e+05	934	2.91e+05	851.76	2.66e+05

Table 4.13 Water savings achievable by covering the basin's free surface with Ciel et Terre technology (type A) at the three different coverage percentages.

Month	25% coverage		30% coverage		40% coverage	
	E_{cum} (mm)	E_{cum} (m^3)	E_{cum} (mm)	E_{cum} (m^3)	E_{cum} (mm)	E_{cum} (m^3)
Dec - 21	1.86	5.80e+02	2.2	6.90e+02	2.85	8.90e+02
Jan - 22	4.87	1.50e+03	5.78	1.80e+03	7.56	2.40e+03
Feb - 22	9.10	2.90e+03	10.87	3.40e+03	14.14	4.50e+03
Mar - 22	13.83	4.30e+03	16.55	5.20e+03	21.73	6.80e+03
Apr - 22	20.40	6.40e+03	24.41	7.60e+03	32.36	1.01e+04
May-22	28.17	8.80e+03	33.72	1.05e+04	44.25	1.38e+04
Jun - 22	35.91	1.12e+04	42.96	1.34e+04	56.92	1.78e+04
Jul - 22	42.54	1.33e+04	50.89	1.59e+04	67.42	2.10e+04
Aug - 22	37.49	1.17e+04	44.85	1.40e+04	59.42	1.85e+04
Sep - 22	32.30	1.01e+04	38.64	1.21e+04	51.17	1.60e+04
Oct - 22	20.62	6.40e+03	24.68	7.70e+03	32.74	1.02e+04
Nov - 22	17.58	5.50e+03	21.04	6.50e+03	27.90	8.70e+03
Annual	264.67	8.26e+04	316.59	9.88e+04	418.50	1.31e+05

Table 4.14 Water savings achievable by covering the basin's free surface with NRG technology (type B) at the three different coverage percentages.

Month	25% coverage		30% coverage		40% coverage	
	E_{cum} (mm)	E_{cum} (m^3)	E_{cum} (mm)	E_{cum} (m^3)	E_{cum} (mm)	E_{cum} (m^3)
Dec - 21	0.83	2.60e+02	0.97	3.00e+02	1.23	3.80e+02
Jan - 22	1.59	5.00e+02	1.87	6.00e+02	2.37	8.00e+02
Feb - 22	4.40	1.40e+03	5.26	1.70e+03	6.97	2.20e+03
Mar - 22	7.83	2.40e+03	9.37	2.90e+03	12.41	3.90e+03
Apr - 22	12.39	3.90e+03	14.85	4.60e+03	19.73	6.10e+03
May-22	17.99	5.60e+03	21.56	6.70e+03	28.69	8.90e+03
Jun - 22	23.77	7.40e+03	28.47	8.90e+03	37.79	1.18e+04
Jul - 22	29.01	9.10e+03	34.72	1.08e+04	46.04	1.44e+04
Aug - 22	26.10	8.10e+03	31.23	9.70e+03	41.39	1.29e+04
Sep - 22	23.25	7.30e+03	27.81	8.70e+03	36.84	1.15e+04
Oct - 22	15.52	4.80e+03	18.59	5.80e+03	24.68	7.70e+03
Nov - 22	13.64	4.20e+03	16.32	5.10e+03	21.66	6.70e+03
Annual	176.32	5.49e+04	211.02	6.58e+04	279.81	8.72e+04

Table 4.15 Water savings that would be achieved by covering the free area of the basin with Ocean Sun technology (type D), for the three different coverage percentages.

Month	25% coverage		30% coverage		40% coverage	
	E_{cum} (mm)	E_{cum} (m^3)	E_{cum} (mm)	E_{cum} (m^3)	E_{cum} (mm)	E_{cum} (m^3)
Dec - 21	7.26	2.27e+03	7.61	2.37e+03	8.24	2.57e+03
Jan - 22	16.78	5.30e+03	17.77	5.60e+03	19.71	6.20e+03
Feb - 22	18.95	6.00e+03	20.51	6.40e+03	23.51	7.40e+03
Mar - 22	27.66	8.60e+03	30.02	9.40e+03	34.52	1.08e+04
Apr - 22	32.11	1.00e+04	35.42	1.10e+04	41.96	1.31e+04
May-22	36.28	1.13e+04	40.56	1.26e+04	48.93	1.52e+04
Jun - 22	46.90	1.46e+04	52.45	1.64e+04	63.45	1.98e+04
Jul - 22	57.58	1.80e+04	64.1	2.00e+04	77.00	2.40e+04
Aug - 22	53.57	1.67e+04	59.31	1.85e+04	70.66	2.20e+04
Sep - 22	51.92	1.62e+04	56.88	1.78e+04	66.68	2.09e+04
Oct - 22	35.85	1.12e+04	39.04	1.22e+04	45.36	1.41e+04
Nov - 22	33.93	1.06e+04	36.71	1.14e+04	42.23	1.32e+04
Annual	418.79	1.31e+05	460.38	1.44e+05	542.25	1.69e+05

4.1.2.3 Comparisons between the two case studies

For the sake of summary and easier comparison, it is helpful to present tables that contrast the two study sites in terms of annual cumulative evaporation and annual water savings. Tables 4.15, 4.16, and 4.17 provide these values for the three floating system technologies and coverage percentages analyzed. Additionally, the coverage efficiencies of each floating system, corresponding to their specific coverage percentages, are also included. Efficiency (%) is calculated using the following formula:

$$\eta = \frac{E_{free\ cum} - E_{FPV\ cum}}{E_{free\ cum}} \cdot 100 \tag{4.7}$$

Where $E_{free\ cum}$ represents the annual evaporation (in mm or m³) from the uncovered basin surface, and $E_{FPV\ cum}$ represents the annual evaporation (in mm or m³) from the basin area covered with FPV modules.

Table 4.16 Comparison, for the two study locations of the cumulative annual amount of water evaporated and saved, and the coverage efficiencies of the three different technologies of floating systems for a coverage percentage of 25%.

	Anapo				Cesima			
	Free surface	Ciel et terre	NRG	Ocean Sun	Free surface	Ciel et terre	NRG	Ocean Sun
Annual evaporation (mm)	1539.96	1241.79	1338.59	1073.69	1394.01	1129.34	1217.69	975.22
Annual evaporation (m^3)	6.641e+05	5.35e+05	5.77e+05	4.63e+05	4.35e+05	3.52e+05	3.80e+05	3.04e+05
Annual water savings (mm)	-	298.17	201.37	466.27	-	264.67	176.32	418.79
Annual water savings (m^3)	-	1.29e+05	8.70e+04	2.01e+05	-	8.26e+04	5.49e+04	1.31e+05
Annual coverage efficiency, η (%)	-	19.1	12.8	30.0	-	19.0	12.7	30.1

Table 4.17 Comparison, for the two study locations of the cumulative annual amount of water evaporated and saved, and the coverage efficiencies of the three different technologies of floating systems for a coverage percentage of 30%.

	Anapo				Cesima			
	Free surface	Ciel et terre	NRG	Ocean Sun	Free surface	Ciel et terre	NRG	Ocean Sun
Annual evaporation (mm)	1539.96	1184.25	1300	1027.69	1394.01	1077.42	1183	934
Annual evaporation (m^3)	6.641e+05	5.106e+05	5.60e+05	4.43e+05	4.35e+05	3.36e+05	3.69e+05	2.91e+05
Annual water savings (mm)	-	355.71	240	512.27	-	316.59	211.02	460.38
Annual water savings (m^3)	-	1.535e+05	1.04e+05	2.21e+05	-	9.88e+04	6.58e+04	1.44e+05
Annual coverage efficiency, η (%)	-	22.8	15.3	33.0	-	22.7	15.2	33.0

Table 4.18 Comparison, for the two study locations of the cumulative annual amount of water evaporated and saved, and the coverage efficiencies of the three different technologies of floating systems for a coverage percentage of 40%.

	Anapo				Cesima			
	Free surface	Ciel et terre	NRG	Ocean Sun	Free surface	Ciel et terre	NRG	Ocean Sun
Annual evaporation (mm)	1539.96	1070.36	1223.54	936.58	1394.01	975.51	1114.20	851.76
Annual evaporation (m^3)	6.641e+05	4.61e+05	5.28e+05	4.04e+05	4.35e+05	3.04e+05	3.48e+05	2.66e+05
Annual water savings (mm)	-	469.60	316.42	603.38	-	418.50	279.81	542.25
Annual water savings (m^3)	-	2.03e+05	1.37e+05	2.60e+05	-	1.31e+05	8.72e+04	1.69e+05
Annual coverage efficiency, η (%)	-	30.3	20.3	39.0	-	30.0	20.1	38.9

Examining the tables above, it is evident that the Anapo site experiences higher annual evaporation from the free water surface compared to Cesima. This can be explained by the generally higher solar radiation, air temperatures, and wind speeds recorded at Anapo (see Figure 4.1).

Considering the efficiency values, it is clear that each type of floating system shows similar efficiency percentages at both sites. This indicates that the performance of the floating systems analyzed is largely consistent across the two locations, likely due to their shared Mediterranean climate. Finally, in both locations, the Ocean Sun technology delivers the greatest reduction in evaporation and thus the highest water savings, followed by the Ciel et Terre system. The NRG technology results in the largest annual water loss. The ranking of the systems' efficiency values mirrors this pattern.

4.1.3 Conclusions

The Penman-Monteith model was used to estimate daily and hourly evaporation rates from water surfaces. The model was adapted to account for the influence of different floating system technologies on the evaporation of basin surfaces. Two case studies, the Anapo and Cesima basins, are considered and three commercially available floating system technologies were analyzed: Ciel et Terre, NRG, and Ocean Sun. Evaporation rates were evaluated for basin coverage percentages of 25%, 30%, and 40%.

Monthly average trends of key meteorological variables, including solar radiation, air temperature, relative humidity, and wind speed, were examined. The Anapo site exhibited higher average values for these variables compared to Cesima, which is reflected in the results: cumulative annual evaporation (and the corresponding water savings) was greater at Anapo than at Cesima.

Among the three floating system technologies, Ocean Sun demonstrated the highest effectiveness in reducing evaporation and maximizing water savings. Coverage efficiencies were found to be very similar between the two locations for each type of technology, indicating consistent performance across both sites.

4.1.4 Hybridization of offshore solar and wind systems

As the world advances toward decarbonization and long-term carbon neutrality, coastal areas are intensifying efforts to exploit renewable energy from the marine environment. Offshore wind power has expanded rapidly and, in many regions, has already reached cost competitiveness with conventional generation. At the same time, early-stage offshore FPV projects are beginning to appear. Developing marine resources in an integrated manner and using ocean space more efficiently for energy production are becoming central to the creation of multifunctional offshore energy systems, which are essential for achieving high-quality, large-scale carbon neutrality [86].

Nevertheless, the large-scale roll-out of offshore energy systems faces notable constraints, particularly in marine areas characterized by moderate wind resources, where stand-alone floating wind farms often struggle to achieve financial viability. In semi-enclosed basins such as the Mediterranean Sea, however, high solar availability combined with relatively calm wave conditions opens up new opportunities for offshore FPV. Yet, the joint operation of multiple generation technologies and their interaction with the power grid require detailed technical and economic evaluation. In [87], the authors focus on a hybrid offshore energy hub located off the Sicilian coast in southern Italy, designed around a maximum transmission capacity of 1 GW. The system is optimized by testing different combinations of floating wind and solar generation with the objective of increasing net present value, lowering the levelized cost of energy, and improving the load factor of the export cable. Two development pathways are explored. The first considers a fully hybrid plant with a total installed capacity of 1 GW, where the relative shares of wind and solar are progressively adjusted. The second pathway starts from a baseline 1 GW floating wind farm and adds FPV capacity while constraining the export limit to 1 GW, with excess production curtailed.

Because wind power is inherently variable, pairing offshore wind with other renewable sources offers an effective way to stabilize electricity generation. The authors in [88] examine the feasibility of integrating offshore wind and solar energy through a case study in Asturias (Spain), a region where floating technologies are essential for marine renewables due to the absence of shallow waters, which makes fixed-bottom turbines impractical. Using high-resolution resource data and the technical characteristics of commercial wind turbines and FPV modules, the wind and solar potential and expected production are evaluated. Compared with a conventional offshore wind farm, a hybrid wind–solar installation increases installed capacity and annual energy output per unit of occupied sea surface by approximately one order of magnitude and sevenfold, respectively, significantly improving the efficiency of marine space use. In addition, the combined system delivers a much more stable power profile.

Given the growing importance of hybridizing FPV with offshore wind plants, it is interesting to carry out a study that also involves wind technology. The next section deals with a study on the impacts of climate change on offshore wind production.

4.2 Assessment of the impact of climate change on the performance of an offshore wind turbine

The interplay between climate and energy systems is attracting growing attention in both policy development and scientific research [89]. In power systems, electricity generation influences the atmosphere—and consequently future climate—through greenhouse gas (GHG) emissions, while climatic conditions, in turn, affect electricity supply and demand [90]. In response to the emissions associated with power generation, the European Union has introduced several energy transition strategies, including the Green Deal, which promotes substantial deployment of ND-RESs, such as solar photovoltaics (PV) and wind energy [91]. Wind energy infrastructure includes both onshore and offshore installations, each with distinct advantages and limitations. Offshore wind farms, in particular, help overcome land availability constraints, which has driven the expansion of these installations. Global offshore wind capacity is expected to rise sharply, reaching approximately ten times the 2018 level by 2030 and fifty times by 2050 [92]. In light of this expansion, the present study focuses on evaluating the wind energy potential at selected sites in the southern Mediterranean.

Traditional assessments of wind farm performance generally rely on historical wind data, often neglecting projected trends over future decades. For instance, [93] and [94] examine the Mediterranean region but consider only past wind records, while [95] conducts a local-scale analysis without including future wind projections. Ignoring the evolution of the wind resource is problematic, given that wind turbines typically operate for at least twenty years. To address this, the current study examines wind speed trends both historically and for a short-to-medium-term future horizon using climate projections from the Coupled Model Intercomparison Project Phase 6 (CMIP6) [96]. CMIP6 represents the latest phase of the CMIP initiative, consolidating global climate models from research centers worldwide, and was used in the IPCC’s Sixth Assessment Report (AR6) [97]. This study specifically leverages CMIP6 models providing hourly outputs, the finest temporal resolution currently available (2025), which is a novel feature compared to most previous studies that rely on three-hour or coarser data [98], [99], [100].

The study evaluates the expected energy output of a reference offshore wind turbine (OWT), using the relative power curve alongside both historical and projected wind speeds. The analysis is performed through both deterministic and stochastic approaches, with the latter based on Monte Carlo (MC) simulations. A stochastic approach is chosen to account for the intrinsic uncertainty in OWT energy production, which prior research has shown to be a dominant factor in technical and economic assessments of wind farms [101] and [102]. Furthermore, climate model projections carry their own uncertainties [103], which are particularly relevant for evaluating turbine fatigue and operational lifetime [104]. Monte Carlo simulations enable the generation of multiple possible energy production outcomes, rather than a single deterministic estimate, which also allows the stochastic results to be benchmarked against deterministic calculations.

To the author’s knowledge, no previous study has applied Monte Carlo simulations to generate OWT energy production profiles from synthetically created hourly wind speed datasets. In the literature, MC approaches have primarily been used to sample Weibull distribution parameters [105], simulate random system states [106], evaluate life-cycle uncertainties [107], assess economic performance [108], or model turbine failure probabilities [109]. Moreover, few studies combine historical data and climate projections to stochastically simulate hourly offshore wind power production [110] [111]. This study addresses that gap by implementing a Monte Carlo framework that generates multiple energy scenarios for the reference OWT based on probability distributions derived from both historical observations and climate model outputs.

The methods and the corresponding results of the studies conducted are detailed below.

4.2.1 Methods for studying the complementarity of wind power production and the impact of climate change on it at offshore sites

The aim is to study the energy yield of three offshore sites along the southern coast of Sicily. Considering a reference OWT, the profiles of power extractable from the wind and the energy yield of the OWT are evaluated for the three locations considered. For these assessments, both historical wind speed data and climate projections of wind speed are considered. The historical data are taken from the New European Wind Atlas (NEWA) [112], while the climate projections are taken from the Pan-European Climate Database (PECD), version 4.1 [113]. NEWA is a database designed for conducting wind potential studies for locations across the European continent. This database is among those with the highest spatial and temporal resolution publicly available (to the knowledge of the authors). The PECD 4.1, on the other hand, is a database resulting from the collaboration between the Copernicus Climate Change Service (C3S) and the ENTSO-E. The PECD 4.1 is well-suited as an optimal database for studying the impacts of climate change on power systems, and it consists of three CMs: CMCC-CM2-SR5 (hereafter, CMCC), EC-Earth3 (hereafter, ECEC), and MPI-ESM1-2-HR (hereafter, MPI). The only available emission scenario is SSP2-4.5 (where SSP stands for Shared Socioeconomic Pathways), which is representative of intermediate GHG emissions. For the analysis that follow, all three available climate models are considered, with SSP2-4.5 as the forcing scenario.

The analyses described below are conducted on both an annual and a seasonal basis, considering winter and summer as the seasons, since these are the most critical for wind power production and for the adequacy of a power system. The months December–January–February (DJF) are considered as winter, while the months June–July–August (JJA) are considered as summer. To account for the spatial variability of the wind resource, three case study locations are considered. Two of these locations are close to each other in order to test the spatial sensitivity of the analyses conducted. This local-scale approach is novel, as previous studies either focused on the southwestern Mediterranean [114], excluded southern Sicily [115], [116], or did not analyze climate change impacts on offshore wind production in the region [117]. Finally, the selected Sicilian sites are either hosting offshore wind farms or planned for development in the near future.

4.2.1.1 Power extractable from the wind and correlation analysis

For power system adequacy purposes, it is important to understand whether there is complementarity among the generation sources connected to the grid of a given system. Therefore, the profiles of power extractable from the kinetic energy of the wind are evaluated at each of the considered case study locations, and the correlation among these profiles is assessed. This correlation is spatiotemporal, since for each location the semi-hourly time series of wind producibility profiles are evaluated, and the degree of interdependence of these profiles among the three locations is assessed.

The power extractable from the wind can be evaluated using the following formula [118]:

$$P_W = \frac{1}{2} \rho_{hub} \cdot A_r \cdot v_{hub}^3 \tag{4.8}$$

Where ρ_{hub} (kg/m^3) is the air density at hub height, A_r (m^2) is the swept area of the rotor, and v_{hub} (m/s) is the wind speed at hub height. A_r is known from the nameplate parameters of the considered OWT, while ρ_{hub} and v_{hub} must be evaluated using extrapolation laws for atmospheric variables at the hub height. The air density at hub height can be assessed using the following formula (ideal gas law):

$$\rho_{hub} = \frac{p_{hub} \cdot M \cdot 10^{-3}}{R \cdot T_{hub}} \tag{4.9}$$

Where p_{hub} (Pa) is the air pressure at hub height, M (g/mol) is the molar mass of air, and T_{hub} (K) is the temperature at hub height, and R $(\text{J}/(\text{mol} \cdot \text{K}))$ is the universal gas constant. Therefore, to extrapolate the air density at hub height, it is necessary to extrapolate the air pressure and temperature to hub height.

The air temperature is extrapolated to hub height using the following [119]:

$$T_{hub} = T_{2m} - 0.0065 \cdot \Delta H_T \tag{4.10}$$

Where T_{2m} (K) is the temperature data at 2 m, and ΔH_T (m) is the height difference between the hub height and the measurement height of the temperature data. The use of (4.3) allows accounting for the effect of temperature on the power extractable from the wind.

The air density can then be extrapolated using the following [119]:

$$p_{hub} = p_a \left(1 - \frac{0.0065 \cdot \Delta H_P}{T_{2m}}\right)^{5.225} \tag{4.11}$$

Where p_a is the surface atmospheric pressure (Pa) and ΔH_P (m) is the difference in meters between the turbine hub height and the surface pressure data. Equation (4.2) allows for an accurate evaluation of air density, which is crucial in a marine environment, where conditions differ from those onshore to which standard air density values usually refer [120].

To extrapolate the wind speed to hub height, the following can be used [121]:

$$v_{hub} = v_{h_{data}} \left(\frac{h_{hub}}{h_{data}}\right)^{\alpha} \tag{4.12}$$

Where $v_{h_{data}}$ (m/s) is the wind speed at the data height (h_{data} in meters), h_{hub} (m) is the hub height, and α is the power law exponent (dimensionless). The value of α is here evaluated using wind speed climate data (NEWA database) at two different heights (200 m and 100 m), so that the only unknown in equation (4.5) is the power law exponent.

Once the wind producibility profiles for each location have been evaluated using the previous equations, the correlation among these profiles is then assessed using the sample Pearson correlation coefficient, *r*, expressed by the following equation [122], [123]:

$$r = \frac{\sum_{i=1}^{n}(x_i - \bar{x})\,(y_i - \bar{y})}{\sqrt{\sum_{i=1}^{n}(x_i - \bar{x})^2}\,\sqrt{\sum_{i=1}^{n}(y_i - \bar{y})^2}} \tag{4.13}$$

Where n is the data size, x_i and y_i are the wind speed data at location x and y, with means $\bar{x}$ and $\bar{y}$, respectively. A value of $r = 1$ indicates a perfect positive linear correlation between the variables x and y, while the value of $r = -1$ indicates a perfect negative linear correlation (anticorrelation) between the variables x and y. The null hypothesis underlying the correlation analysis conducted here is that there is no correlation between the pairs of producibility profiles considered. The significance level is set to 0.05. Considering a linear correlation index is justified by the fact that wind power production profiles follow a power curve that, for most wind speed values, exhibits an almost linear trend. Moreover, the analysis is specifically aimed at assessing the degree of linear correlation between the hourly wind production profiles of the sites considered.

4.2.1.2 Deterministic and stochastic approaches for evaluating the production of a single OWT

After evaluating the power extractable from the wind, the hourly production of a single offshore turbine is then assessed. To do this, both deterministic and stochastic methods are used. The deterministic approach is based on interpolating wind speed data onto the power curve of the single OWT. Since the power curve provides instantaneous values of power produced by the single OWT, this interpolation yields time series of power production whose resolution depends on the wind speed data used. In this study, hourly wind speed data and hourly wind speed projections are used, thus obtaining hourly profiles of power produced by the OWT. Once these profiles are obtained, the energy produced by the OWT can be easily evaluated on both a seasonal and an annual basis.

However, the drawback of using a deterministic approach is that it does not account for the uncertainties involved in wind power production by a turbine. In fact, the power curve is an average curve, representative of the turbine's production profile, but it is not the one that the turbine will actually follow over its lifetime. Moreover, when considering climate wind speed projections, the intrinsic uncertainty of climate model outputs must also be considered. It would therefore be desirable to adopt a stochastic approach that allows the simulation of multiple scenarios in order to account for the many uncertainties associated with the production of an OWT. In this work, a Monte Carlo algorithm is therefore implemented to simulate various wind power production scenarios. Indeed, one of the benefits of employing Monte Carlo simulations is that each run generates an hourly energy production profile for a specific OWT, effectively capturing a range of potential output scenarios.

The Monte Carlo algorithm implemented is based on the inverse method [124], [125]. Specifically, both historical wind speed data and wind speed projections are fitted with Weibull distributions [126], [127], as its application represents the state of the art in modeling wind speed distributions [128], [129], [130], [131]. The Weibull distributions that best fit the wind speed time series are identified using the Maximum Likelihood Estimation (MLE) method [132]. Once the best fitting Weibull distributions are identified, the corresponding cumulative distribution functions (CDFs) are evaluated, and their inverses (ICDFs) are then calculated. By then drawing values between 0 and 1 according to a uniform distribution, these are input into the ICDFs, thus obtaining synthetic wind speed profiles. These synthetic profiles are then interpolated onto the OWT power curve, thus obtaining stochastic wind power production profiles. The implemented MC methodology uses a dual convergence criterion, considering both a maximum number of iterations and a predefined tolerance.

4.2.2 The impacts of climate change on offshore wind power production off the coast of Sicily

All the methods described in the previous subsection are applied to three locations offshore the southern coast of Sicily, as shown in Figure 4.8. All simulations are conducted on MATLAB (R2019a) [133], and the corresponding results are presented in the following.

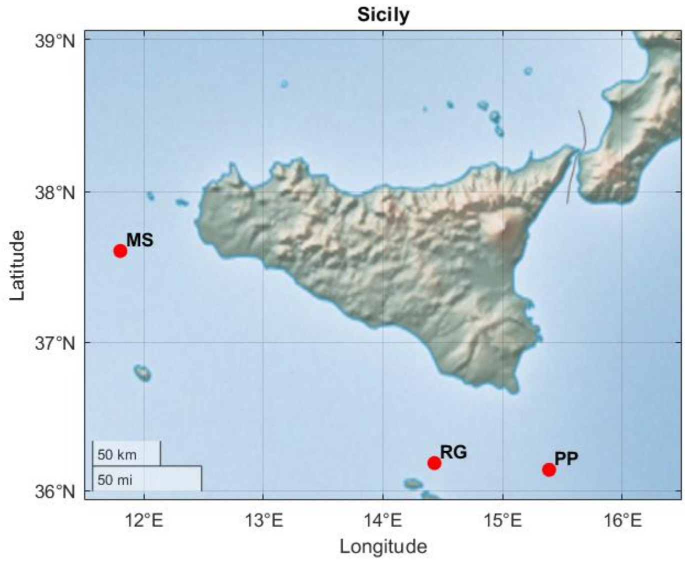

Figure 4.8. Location of the three case-study sites. MS is the site offshore the coast of Marsala, RG offshore the coast of Ragusa, and PP offshore the coast of Porto Palo.

As can be observed from Figure 4.8, the three sites marked in red are located at almost the same distance from the coast (≅60 km), so that all three experience the same coastal proximity effect on wind conditions. The sites have the following geographical coordinates: 36.14229° latitude and 15.38965° longitude for PP, 36.18732° latitude and 14.43054° longitude for RG, and 37.60892° latitude and 11.80261° longitude for MS. These same coordinates are selected for the historical data of wind speed at 100 m, air temperature at 2 m, and surface atmospheric pressure. Moreover, these coordinates also correspond to one of the four vertices of the grid cells selected for the CM outputs. Specifically, the projection cells have the following coordinates: North: 36.142325°, West: 15.39°, South: 35.8°, East: 15.64° for PP; North: 36.4264°, West: 14.4281°, South: 36.1764°, East: 14.6781° for RG; North: 37.6°, West: 11.75°, South: 37.35°, East: 12° for MS. Regarding the CMs, for the analyses, wind speed climate projections at 100 m are considered.

Once the locations for studying the wind potential are identified, the turbine on which to perform the energy yield evaluations is chosen. For this purpose, a 15 MW reference offshore turbine from the National Renewable Energy Laboratory (NREL) is selected [134]. Using the formulas presented in Section 4.2.1, the semi-hourly profiles of power extractable from the wind are evaluated. The 15 MW OWT has the following characteristics: a 170 m hub height and a rotor diameter of 240 m [134]. To determine the power extractable from the wind, historical data of wind speed at 100 m, air temperature at 2 m, and surface air pressure are used. These data are provided as inputs to the equations shown in Section 4.2.1. The semi-hourly profiles of power extractable from the wind are evaluated for the three locations considered, and the correlations among these profiles are assessed. Figure 4.9

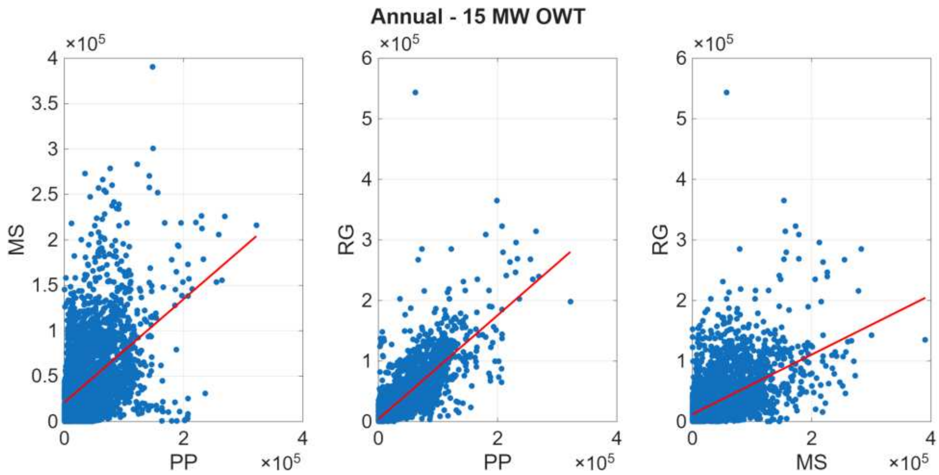

Figure 4.9. Scatter plots of the hourly values of the producible power from the 15 reference OWTs, on an annual basis, for each pair of locations considered.

From Figure 4.9, it can be observed that there is a particularly strong linear relationship between the production profiles of PP and RG. This relationship weakens for locations that are farther apart. Therefore, the greater the distance between locations, the weaker the linear relationship between the wind production profiles of the turbines.

The correlation analysis is conducted on both an annual and a seasonal basis. It is observed that the correlation results do not exhibit marked temporal variability, since moving from an annual to a seasonal basis the Pearson coefficient r values differ only slightly. Figure 4.10 shows the trends of the r coefficient values evaluated on an annual basis.

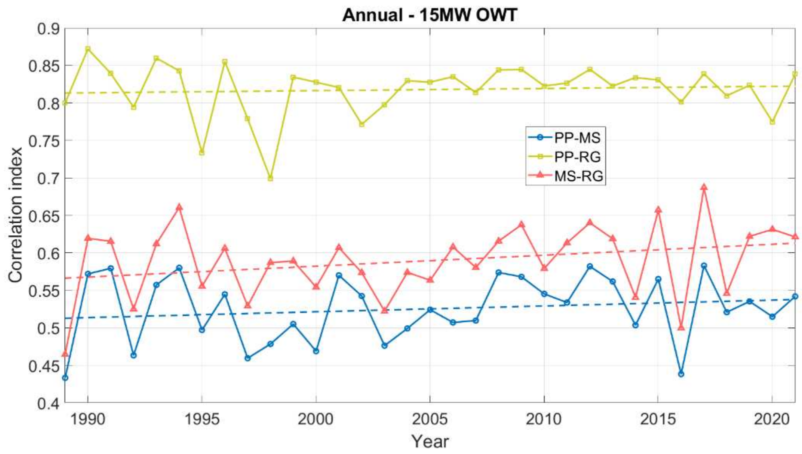

Figure 4.10. Degree of correlation between the wind-extractable power profiles of the pairs of case-study locations, on an annual basis.

For all pairs of wind power extractable profiles, a strong positive correlation is observed ($p < 0.05$). This implies that there is no complementarity in the wind power production of the three locations. That is, if one site is affected by wind drought, the others are very likely to be affected as well, which poses a problem for the adequacy of the power system to which the plants are connected.

Once the correlations among the wind power extractable profiles have been evaluated, the hourly profiles of power produced by the 15 MW OWT are then assessed. To do this, it is necessary to know the turbine power curve, which is taken from the SAM software [135]. Specifically, the synthetic historical and projected wind speed profiles, obtained as described in Section 4.2.1, are therefore interpolated onto the power curve of the 15 MW OWT, thus yielding synthetic hourly profiles of power produced by the single turbine. This is done in each MC simulation. The Monte Carlo algorithm stops when the error between successive iterations falls below the tolerance threshold (= 10^{-4}) and when the number of iterations exceeds N = 1000. The hourly production profile of the single turbine is also evaluated deterministically by interpolating both the historical data and the wind speed projections onto the power curve of the 15 MW OWT. Once the hourly power output is known, the energy produced on an annual and seasonal basis can be evaluated, and the results for the deterministic case, using historical data as input, are shown in Figure 4.11.

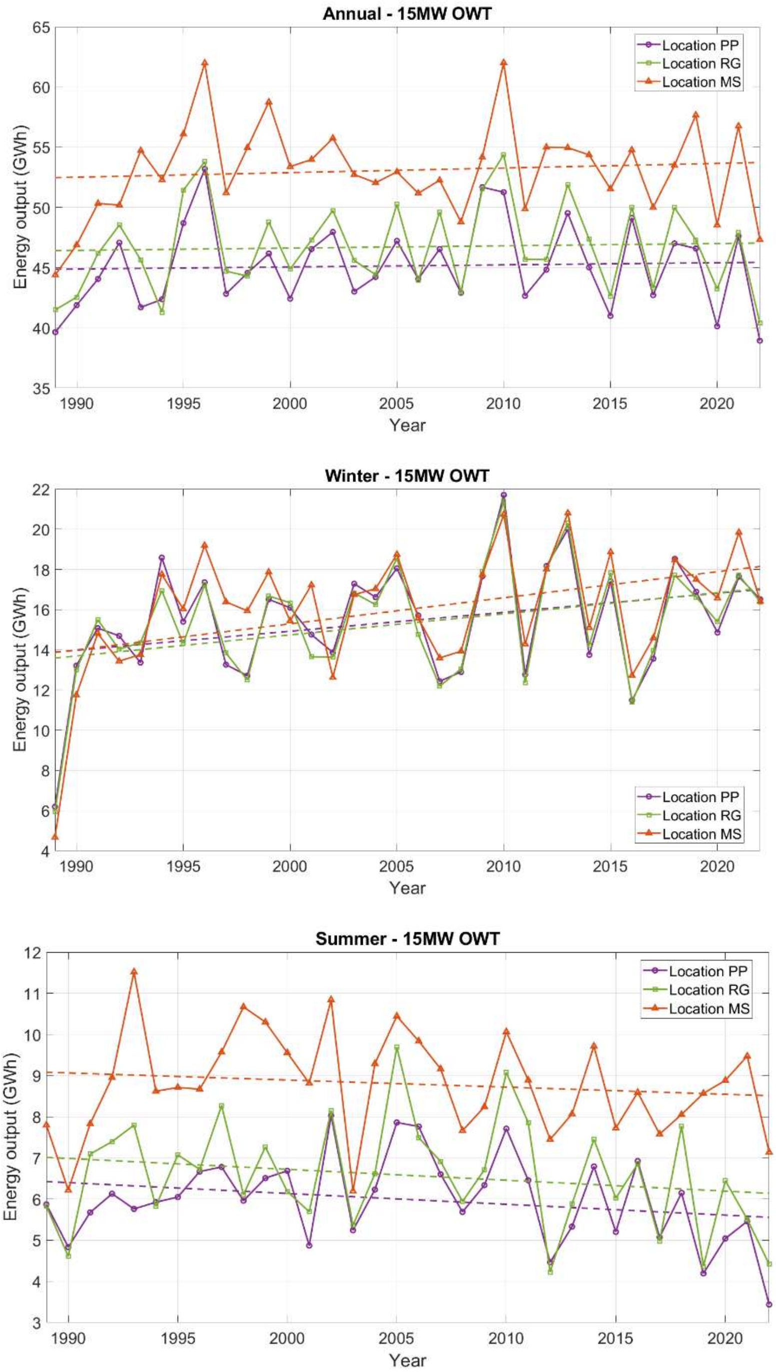

Figure 4.11. Trends of the energy yield of the reference 15 MW offshore wind turbine (NREL) evaluated from the historical data 1989-2022, both on an annual and seasonal basis.

From Figure 4.11, it is interesting to note that the annual trend results from the compensation between the winter and summer trends. It can also be observed that, on a summer basis, the MS trend shows a gap compared to the others, whereas on a winter basis, no such gap is present. This demonstrates how the spatial variability of the results changes depending on the season considered.

Figure 4.11 provides qualitative results, and it would therefore be useful to evaluate descriptive statistics of the observed trends. The means, medians, P95, and the STD of the obtained energy values are thus assessed, and the results are reported in Table 4.1.

Table 4 19. Mean, median, 95th percentile (P95), and standard deviation (STD) of the trends in the energy produced by the 15 MW OWT, evaluated deterministically using historical wind speed data, for all three case study locations.

Location	Statistics (GWh)	Annual	Winter	Summer
PP	Mean	45.15	15.44	5.99
	Median	44.69	15.56	6.00
	P95	51.59	19.72	7.84
	STD	3.50	2.89	1.05
RG	Mean	46.72	15.32	6.58
	Median	45.93	15.45	6.67
	P95	53.41	19.95	8.92
	STD	3.66	2.88	1.31
MS	Mean	53.09	16.01	8.80
	Median	53.16	16.40	8.76
	P95	61.33	20.56	10.81
	STD	3.88	3.06	1.24

From Table 4.1 and Figure 4.11, it can be observed that the MS location has the highest statistical values. From Table 4.1, it can also be noted that in winter the statistics of the three locations do not differ markedly from one another.

Once the deterministic evaluations of the energy produced by the single OWT have been carried out, the Monte Carlo algorithm is then applied. One thousand simulations are performed, thus obtaining one thousand hourly power profiles and, consequently, one thousand energy production values on both an annual and a seasonal basis. The averages of these energy values are computed, yielding results close to those obtained using the deterministic method. This validates the implemented Monte Carlo algorithm. Moreover, to verify the convergence of the MC method, the cumulative means of the energy produced in each MCS are evaluated, and Figure 4.12 shows the results on both an annual and a seasonal basis.

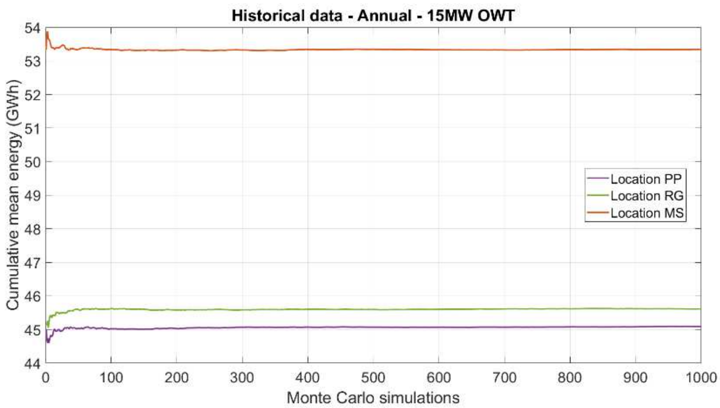

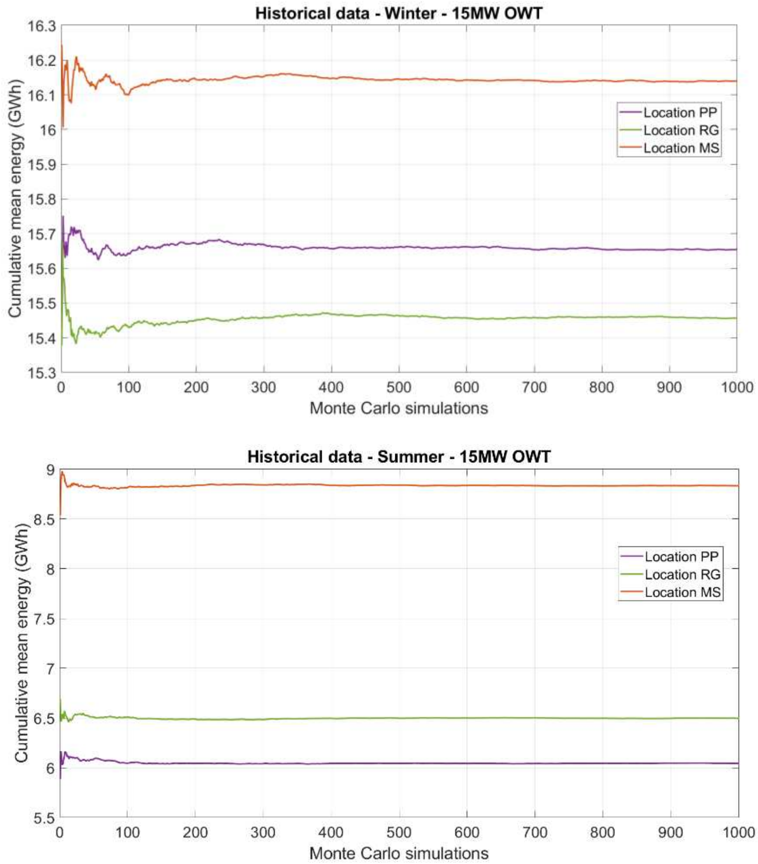

Figure 4.12. Convergence of the implemented Monte Carlo method for the stochastic simulation of the energy produced by the 15 MW OWT, on both an annual and a seasonal basis.

The results presented so far are obtained using historical data. The same deterministic and stochastic evaluations are therefore repeated using wind speed projections. Figure 4.13 shows the trends of the output energy evaluated on an annual basis for the three case study locations, using wind speed projections at 100 m.

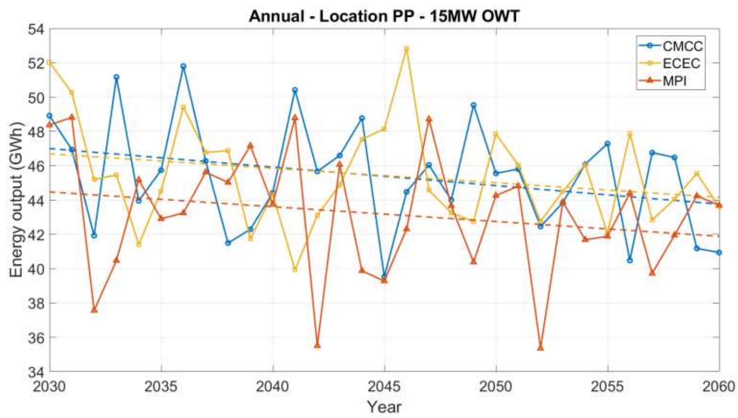

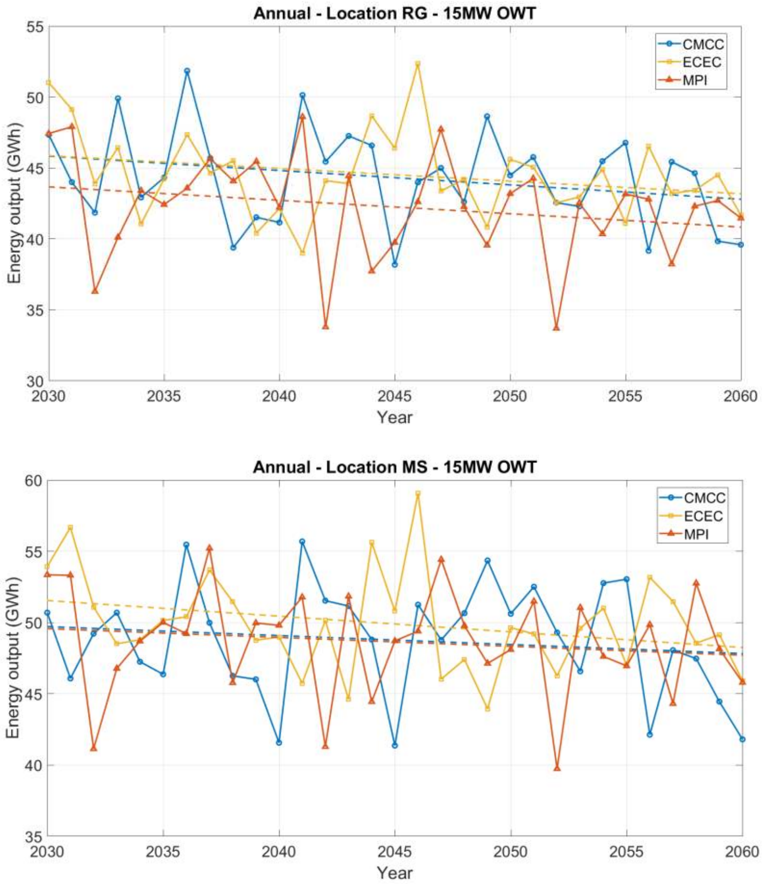

Figure 4.13. Trends of the projected energy output from a 15 MW OWT in the three case study locations, on an annual basis.

From Figure 4.13, it can be observed that the three climate models agree in projecting decreasing trends in the energy produced by the 15 MW OWT. Moreover, a strong interannual variability in the projections can be observed. This variability is due to the variability in the wind speed projections. Figure 4.14 shows the projections of the energy supplied by the 15 MW OWT on a seasonal basis.

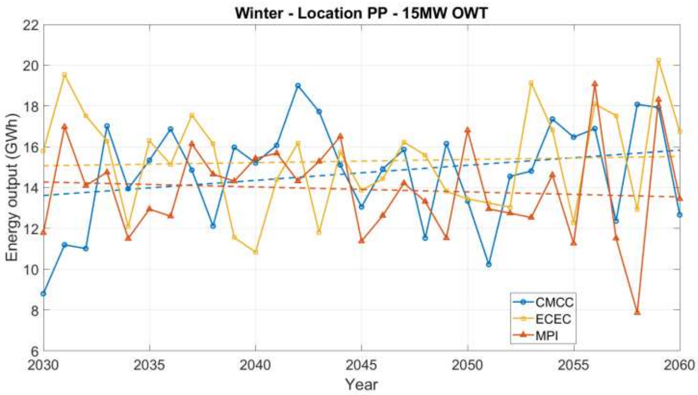

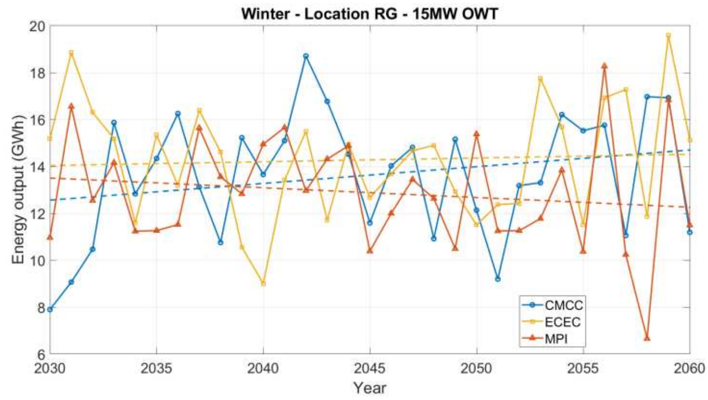
Winter - Location RG - 15MW OWT
Energy output (GWh)
Year
CMCC
ECEC
MPI

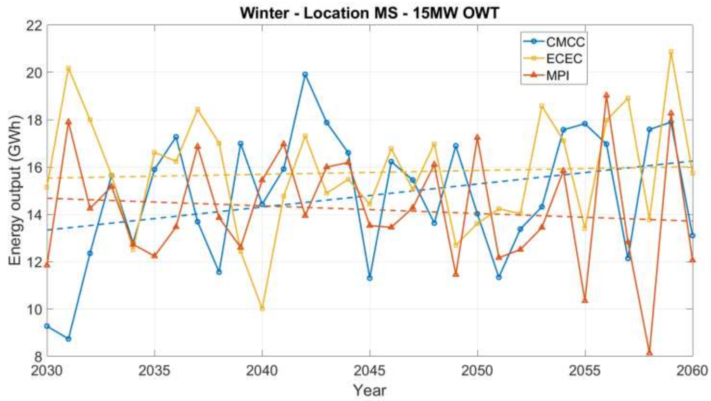
Winter - Location MS - 15MW OWT
Energy output (GWh)
Year
CMCC
ECEC
MPI

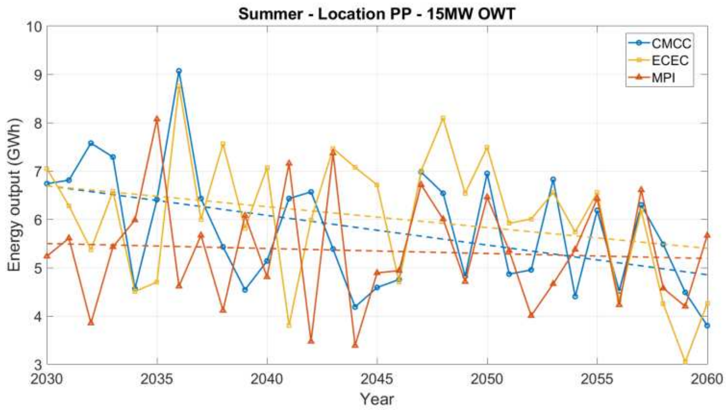
Summer - Location PP - 15MW OWT
Energy output (GWh)
Year
CMCC
ECEC
MPI

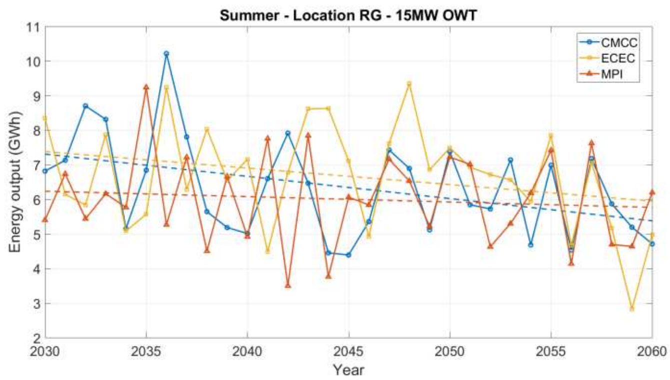
Summer - Location RG - 15MW OWT
Energy output (GWh)
Year
CMCC
ECEC
MPI

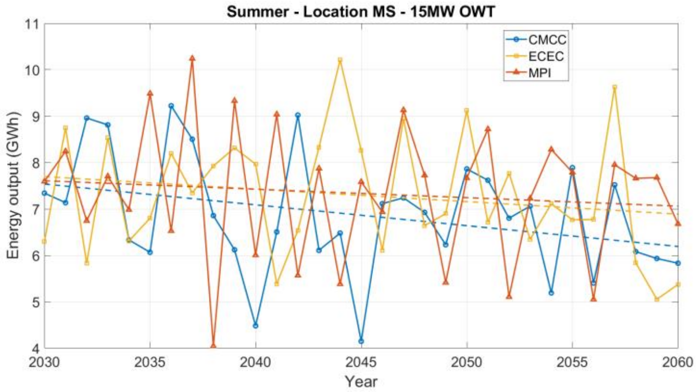

Figure 4.14. Trends of the projected energy output from a single 15 MW OWT in the three case study locations, on a winter and summer basis.

From Figure 4.14, it can be observed that on a summer basis decreasing trends in the energy produced are found for all three climate models, as also observed on an annual basis. On a winter basis, however, it cannot be inferred whether there will be a reduction or an increase in the energy produced in winter in the coming decades, since there is no consistency among the climate models. As done for the energy production evaluated using historical wind speed data, descriptive statistics are also computed for the results shown in Figure 4.13 and Figure 4.14 for each location and each climate model. Tables 4.2, 4.3, and 4.4 report the statistical results for the PP, RG, and MS locations, respectively.

Table 4 4.20. Mean, median, 95th percentile (P95), and standard deviation (STD) of the trends in the energy produced by the 15 MW OWT, evaluated deterministically using wind speed projections, for the PP location.

Climate model	Statistics(GWh)	Annual	Winter	Summer
CMCC	Mean	45.38	14.73	5.78
	Median	45.74	15.11	5.48
	P95	51.13	18.08	7.56
	STD	3.18	2.55	1.23
ECEC	Mean	45.43	15.30	6.05
	Median	44.87	15.74	6.19
	P95	51.94	19.51	8.07
	STD	3.04	2.44	1.34
MPI	Mean	43.18	13.91	5.34
	Median	43.70	14.09	5.35
	P95	48.78	18.25	7.36
	STD	3.55	2.35	1.16

Table 4 4.21. Mean, median, 95th percentile (P95), and standard deviation (STD) of the trends in the energy produced by the 15 MW OWT, evaluated deterministically using wind speed projections, for the RG location.

Climate model	Statistics (GWh)	Annual	Winter	Summer
CMCC	Mean	44.32	13.63	6.35
	Median	44.48	14.02	6.47

	P95	50.12	16.97	8.69
	STD	3.39	2.67	1.42
ECEC	Mean	44.52	14.28	6.67
	Median	44.21	14.67	6.78
	P95	50.92	18.80	9.22
	STD	3.02	2.48	1.51
MPI	Mean	42.25	12.88	6.01
	Median	42.62	12.63	6.07
	P95	47.89	16.82	7.84
	STD	3.69	2.43	1.34

Table 4 4.22. Mean, median, 95th percentile (P95), and standard deviation (STD) of the trends in the energy produced by the 15 MW OWT, evaluated deterministically using wind speed projections, for the MS location.

Climate model	Statistics (GWh)	Annual	Winter	Summer
CMCC	Mean	48.77	14.79	6.86
	Median	49.22	15.44	6.86
	P95	55.41	17.89	9.02
	STD	3.92	2.75	1.26
ECEC	Mean	49.89	15.77	7.29
	Median	49.60	15.66	6.90
	P95	56.61	20.12	9.61
	STD	3.47	2.43	1.32
MPI	Mean	48.64	14.19	7.33
	Median	49.22	13.85	7.66
	P95	54.36	18.25	9.48
	STD	3.80	2.47	1.46

It is important to compare the results obtained through wind speed projections (Tables 4.2–4.4) with those obtained using historical wind speed data (Table 4.1). For the PP location, on annual and winter basis, the CMCC and ECEC models provide statistics close to those obtained with historical data, while the MPI model projects energy values lower than the historical statistics. On a summer basis, the statistics of the projected energy production are close to the historical ones. For the RG and the MS locations, both on an annual and seasonal basis, the statistics of the projected energy production are lower than the historical ones. Finally, it is observed that the MS location is the one for which the climate models project the greatest reductions in production.

The Monte Carlo simulations are run and the cumulative means of the energy values obtained at each iteration is computed. The energy production values to which the Monte Carlo algorithm converges are close to the means of the energy production projections evaluated deterministically, both on an annual and a seasonal basis. As an example, the convergence trends of the Monte Carlo method on a winter basis are shown in Figure 4.15.

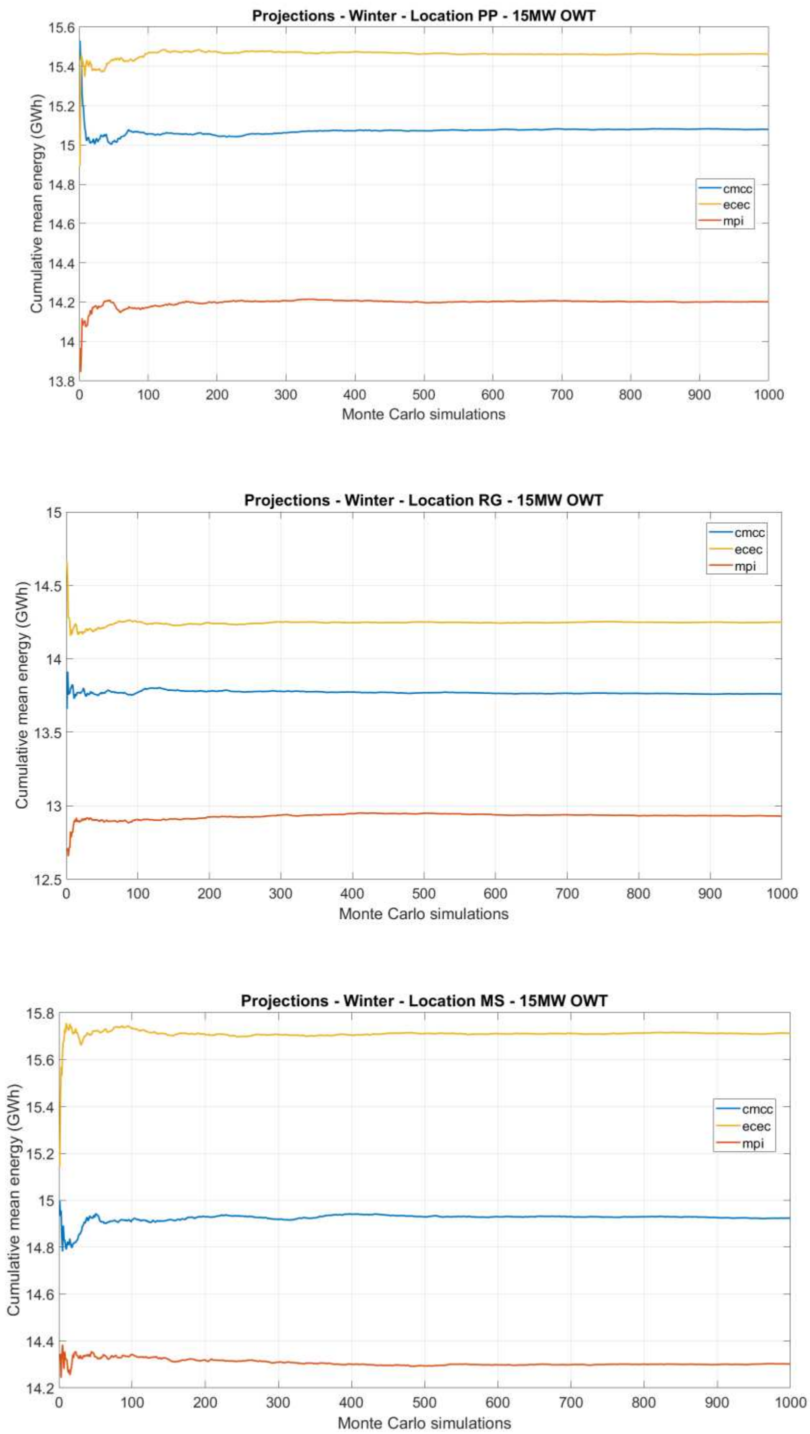

Figure 4.15. Convergence of the Monte Carlo algorithm for the cumulative means of the simulations of energy produced by the 15 MW OWT obtained using wind speed projections for the three case study locations.

From Figure 4.15, it can be observed that the Monte Carlo algorithm converges to the means evaluated in Tables 4.2, 4.3, and 4.4.

In conclusion, it would be interesting to understand what 'error' would have been made if historical wind speed data had been used instead of wind speed projections to evaluate the energy yield of an OWT in the coming decades. To do this, the trends of historical wind speed data are considered and extended to the 2030–2060 period, and the energy produced is evaluated on both an annual and a seasonal basis for each year. These resulting energy values, referred to as *historical energy trends*, are then compared with the energies previously evaluated using climate wind speed projections (*projection energy trends*). The difference between the historical energy trends and the projection energy trends is thus evaluated, both on an annual and a seasonal basis. Figure 4.16 shows the results on an annual basis.

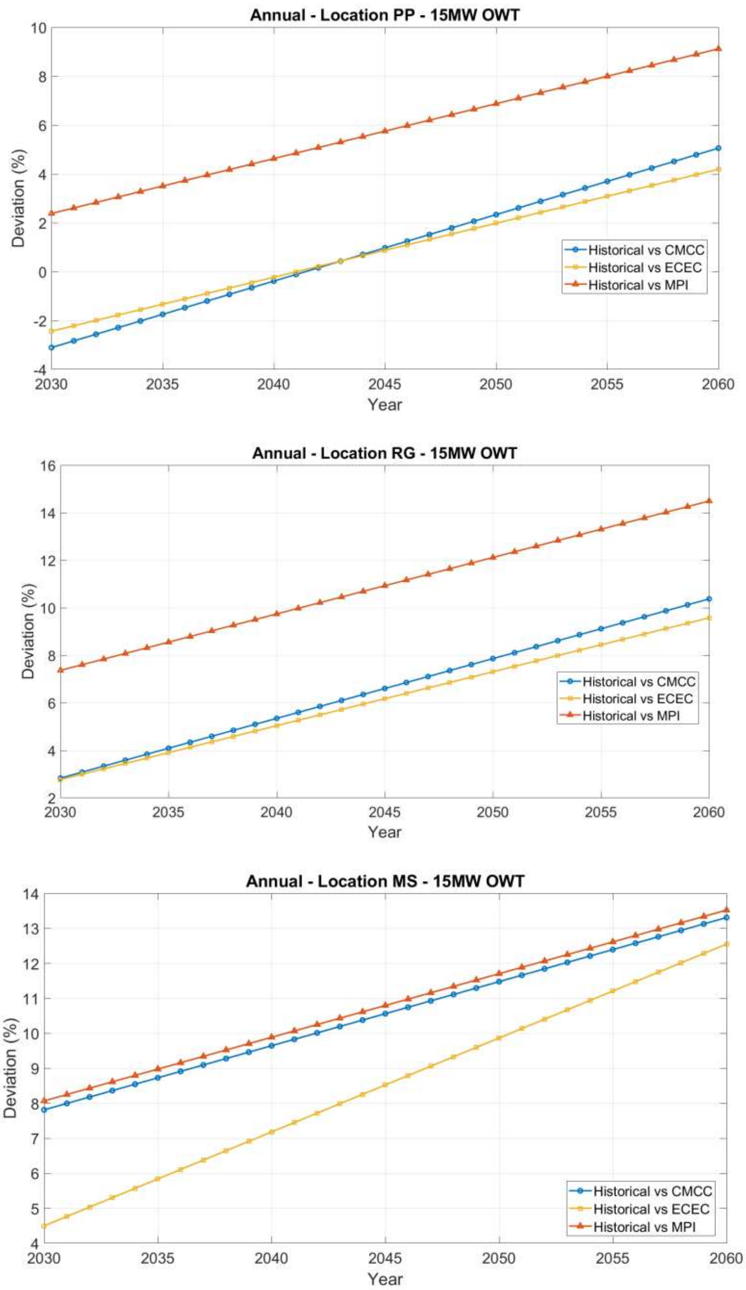

Figure 4.16. Deviations between the historical energy trends and the projection energy trends for the three case study locations for the 15 MW OWT on an annual basis.

Figure 4.16 reveals that for the RG and MS locations, the use of historical data would have led to an overestimation of energy production, whereas for the PP location the use of historical energy trends would have overestimated the production forecast, while for the CMCC and ECEC models the projection is overestimated from 2041 onward.

4.2.3 Discussion and conclusions

Energy yield analyses were conducted for a reference single OWT. Using historical wind speed data, the hourly profiles of power extractable from the wind were evaluated for the three locations considered. The correlation between these wind energy potential profiles of the three locations was then assessed, showing that these profiles are positively correlated. This aspect compromises the adequacy of the power system in Sicily, since if a plant at location A is not producing energy due to wind drought, it is very likely that the other sites would experience a similar wind drought, and thus do not compensate for the lack of production at location A.

Regarding the energy yield assessments of the 15 MW OWT, it was observed that on an annual and summer basis the climate models were consistent in projecting decreasing production trends, whereas on a winter basis the lack of agreement among the CMs did not allow conclusions to be drawn about a reduction or an increase in production in the coming decades. This reveals how essential it is to consider as many climate models as possible in climate change impact studies, in order to properly characterize the uncertainty of climate projections. A strong interannual variability of the energy produced was also observed on both an annual and a seasonal basis, due to the high variability of the wind speed projections from the climate models. This intrinsic variability of the projections implies that it is not possible to make robust assessments regarding the variability of wind power production in the coming decades.

The energy assessments were carried out using a Monte Carlo algorithm to account for both the uncertainty in the production of an OWT and the intrinsic uncertainty of climate model projections. The MC algorithm was then validated by comparing the results of the stochastic simulations with those obtained using the deterministic method. The implemented MC approach therefore allows the simulation of different energy production scenarios from the 15 MW OWT using both historical data (NEWA database) and climate projections (PECD 4.1 database). Finally, it was observed that if historical data had been used to evaluate energy production in the coming decades, the production would have been either overestimated or underestimated relative to climate projections, depending on the temporal interval considered (annual or seasonal), the location, and the climate model considered.

The study conducted can then be extended to the assessment of the production of a wind farm, considering the wake effects among OWTs and turbine aging, for economic performance evaluations and investment decision-making for existing or new wind farms. Moreover, to better characterize the uncertainty of climate projections, it would be useful to consider additional climate models and to account for further forcing scenarios in addition to SSP2-4.5 (i.e., SSP1-1.9, SSP5-8.5).

5. The influence of climate on the transmission grid: stochastic thermal modeling of transformers

European climate and energy targets set under the Fit-for-55 package require renewable energy sources (RES) to supply at least 65% of Italy's final electricity consumption by 2030. According to Terna's 2022 Scenarios Description Document, achieving this objective would require the installation of approximately 70 GW of additional RES capacity, mainly from photovoltaic and wind technologies [136]. Even more ambitious targets emerge under the REPowerEU plan, which could raise the required additional renewable capacity to over 80 GW [137]. The projected geographical distribution of future RES installations aligns with the spatial pattern of grid connection requests received by Terna, indicating a strong concentration—around 80%—in central and southern Italy [138].

Alongside this rapid expansion of renewables, the growing frequency and intensity of extreme weather events, particularly heat waves, is increasingly influencing electricity demand [139]. A clear example is provided by the extreme temperatures experienced in Italy in late July 2022, which caused a significant surge in electricity consumption, with demand peaks reaching approximately 55–57 GW [138].

In response to the energy and climate challenges facing the future Italian power system, the transition process requires the rapid deployment of targeted interventions aimed at increasing transmission capacity between market zones, mitigating network congestion, managing acceptable levels of renewable overgeneration, and enhancing power transfers from southern Italy—where renewable production is highest—to the northern regions, characterized by greater electricity demand.

To address congestion issues, the Italian transmission system operator has prioritized measures with relatively low investment costs, such as expanding the application of Dynamic Thermal Rating (DTR). By installing DTR systems on EHV–HV transmission lines, power flows can be dynamically adjusted according to real-time environmental conditions, allowing operational limits to exceed conservative static ratings based on design assumptions. This approach represents a fundamental shift in asset management, moving from a current-based paradigm to a temperature-driven operational strategy.

With regard to voltage regulation, transmission systems have increasingly experienced overvoltage conditions, particularly during periods of low electricity demand. In Italy, the 380 kV nodes most frequently affected by overvoltages are located in central and southern regions, such as Puglia [140]. To address voltage control in the EHV–HV network, Terna has recently introduced the concept of grid dispatching, which aims to maximize the self-regulation capability of the transmission system by fully leveraging existing assets and extending their operational use beyond traditional functions.

A notable example of this approach is the operation of autotransformers (ATRs) in tap staggering (TS) mode. In 2022, approximately 140 ATRs within the Italian power system were identified as suitable for this operating strategy [141]. The application rules and field test results of TS mode in Italy are presented in [142], while similar implementations in the UK are discussed in [143], which also highlight thermal constraints arising from transformer overloading. Further studies, such as [144], investigate the limiting factors of transformer overloading and how these constraints can be exploited to maximize current-carrying capability, whereas [145] analyzes variations in transformer load capacity as a function of current limits, oil temperature, and ambient conditions.

As expected, transformer loading capability is strongly influenced by ambient temperature, which is inherently stochastic and can therefore be described using statistical methods. Previous work, such as [146], has followed this approach by generating synthetic atmospheric profiles to study the Dynamic Thermal Rating of overhead transmission lines. To the authors' knowledge, however, a comparable statistical framework has not yet been applied to the thermal analysis of power transformers.

In this chapter, hourly synthetic temperature profiles are produced using a Monte Carlo methodology based on historical hourly temperature data from the past twenty years. These profiles are generated on a daily basis, from which synthetic mean values and 95th percentiles (P95s) are derived. The synthetic mean temperatures are representative of typical operating conditions on days without extreme heat, while the P95 values are used to characterize thermal conditions during extreme temperature events.

5.1 Statistical methods for the thermal modeling of transformers

This study seeks to introduce statistical approaches into the analysis of transformer DTRs, considering both normal operating conditions and periods of extreme heat. The proposed methodology relies on the stochastic generation of synthetic hourly ambient temperature profiles. The daily synthetic mean of these hourly ambient temperature profiles can be used to model transformer thermal behavior under normal loading conditions with standard insulation life expectancy, while the synthetic extreme values are intended to represent short-duration overload conditions involving a controlled reduction in transformer lifetime, such as those associated with tap-staggering operation. The following sections describe the procedure adopted to stochastically generate daily ambient temperature profiles with hourly resolution.

5.1.1 Statistical Fitting of Probability Distributions to Hourly Ambient Temperature Data

The stochastic modeling of the hourly ambient temperature (T_a, °C) experienced by a transformer is grounded in considerations drawn from IEEE Std C57.91-2011 [147]. In Chapter 6, the standard assumes a reference mean ambient temperature of 30°C, averaged over a 24-hour period, for transformer thermal ratings. To statistically represent such elevated mean temperature conditions, this study focuses on summer ambient temperature data. Summer is defined here as the months of June, July, and August, and hourly air temperature records spanning the past twenty years are used as the input dataset for the MC framework.

A key preliminary step involves fitting continuous probability distribution functions (CPDFs) to the summer T_a data for each of the twenty years considered. Parameter estimation is carried out using the MLE method [148]. The suitability of each candidate distribution is then assessed through a combination of goodness-of-fit (GOF) tests and statistical performance indices. Specifically, the chi-square (χ^2) test and the Kolmogorov–Smirnov (KS) test are employed, together with the normalized root mean square error (NRMSE), the normalized mean absolute error (NMAE), and the coefficient of determination (R^2).

The chi-square test is a statistical method used to assess how well observed categorical data match an expected distribution, making it a common choice for goodness-of-fit analyses. Similarly, the Kolmogorov–Smirnov test is a non-parametric test that evaluates the agreement between a sample distribution and a reference probability distribution. Both tests provide a way to determine whether observed data deviate significantly from theoretical expectations, helping to validate assumptions about the underlying distribution of the data.

For both the $\chi^2$and KS tests, the null hypothesis assumes that the observed data follow the selected theoretical CDF, denoted as $F_{\mathrm{th}}(x)$. By setting a significance level 0.05, the null hypothesis is accepted when the associated p-value satisfies $p > 0.05$. The χ^2test is implemented following the procedure described in [149], while the KS test evaluates the maximum deviation between the empirical CDF, $F_{\exp}(x)$, derived from the data and the theoretical CDF obtained from the fitted distribution, as expressed by equation (5.1):

$$\max_{1\le t\le T}\left(\left|F_{\exp}(x_t) - F_{th}(x_t)\right|\right) \tag{5.1}$$

where $F_{\exp}(x_t)$ and $F_{th}(x_t)$ are evaluated on the hourly data x_t; T is the cardinality of the set of input values for the experimental and theoretical CDFs.

The NRMSE is given by the following equation (5.2):

$$\mathrm{NRMSE} = \frac{1}{\Delta\theta}\sqrt{\frac{1}{T}\sum_{t=1}^{T}\left(F_{\exp}(x_t) - F_{th}(x_t)\right)^2} \tag{5.2}$$

where $\Delta\theta$ is the difference between the maximum and minimum of T_a values.

The NMAE is expressed by the following equation (5.3):

$$\mathrm{NMAE} = \frac{1}{\Delta\theta}\left(\frac{1}{T}\sum_{t=1}^{T}\left|F_{\exp}(x_t) - F_{th}(x_t)\right|\right) \tag{5.3}$$

where the symbols are defined as in the previous equations.

It was decided to normalize both the RMSE and the MAE using the difference between the maximum and minimum values, i.e., the range, rather than the mean, since in statistics both the mean and the range are used to normalize these indices [150]. Therefore, the two normalization approaches are equivalent.

Finally, the coefficient of determination $R^2$is evaluated using the following equation (5.4):

$$R^2 = 1 - \frac{\sum_{t=1}^{T}\left(F_{\exp}(x_t) - F_{th}(x_t)\right)^2}{\sum_{t=1}^{T}\left(F_{\exp}(x_t) - \overline{F_{\exp}(x_t)}\right)^2} \tag{5.4}$$

where $\overline{F_{\exp}(x_t)}$ is the mean of $F_{\exp}(x_t)$ values.

5.1.2 Monte Carlo algorithm implementation

The probability distribution that best represents the summer ambient temperature T_a data is selected to implement the Monte Carlo algorithm. The adopted approach is based on the inverse transform method, whereby uniformly distributed random numbers in the interval (0,1) are mapped through the ICDF of the fitted distribution to generate synthetic daily hourly ambient temperature profiles. This method requires the existence of a suitable continuous probability distribution; if no adequate fit is found, alternative stochastic techniques, such as the bootstrap method, must be employed.

The implemented algorithm consists of multiple independent MCSs, each producing a synthetic daily hourly T_a profile with uncorrelated hourly values, thus constituting a non-sequential MC approach. The methodology is validated for three Italian locations, and the statistical accuracy of the generated profiles is assessed using the NRMSE metrics introduced above.

5.1.3 Winding temperature assessment based on stochastic ambient temperature profiles

This section illustrates how the previously described algorithm is applied to the assessment of power transformer winding temperatures. The procedures and equations used to estimate transformer winding temperatures are well established in the literature and are governed by dedicated technical standards. Among these, IEC 60076-7 is an internationally recognized reference and is adopted in this study to calculate the winding hot-spot temperature (HST) of a power transformer, using the formulation provided in [151]:

$$
\begin{aligned}
T_{hst}(t) = T_a + \Delta T_{to,i} + \left[\Delta T_{to,r} \cdot \left(\frac{1 + R \cdot K^2}{1 + R}\right)^x - \Delta T_{to,i}\right] \cdot f_1(t) + \Delta T_{ht,i} \\
+ \left(H \cdot g_{wo,r} \cdot K^y - \Delta T_{ht,i}\right) \cdot f_2(t)
\end{aligned}
\tag{5.5}
$$

In the formulation, T_{hst}(°C) denotes the winding hot-spot temperature, while T_a(°C) represents the ambient temperature. The terms $\Delta T_{to,i}$(K) and $\Delta T_{to,r}$(K) correspond to the initial top-oil temperature rise and the steady-state top-oil temperature rise at rated losses, respectively. The parameter R (dimensionless) is the ratio between load losses at rated current and no-load losses, and K (dimensionless) is the transformer load factor. The exponents x and y characterize the thermal behavior of the oil and windings. The functions $f_1(t)$ and $f_2(t)$ describe the dynamic evolution of the top-oil temperature rise and the hot-spot-to-top-oil temperature gradient. The remaining parameters include $\Delta T_{ht,i}$(K), the initial hot-spot-to-top-oil gradient, H (dimensionless), the hot-spot factor, and $g_{wo,r}$(K), the average-winding-to-average-oil temperature gradient at rated current.

Although Equation (5.5) is well established in the literature, the novelty of this study lies in incorporating the stochastic nature of ambient temperature into its application. After generating synthetic temperature profiles, both their mean values and P95 are extracted. The synthetic mean temperatures, $T_{\text{syn-mean}}$, are used to model winding hot-spot temperatures under normal thermal conditions, while the synthetic P95 temperatures, $T_{\text{syn-95p}}$, are employed to represent transformer thermal behavior during extreme heat events. The results of the proposed methodology are presented in the following section.

5.2 Results

Hourly historical air temperature data are obtained from NASA's POWER project, which is derived from the MERRA-2 reanalysis product (spatial resolution of 0.5°×0.625°). The analysis considers twenty years of summer ambient temperature data, spanning from 2002 to 2021. Using recent historical data allows the effects of climate change on temperature trends to be implicitly captured and supports short-term future applicability, while longer-term assessments would require climate model projections.

The study focuses on three representative Italian locations—Foggia, Parma, and Mendrisio—selected to reflect distinct climatic regimes: Mediterranean, continental/Mediterranean, and continental/alpine, respectively. The subsequent sections present the results of the probability distribution fitting, the associated GOF metrics used to validate the MC algorithm, and the final application of the stochastic approach to the evaluation of transformer hot-spot temperature profiles.

5.2.1 Fitting campaign

Only continuous probability distributions whose domains are compatible with the observed hourly temperature data are considered for fitting. After an initial qualitative assessment based on graphical inspection, the goodness of fit is quantitatively evaluated using the statistical tests and indices described in Section 5.1.1.

For all three locations, at least one theoretical continuous probability distribution is found to adequately represent the data, allowing the MC algorithm to be implemented using the inverse transform method without resorting to alternative techniques such as the bootstrap. Based on the combined outcomes of the goodness-of-fit tests and indices, Table 5.1 reports both the best- and worst-performing distributions, with the normal distribution included as a reference benchmark.

Table 5.1. Best- and worst-fitting probability distributions for hourly summer t_a data, with the normal distribution included for comparison. NRMSE and NMAE values are expressed in percentages

Foggia					
Distribution	χ^2	KS	NRMSE	NMAE	R^2
Burr	1.0472	0.0896	0.12	0.09	0.9879
Gamma	0.5380	0.0770	0.11	0.09	0.9898
Normal	0.9376	0.0947	0.13	0.10	0.9863
Mendrisio					
Distribution	χ^2	KS	NRMSE	NMAE	R^2
Burr	0.0697	0.1298	0.18	0.14	0.9753
Gamma	24.7813	0.1235	0.18	0.14	0.9749
Normal	0.1527	0.1284	0.18	0.14	0.9743
Parma					
Distribution	χ^2	KS	NRMSE	NMAE	R^2
Burr	1.0454	0.1511	0.21	0.15	0.9633
Gamma	0.5594	0.1435	0.20	0.14	0.9663
Normal	0.8836	0.1536	0.22	0.15	0.9612

The results reported in Table 5.1 show that the probability distribution providing the best or worst fit to the ambient temperature data depends on the location. Based on the applied goodness-of-fit tests and statistical indices, the gamma distribution offers the best fit for the Foggia and Parma datasets, while the Burr distribution performs best for Mendrisio. These findings indicate that the normal distribution, which is commonly assumed for temperature data, does not provide the most accurate representation for any of the three locations considered. It is also noted that the gamma distribution can be successfully applied in this context because the analysis is limited to summer temperatures, which are strictly positive and therefore compatible with the domain of the gamma distribution.

5.2.2 MC algorithm validation

After fitting the probability distributions, the one providing the best fit is selected to implement the MC algorithm described in Section 5.1.2. Each MCS generates a synthetic daily hourly profile of ambient temperature, from which the daily mean and P95 values are extracted. To ensure statistical reliability, a 95% confidence interval is considered, which requires more than 1052 Monte Carlo simulations according to [146]. In this study, 1500 simulations are performed for each summer day, from June 1st to August 31. Consequently, 1500 synthetic daily hourly temperature profiles are obtained for each summer day.

To evaluate the performance of the MC algorithm, two metrics are computed for each simulation: the normalized RMSE for the mean ($NRMSE_{\text{mean}}$) and for the standard deviation ($NRMSE_{\text{std}}$). The standard deviation is included to assess how well the MC algorithm reproduces the variability observed in historical T_a profiles. For a given summer day, the means of the synthetic temperature profiles are calculated, and the deviations between these means and the historical daily mean T_a values over the past twenty years are determined. These differences are then used in the $NRMSE_{\mathrm{mean}}$ calculation, with an analogous procedure applied for $NRMSE_{\mathrm{std}}$ using STDs instead of means. $NRMSE_{\mathrm{mean}}$ is given by the following equation:

$$\mathrm{NRMSE_{mean,k}} = \frac{1}{\Delta \mathrm{m_{hst}}} \sqrt{\frac{1}{\mathrm{n}} \sum_{\mathrm{i=1}}^{\mathrm{n}} \left(\mathrm{m_{syn}} - \mathrm{m_{hst,i}}\right)^2} \tag{5.6}$$

where k denotes the k-th MCS and i is an index ranging from 1 to 20, as 20 years of historical data are considered. m_{syn} represents the mean value computed from the synthetic daily temperature profile, while m_{hst} is the historical daily average temperature for a given summer day in each year of the dataset. Δm_{hst} denotes the range of historical daily averages for that summer day, calculated as the difference between the maximum and minimum average values.

For the standard deviation, equation (5.6) is modified as follows:

$$\mathrm{NRMSE_{std,k}} = \frac{1}{\Delta \mathrm{STD_{hst}}} \sqrt{\frac{1}{\mathrm{n}} \sum_{\mathrm{i=1}}^{\mathrm{n}} \left(\mathrm{std_{syn}} - \mathrm{std_{hst,i}}\right)^2} \tag{5.7}$$

Following the same calculation procedure as applied for the mean.

These new metrics, reported in Equations (5.6) and (5.7), have been introduced to quantify the deviation between historical means and those of the simulated profiles, and similarly for the standard deviations. This is done to verify whether the implemented Monte Carlo method is capable of generating synthetic temperature profiles with mean and variability close to the historical ones. Indeed, the proposed approach is intended to carry out statistical simulations of different temperature scenarios, and the goal is to assess whether these reliably capture the mean values and variability of historical temperature time series. Moreover, this type of analysis is consistent with the simulations performed in adequacy studies. In such analyses, the Monte Carlo method is used to run hundreds of MCSs, from which the expected value is then evaluated. Therefore, quantifying how well the implemented approach reproduces the statistical mean and variability of temperatures makes it possible to assess whether it can provide reliable operating scenarios for transformers in adequacy analyses. For all these reasons, $NRMSE_{\mathrm{mean}}$ and $NRMSE_{\mathrm{std}}$ are introduced because, compared to the classical NRMSE found in the literature, they are considered more suitable indices for validating the implemented Monte Carlo method, in light of the objectives of this study.

Figures 5.1–5.3 illustrate the NRMSE trends for both the mean and standard deviation of synthetic temperature profiles across the three locations, shown for one representative day from the middle of each summer month.

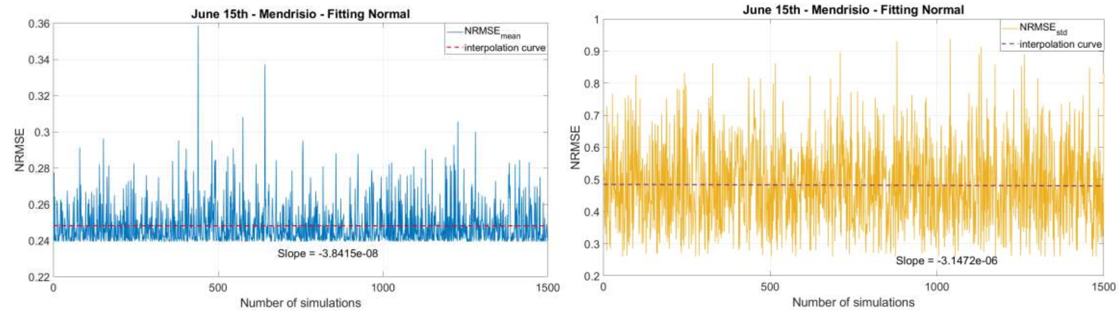

(a) (b)

Figure 5.1. NRMSE values of: (a) the mean and (b) the STD evaluated for each of the 1500 MCSs, fixing the date as June 15th, for the location of Mendrisio.

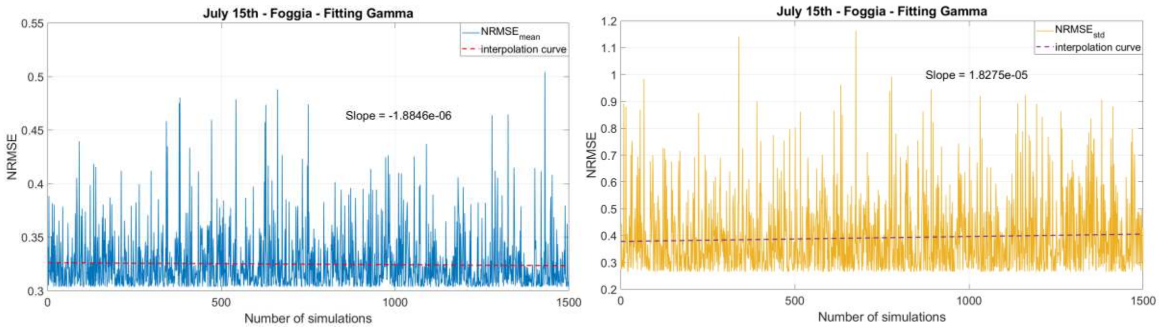

(a) (b)

Figure 5.2. NRMSE values of: (a) the mean and (b) the STD evaluated for each of the 1500 MCSs, fixing the date as July 15th, for the location of Foggia.

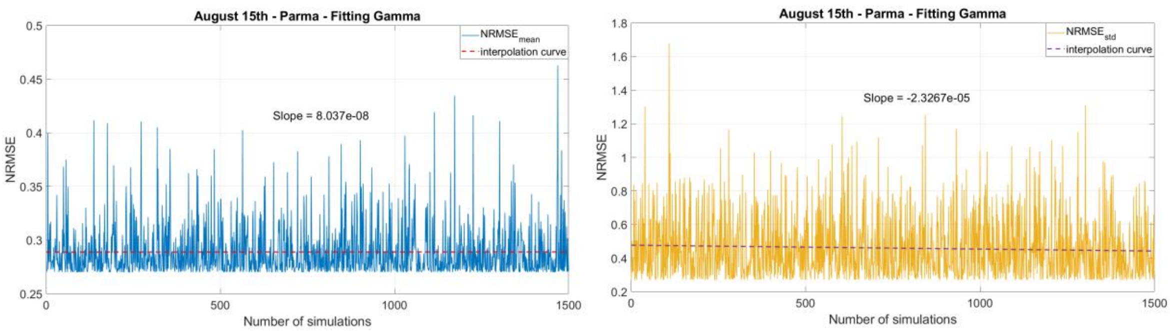

(a) (b)

Figure 5.3. NRMSE values of: (a) the mean and (b) the STD evaluated for each of the 1500 MCSs, fixing the date as July 15th, for the location of Parma.

From Figures 5.1 (a), 5.2 (a), and 5.3 (a), it can be seen that the $NRMSE_{\mathrm{mean}}$ values are all below one, with the interceptions of their respective trend lines falling under 0.4 for all three locations. This indicates that the results are generally acceptable and that the implemented algorithm performs reliably across different climates. Mendrisio shows particularly good results, as the normal distribution fitted to this location yielded better GOF outcomes compared to the normal distributions used for Foggia and Parma (see Table 5.1). Moreover, for Mendrisio, the normal distribution outperformed the gamma distributions used for Foggia and Parma. Although the Burr distribution provided the best GOF for Mendrisio, it was not used in the MC algorithm due to convergence issues.

Figures 5.1 (b), 5.2 (b), and 5.3 (b) show that the $NRMSE_{\mathrm{std}}$ values are higher than the $NRMSE_{\mathrm{mean}}$ values, both in terms of minimum and maximum values and in the intercept of the trend line. Additionally, the $NRMSE_{\mathrm{mean}}$ values tend to cluster around a lower bound below which none of the 1,500 simulations fall, a pattern not observed for the $NRMSE_{\mathrm{std}}$ values. When comparing the $NRMSE_{\mathrm{mean}}$ and $NRMSE_{\mathrm{std}}$ results, no clear trend is observed across the 1,500 MCSs, further confirming the stochastic nature of the implemented MC algorithm.

5.2.3 The hot-spot temperature curves

The transformer winding hot-spot temperatures are assessed under steady-state conditions, so equation (5.5) is simplified to become:

$$T_{hst} = T_a + \Delta T_{to,r} \cdot \left[\frac{1 + R \cdot K^2}{1 + R}\right]^x + H \cdot g_{wo,r} \cdot K^y \tag{5.8}$$

where the values assigned to the respective terms are [143]: $R = 10.2$, $\Delta T_{to,r} = 46.7$ °C, $x = 0.8$, $H = 1.3$, $g_{wo,r} = 6.9$ °C, $y = 1.3$. K varies from 0.1 to 1 with steps of 0.1.

As described in Section 5.1.3, the synthetic mean and P95 values of the simulated hourly temperature profiles are used for each summer day, with transformer load levels varying from 0.1 to 1. Figures 5.4 and 5.5 show the corresponding HST curves of the transformer windings for a midsummer day.

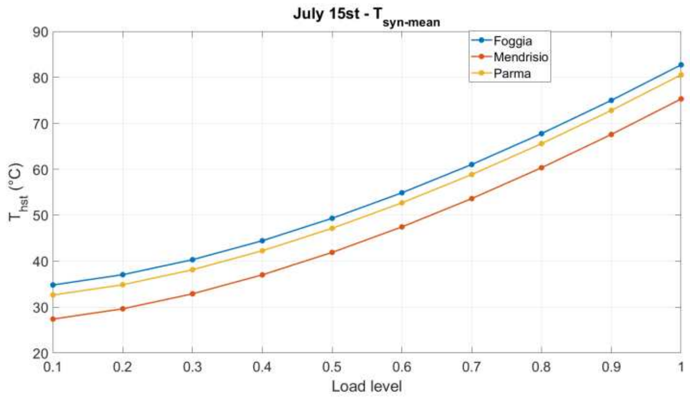

Figure 5.4. HST curves derived from the daily average values of the synthetic ambient temperature profiles.

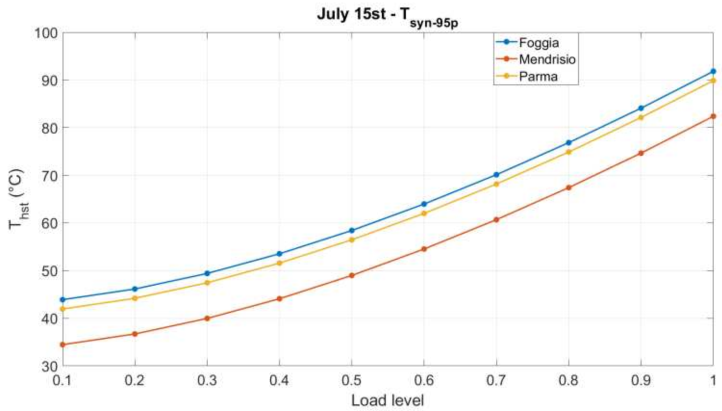

Figure 5.5. HST curves derived from the 95th percentile of the daily synthetic ambient temperature profiles.

As expected, using the P95 instead of the mean shifts the HST curves upward. Additionally, notable differences are observed between the HST curves of the three locations, particularly for Mendrisio (alpine climate) compared to the others. This demonstrates how the applied methodology effectively reflects the distinct climatic characteristics of each site.

5.3 Conclusions

In this chapter, a stochastic modeling approach for ambient temperature was developed to introduce a novel perspective in studying the thermal impacts on transformer windings. Incorporating statistical methods into the thermal analysis of network components enables the simulation of multiple parallel scenarios and allows integration of these stochastic-thermal results into broader statistical analyses of power systems, such as adequacy studies.

The results of the probability distribution fitting reveal both spatial and temporal variability: the CPDF that best fits the data differs by location, and the suitable CPDF also varies with the time of year (e.g., winter versus summer).

The NRMSE values calculated for both the mean and standard deviation are below one, indicating that the algorithm performs satisfactorily for the study's purposes. Moreover, no clear trends were observed in the NRMSE values across the 1500 MCSs, and the slopes of the interpolating lines were minimal, suggesting that increasing the number of simulations would not significantly improve the results.

The evaluation of the transformer winding HST curves confirms the practical applicability of the proposed stochastic approach.

For future work, the same MC methodology could be extended to the thermal analysis of overhead transmission lines, incorporating additional atmospheric variables that affect the performance and reliability of high-voltage line insulations.

6. Study of the relationship between electricity demand and air temperature during heat waves

International and national energy strategies are driving a growing integration of ND-RESs into electric power systems (EPSs) worldwide [152]. While this transition contributes to the reduction of carbon dioxide emissions, it also increases the variability of electricity supply, as ND-RES generation strongly depends on meteorological conditions [153]. At the same time, electricity demand is influenced by atmospheric factors such as air temperature and humidity [154]. For effective EPS planning and operation, it is therefore essential to assess the strength of the relationship between weather variables and both electricity production and consumption.

With specific regard to electricity demand, numerous studies have investigated the relationship between atmospheric variables—most notably temperature and humidity—and demand using simple or multiple linear regression models [154] [155] [156]. However, before applying such statistical models, it is advisable to first quantify the degree of linear dependence between weather variables and electricity demand [157]. Despite its relevance, this topic has received limited attention in the literature, and existing studies typically rely on coarse temporal resolutions, such as monthly [154] [158] or daily data [159] [160], rather than hourly demand profiles. This study seeks to address this gap by evaluating the correlation between electricity demand and temperature, as well as both relative and specific humidity, at daily and hourly time scales.

When examining the relationship between weather conditions and electricity demand, it is also crucial to account for long-term climatic trends. Average temperatures are rising over time, and extreme heat events, including heat waves (HWs), are becoming more frequent and intense. As a result, analyzing how the correlation between atmospheric variables and demand evolves over time provides valuable insight into the changing nature of this relationship. Moreover, given the increasing occurrence of heat waves, understanding their specific impact on electricity demand is of particular importance [161].

Previous studies have investigated the effects of heat waves on electricity consumption [162] [163] [164], including the modeling of peak demand during extreme heat events [165]. However, a comprehensive analysis of how the demand–weather relationship differs between heat wave periods and typical summer conditions is still lacking. In particular, little attention has been paid to evaluating how correlations between atmospheric variables and demand change during heat waves. This chapter aims to fill this gap by quantifying the impact of heat waves on electricity demand, focusing on demand increases, variations in the slope of linear regression relationships between demand and atmospheric variables, and changes in correlation strength during extreme heat conditions.

Since there is no universally accepted definition of a heat wave [166], different climatic indices based on absolute or relative thresholds are commonly employed to identify extreme heat events. In this work, HWs are detected using a new Warm Spell Duration Index (WSDI), which considers both daily maximum and minimum temperatures, enabling the identification of extreme heat during both daytime and nighttime. In addition, given the importance of minimum demand levels in EPS operation, absolute temperature thresholds are applied to detect extreme nighttime heat events, known as tropical nights (TRs). The combined use of relative and absolute criteria allows for an assessment of whether heat waves are associated with tropical nights, and vice versa. Finally, in view of projections indicating that the Mediterranean region will become a hotspot of global warming [167], Sicily—one of Italy's major electricity market zones—is selected as the case study for the analyses.

In the following paragraphs, the study methods and the corresponding results obtained are described in detail

6.1 Methods

To address the objectives outlined above, analyses are performed on both meteorological variables and electricity demand at annual and seasonal scales, focusing specifically on spring and summer. This approach allows for an investigation of how the relationships between atmospheric conditions and electricity consumption evolve when shifting from annual to seasonal analyses, as well as between spring and summer periods. The comparison between these two seasons is motivated by their differing climatic characteristics: during spring, relatively mild weather conditions may reduce the sensitivity of electricity demand to temperature and humidity, whereas in summer demand is more likely to be strongly driven by meteorological factors. Summer is defined as the months of June, July, and August (JJA), while spring includes March, April, and May (MAM).

The selected case study is Sicily, which represents a distinct market zone and a major load center within the Italian power system. Island-based electric power systems are of particular technical and scientific interest due to their greater operational and maintenance complexity compared to mainland systems [168]. The following paragraphs describe in detail the methodological framework adopted in the study.

6.1.1 Database used

The meteorological dataset employed in this analysis is derived from the Modern-Era Retrospective Analysis for Research and Applications, Version 2 (MERRA-2), accessed through the NASA Langley Research Center (LaRC) POWER Project, supported by the NASA Earth Science/Applied Science Program [83]. The data are provided on a spatial grid with a resolution of $0.5° \times 0.625°$ in latitude and longitude. Both daily and hourly records of air temperature (°C), relative humidity (RH, %), and specific humidity (SH, g/kg) are utilized. For temperature, the analysis includes daily maximum temperature (T_X, °C), daily minimum temperature (T_N, °C), the diurnal temperature range (DTR, °C), and hourly air temperature at 2 m above ground level (T_{2m}, °C).

Electricity demand data are obtained from the transparency platform of the ENTSO-E [169]. The dataset consists of hourly power demand values (MW) for the Sicilian market zone and represents total aggregated demand, including industrial, commercial, and residential consumption. All data processing and analyses are carried out using the MATLAB software environment [133].

6.1.2 Correlation analysis

To investigate the relationship between atmospheric variables—specifically temperature and humidity—and electricity demand, a correlation analysis based on the sample Pearson correlation coefficient *r* is carried out (evaluated using equation 4.6).

The correlation analysis is performed over multiple temporal scales, including the full annual dataset as well as the corresponding spring and summer periods. Since electricity demand is available at an hourly resolution, its relationship with daily meteorological variables is evaluated by computing daily minimum (Dem_N), maximum (Dem_X), and mean demand values (Dem_{mean}). For instance, when considering daily maximum temperature (T_X), correlations are examined for the variable pairs (T_X, Dem_N), (T_X, Dem_X), and (T_X, Dem_{mean}). A similar procedure is applied to assess the strength of the relationship between electricity demand and other daily atmospheric indicators, including DTR, T_N, RH, and SH.

In addition, correlations at the hourly scale are investigated by directly relating hourly electricity demand to hourly atmospheric variables, namely air temperature at 2 m (T_{2m}), relative humidity, and specific humidity.

6.1.3 'Diurnal' and 'nighttime' heat waves and tropical nights

An additional aspect of interest is the evaluation of the relationship between atmospheric conditions and electricity demand during heat wave events. Since electricity consumption is influenced by both temperature and humidity, and heat waves are characterized by persistently extreme values of these variables, it is important to investigate how such events affect electricity demand patterns. To examine these effects, heat wave periods must first be identified across different summers, after which electricity demand behavior during those intervals can be analyzed.

Heat waves are identified in this study using a criterion based on the Warm Spell Duration Index (WSDI), a climate indicator defined by the Expert Team on Climate Change Detection and Indices (ETCCDI) [170]. Using daily maximum temperature data from a 30-year reference period (1981–2010), the 90th percentile of maximum temperature is calculated for each calendar day, employing a five-day moving window. These percentiles, hereafter referred to as TX90th calendar percentiles, serve as thresholds against which daily maximum temperatures (T_X) of individual years are compared. A heat wave is defined as a sequence of at least six consecutive days during which T_X exceeds the corresponding TX90th calendar percentile. As this definition relies on maximum temperatures, the resulting events are hereafter referred to as *diurnal heat waves*.

The ETCCDI indices do not include an equivalent WSDI metric based on minimum temperatures. However, since minimum temperatures can significantly affect nighttime electricity demand, particularly minimum load levels, it is useful to identify heat waves occurring during nighttime hours. To this end, a nocturnal Warm Spell Duration Index (WSDI-n) is introduced. This index is constructed by comparing daily minimum temperatures of a given year with the 90th calendar percentiles derived from minimum temperature data over the same 30-year reference period (1981–2010), again using a five-day centered window. A *nighttime heat wave* is here identified when daily minimum temperatures exceed the corresponding percentile threshold for at least six consecutive days.

Elevated nighttime temperatures may lead to increased electricity demand, as buildings are less able to release the heat accumulated during daytime hours, thereby intensifying the need for space cooling. In addition to detecting nighttime heat waves, another ETCCDI index related to minimum temperatures is considered: the number of tropical nights (TR). This index identifies days on which the minimum temperature exceeds a predefined absolute threshold. While a threshold of 20 °C is commonly used, absolute thresholds can be adapted to the climatic characteristics of the region under study. In this work, a threshold of 25°C is adopted (hereafter referred to as TR25), as summer nighttime temperatures in Sicily frequently exceed 20 °C. Consequently, a lower threshold would be less effective in isolating nights associated with particularly high cooling demand.

6.1.4 The degree of correlation between energy demand and heat waves

After identifying both daytime and nighttime heat waves, the next step is to investigate whether electricity demand during these events is higher than during comparable periods not affected by heat waves. To this end, reference periods of equal duration to the corresponding heat wave are selected, ensuring the same number of weekdays, Saturdays, Sundays, and public holidays (in this way, the results are not influenced by factors other than environmental ones). During these reference periods, daily maximum temperatures remain below the TX90th calendar percentile thresholds, and the selected days are positioned at least two days away from the start or end of any heat wave simultaneously affecting the analyzed locations. These reference intervals are hereafter referred to as *outside heat wave* periods.

Subsequently, the sensitivity of electricity demand to temperature and humidity is examined by estimating the slope of the linear relationship between demand and each atmospheric variable. This analysis is carried out using hourly data only, as daily samples would be insufficient in size to ensure statistically robust results. The regression slopes are computed by normalizing hourly demand values with respect to the mean hourly demand of the corresponding time frame (annual, spring, or summer).

Finally, the hourly correlation coefficients calculated for annual and seasonal periods are further analyzed by comparing conditions during heat wave episodes—both diurnal and nocturnal—with outside heat wave periods.

6.2 Results

For the Sicilian market zone, nine years of electricity demand data (2015–2023) are available from the ENTSO-E Transparency Platform. Accordingly, an equivalent nine-year period of meteorological data is used to investigate the relationships between atmospheric variables and electricity demand. Weather variables are extracted for three of Sicily's main electricity load centers: Catania (CT), Messina (ME), and Palermo (PA). The corresponding geographical coordinates of the selected locations are 37.44° N, 15.00° E for Catania; 38.12° N, 15.47° E for Messina; and 38.08° N, 13.35° E for Palermo.

A preliminary examination of the electricity demand time series reveals that, across all nine years, summer consistently accounts for the largest share of annual electricity consumption. On average, summer demand represents approximately 30% of the total yearly demand, while spring, autumn, and winter contribute about 23%, 24%, and 25%, respectively. These findings support the expectation that, in Southern European regions, cooling-related electricity consumption plays a more prominent role in power system operation than heating demand. The following paragraphs present the results obtained by applying the methodologies described in the Methods section.

6.2.1 The degree of correlation between energy demand and atmospheric variables

First, daily correlations for the variable pairs described in the Methods section were calculated for all the case study locations. These correlations were assessed on annual, spring, and summertime scales for each of the nine years of data. However, not all years produced statistically significant results ($p > 0.05$). Figure 6.1 presents boxplots of the correlation coefficients, *r*, for the variable pairs that showed statistical significance in each year, using Messina as an example, as similar patterns were observed for Catania and Palermo.

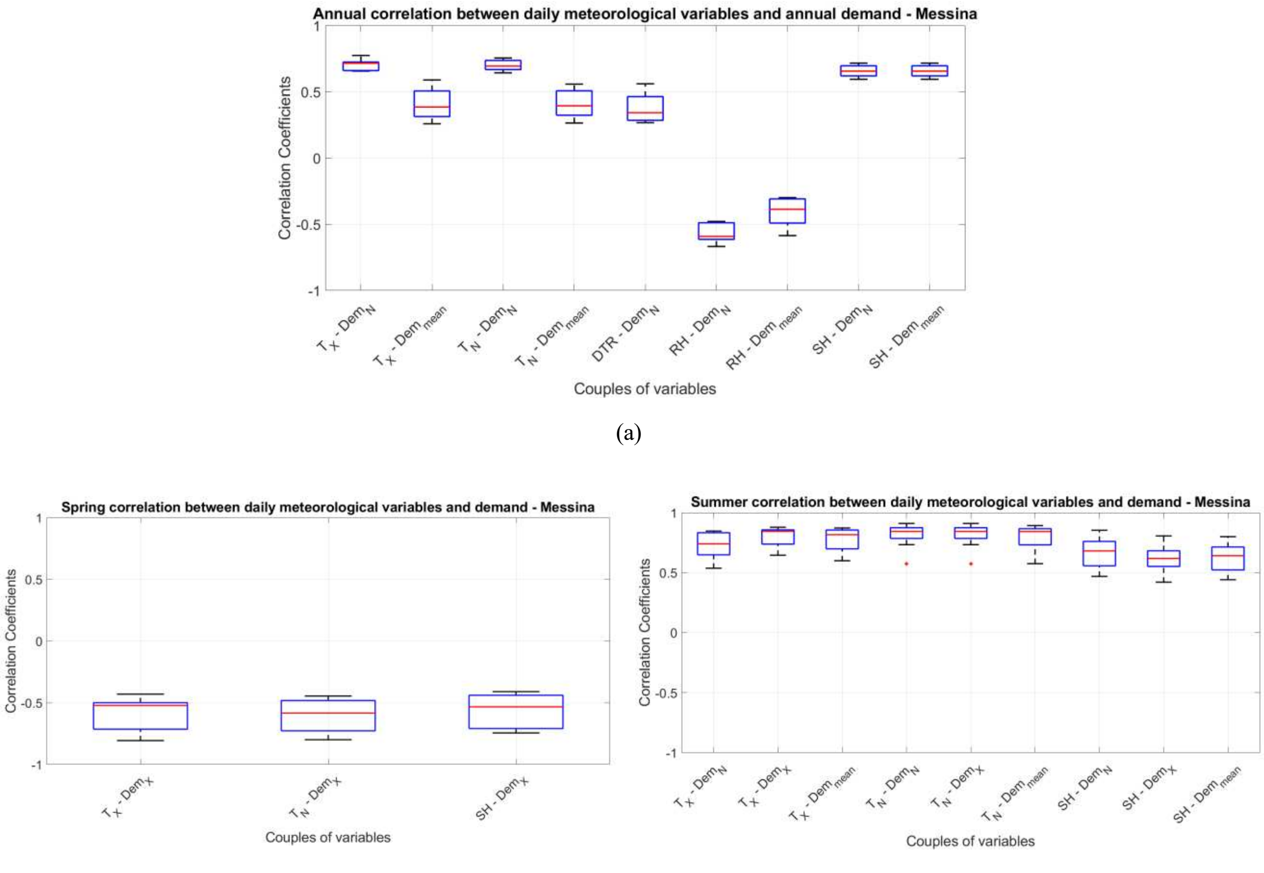

(a)

(b) (c)

Figure 6.1. Boxplots of daily correlation coefficients r calculated for each year of data at the Messina location: a) annual periods, b) spring periods, and c) summer periods. Only variable pairs that yielded statistically significant correlation values in each year are shown (p<0.05).

Figure 6.1 shows that, for a given pair of variables—such as (T_X, Dem_X)—statistically significant correlations are observed during spring but not when considering the full annual period, with the absolute values of the Pearson correlation coefficient exhibiting opposite signs when moving from spring to summer. Overall, across all three analyzed locations, both maximum and minimum temperatures display a positive correlation with electricity demand on annual and summer scales, with stronger relationships observed during the summer months, whereas a negative correlation emerges during spring.

The relationship between humidity variables (both relative and specific) and electricity demand appears more nuanced, as both the sign and magnitude of the correlations vary across seasons and when compared to annual values. In spring, the observed negative correlation between specific humidity and demand is physically plausible, as higher humidity—often associated with cloudy conditions—can coincide with milder temperatures, leading to reduced energy consumption. Similar results are observed for the locations of Catania and Palermo.

While boxplots offer a qualitative view of the spread of the estimated correlation coefficients, they do not convey quantitative metrics such as the mean values. For this reason, Figure 6.2 presents bar charts illustrating the mean values of the distributions of the computed r coefficients.

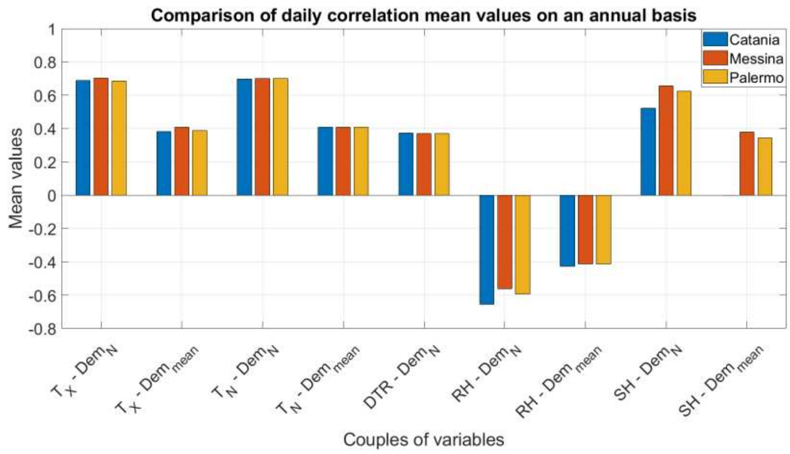

(a)

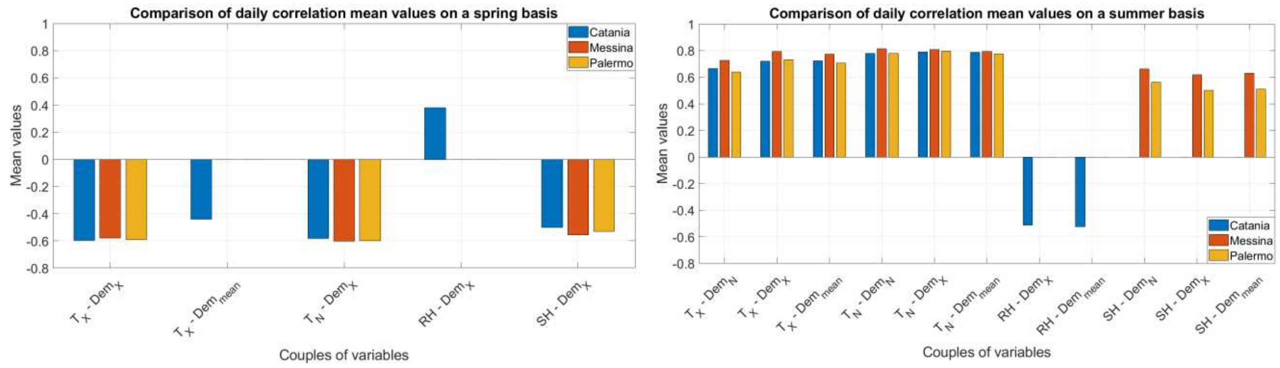

(b) (c)

Figure 6.2. Bar charts showing the mean values of the correlation coefficient r for Catania, Messina, and Palermo, computed on: a) an annual basis, b) during spring, and c) during summer. Only variable pairs yielding statistically significant results are reported.

The comparison among the different locations, illustrated in Figure 6.2, shows that even when the same temporal scale is considered (annual, spring, or summer), the atmospheric variable–demand pairs exhibiting statistically significant correlations vary across locations. For instance, during the summer period, the correlation between specific humidity and electricity demand is statistically significant in Catania ($p > 0.05$) but not in Palermo or Messina.

Following the analysis based on daily data, the next step involves assessing the correlation between hourly atmospheric variables and electricity demand. This correlation analysis considers the same set of atmospheric variables described in the Methods section. The results for the Catania location are presented in Table 6.1, which also reports the Pearson correlation coefficients for years in which the correlations are not statistically significant. The results for Messina and Palermo are not reported, as they are close to those for Catania.

Table 6.1 also reports the mean annual and seasonal values of hourly air temperature, $\overline{T_{2m}}$, in order to assess whether higher average temperatures over a given time period are associated with an increase in the corresponding correlation coefficients.

Table 6.1. Hourly values of the r coefficient for the Catania location

Year	$\overline{T_{2m}}$			T_{2m}-Dem			RH-Dem			SH-Dem		
	Yr	Spr	Sum	Yr	Spr	Sum	Yr	Spr	Sum	Yr	Spr	Sum
2015	17.1	14.4	25.6	0.30	0.18	0.63	-0.33	-0.24	-0.42	0.12	-0.05	0.20
2016	17.3	14.9	25.5	0.27	0.14	0.48	-0.27	-0.18	-0.35	0.08	-0.03*	0.04*
2017	16.9	14.9	27.2	0.28	0.13	0.54	-0.30	-0.15	-0.42	0.05	0.01*	-0.06
2018	17.1	15.2	25.1	0.25	0.07	0.47	-0.27	-0.10	-0.35	0.09	-0.02*	0.02*
2019	17.1	13.6	27.0	0.33	0.08	0.51	-0.33	-0.09	-0.32	0.15	0.00*	0.13
2020	17.4	15.1	26.2	0.35	0.05	0.59	-0.31	-0.11	-0.42	0.18	-0.08	0.12

2021	17.6	14.3	28.0	0.45	0.02*	0.64	-0.45	-0.16	-0.50	0.08	-0.18	-0.07
2022	18.0	14.1	28.0	0.42	0.02*	0.50	-0.40	-0.15	-0.36	0.18	-0.15	-0.02*
2023	17.9	14.4	26.9	0.53	0.25	0.74	-0.55	-0.38	-0.65	0.09	-0.17	-0.30

*Values not statistically significant ($p > 0.05$)

Based on the results reported in Table 6.1, several observations can be made for the (T_{2m}-Dem) variable pair. The positive relationship between temperature and electricity demand identified at daily resolution on annual and summer scales is also confirmed when considering hourly correlations. Moreover, the strengthening of the temperature–demand relationship when moving from annual to summer periods, already observed in the daily analysis, becomes substantially more pronounced at the hourly level. In contrast, correlations during spring are close to zero. Notably, the highest correlation coefficients—both annually and seasonally—are observed in 2023, even though this year does not exhibit the highest average annual or summer temperatures.

With respect to relative humidity, hourly correlation coefficients are statistically significant for all years and across all locations, in contrast to the daily analysis, and consistently indicate a negative relationship with electricity demand. The correlation between specific humidity and demand exhibits the same sign as in the daily analysis, although with a lower magnitude. However, the strength of the (SH, Dem) correlation is markedly higher during summer compared to spring and annual periods.

Overall, across the three analyzed locations, spring emerges as the only season in which statistically non-significant correlations are observed for certain years. In summary, the results suggest that during spring, hourly electricity demand is more strongly influenced by air humidity than by temperature.

6.2.2 Identification of diurnal and nighttime heat waves and tropical nights

For each location, the nine-year time series of daily maximum and minimum temperatures are compared against the 90th calendar percentile thresholds for each summer within the study period. This procedure allows the identification, on a year-by-year basis, of the occurrence of diurnal and/or nighttime heat waves during the summer months.

The analysis shows that all three locations experienced diurnal heat waves during the summers of 2017, 2019 (with a weaker intensity in Messina compared to Catania and Palermo), 2021, 2022, and 2023. Periods characterized by diurnal heat waves are often accompanied by nighttime heat waves as well, although their durations do not necessarily coincide. Conversely, in certain years—such as 2015 and 2020—nighttime heat waves occurred in the absence of daytime events. Figure 6.3 illustrates the trends of daily maximum and minimum temperatures relative to their respective threshold values for the three Sicilian sites during the summer of 2022.

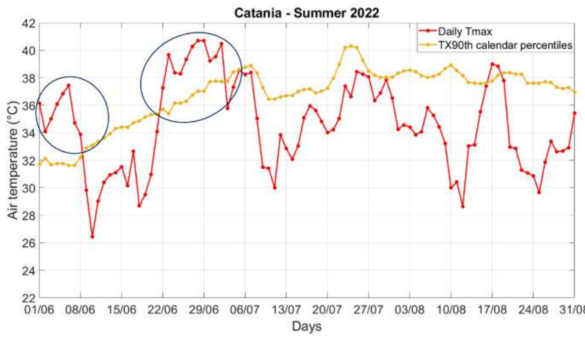

(a)

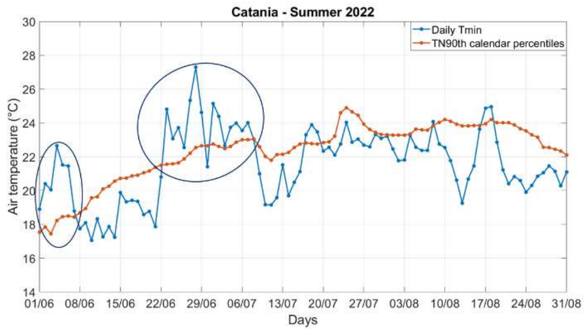

(b)

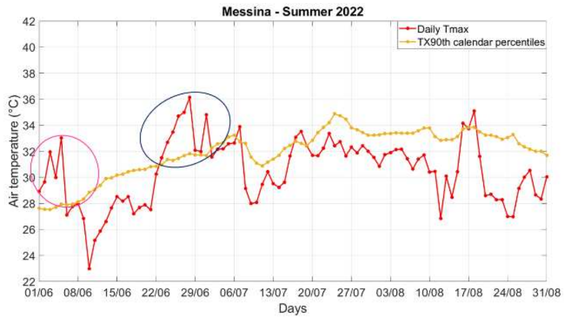

(c)

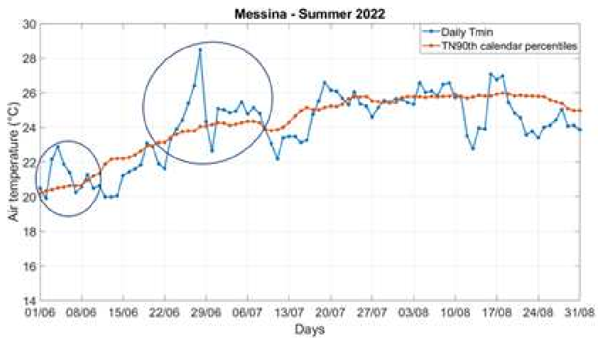

(d)

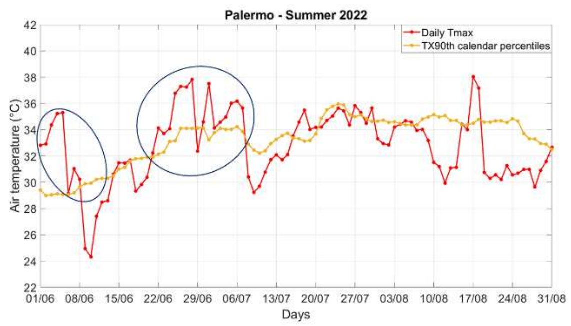

(e)

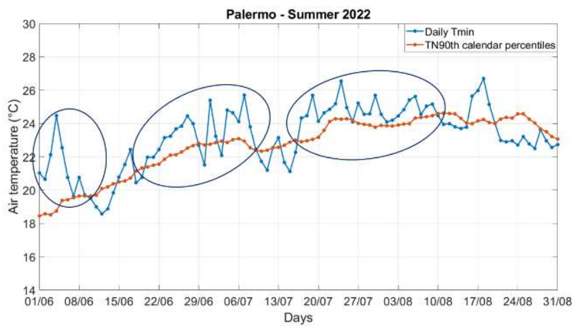

(f)

Figure 6.3. a), c) and e): Comparison between T_X trends during the summer of 2022 and the corresponding TX90th calendar percentile thresholds. b), d) and f):Comparison between T_N trends during the summer of 2022 and the corresponding TN90th calendar percentile thresholds.

Figure 6.3 also highlights sequences of days that were not classified as heat waves because they consist of only five consecutive days above the threshold; these intervals are marked with magenta circles. Figure 6.3 further confirms a well-known characteristic of HWs, namely their spatially extensive nature. Both diurnal and nighttime heat wave events affected all three analyzed locations simultaneously. An exception is observed in Palermo, where a nighttime heat wave occurred that was not detected in the other two locations and was not associated with a corresponding diurnal heat wave.

For completeness, the values of the WSDI and TX90p are computed for all summers during which HWs were identified. The TX90p index, included among the ETCCDI climate indices, represents the percentage of days in which daily maximum temperature exceeds the TX90th calendar percentile threshold. Table 6.2 summarizes the values of these two indices for each of the three locations.

Table 6.2. WSDI and TX90p evaluated for summers with at least one diurnal heat wave in Sicily

Summer	Site	Diurnal HWs	TX90p (%)	WSDI
2017	CT	1	21.7	9
	ME	1	18.5	8
	PA	1	22.8	11
2019	CT	1	19.6	7
	ME	0	15.2	0
	PA	1	23.9	9
2021	CT	2	30.4	21
	ME	3	31.5	27
	PA	3	33.7	17
2022	CT	2	22.8	19
	ME	1	20.7	9
	PA	2	45.7	24
2023	CT	1	18.5	13
	ME	1	20.7	16
	PA	1	21.7	17

Table 6.3 presents the results of the WSDI-n index, introduced in the Methods section, which quantifies the number of days affected by nighttime heat waves. The table also reports the TN90p index, another ETCCDI indicator, representing the percentage of days on which the daily minimum temperature T_N exceeds the TN90th calendar percentile.

Table 6.3. WSDI-n and TN90p evaluated for summers with at least one nighttime heat wave in Sicily

Summer	Site	Nighttime HWs	TN90p (%)	WSDI-n
2015	CT	0	6.5	0
	ME	2	27.8	15
	PA	1	21.7	9
2017	CT	1	23.9	11
	ME	1	18.5	7
	PA	1	30.4	10
2019	CT	1	18.5	6
	ME	0	26.1	0
	PA	1	33.7	8
2020	CT	1	10.9	7
	ME	1	12.0	6
	PA	1	16.3	6
2021	CT	3	33.7	27
	ME	3	39.1	28
	PA	3	38	29
2022	CT	2	29.3	23

	ME	3	43.5	20
	PA	4	64.1	49
	CT	1	19.6	16
2023	ME	1	22.8	18
	PA	2	25	17

As outlined in the methodology, tropical nights are identified using the TR25 index to assess whether heat wave events are associated with elevated nighttime temperatures. Table 6.4 summarizes the number of tropical nights recorded during summers affected by heat waves for all three locations, while Figure 5 illustrates the specific calendar days on which tropical nights occurred.

Table 6.4. Number of tropical nights recorded for those summers in which there was at least one daytime heat wave

Summer	Site	TR25
	CT	8
2017	ME	17
	PA	10
	CT	0
2019	ME	23
	PA	5
	CT	8
2021	ME	33
	PA	11
	CT	3
2022	ME	36
	PA	15
	CT	9
2023	ME	24
	PA	11

The analysis shows that, although daytime heat waves are often associated with the occurrence of tropical nights, extended sequences of tropical nights can also arise independently of heat wave events. For instance, during the summer of 2019 in both Messina and Palermo, multiple consecutive tropical nights were recorded in periods not characterized by heat waves.

Prior to evaluating the effect of heat waves on electricity demand, linear regressions are performed on pairs of hourly demand values and the corresponding atmospheric variables—T_{2m}, RH, and SH. The slope of each regression line is used to quantify the percentage variation in demand associated with a unit change in T_{2m}, RH, and SH over annual and seasonal time frames. Table 6.5 presents the resulting slope estimates for the Palermo location.

Table 6.5. Slopes of the linear regression lines for the pairs of temperature-demand, humidity-demand for the Palermo location.

Year	Annual			Spring			Summer		
	%/ °C	%/ $\%_{RH}$	%/ g/kg	%/ °C	%/ $\%_{RH}$	%/ g/kg	%/ °C	%/ $\%_{RH}$	%/ g/kg
2015	0.8	-0.4	1.0	0.5	-0.3	-0.9	2.9	-0.4	3.3
2016	0.7	-0.3	0.8	0.3	-0.2	-0.7	1.9	-0.3	1.3
2017	0.8	-0.3	1.0	0.4	-0.2	-0.7	2.1	-0.4	2.1
2018	0.6	-0.3	0.8	0.1	-0.1	-0.5	2.0	-0.3	0.5
2019	0.9	-0.4	1.3	0.1	-0.1	-1.2	2.1	-0.3	1.9
2020	1.0	-0.4	1.6	0.1	-0.1	-1.5	2.5	-0.4	2.3

2021	1.3	-0.5	1.7	-0.1	-0.2	-3.1	2.7	-0.5	1.7
2022	1.1	-0.4	1.6	0.1	-0.2	-1.9	2.0	-0.3	0.4
2023	1.5	-0.7	1.8	0.8	-0.4	-2.2	3.5	-0.7	2.4

Table 6.5 corroborates the correlation analysis for the temperature–demand relationship, showing that the regression slope increases from spring to summer. Unlike the RH–demand relationship, the SH–demand pair exhibits a consistent slope sign across seasons. Results for Messina and Catania largely mirror those for Palermo, with the main exception being Catania, where the SH–demand slope changes sign across years and lacks seasonal consistency.

6.2.3 The impact of heat waves on energy demand

After identifying both diurnal and nighttime heat waves, electricity demand during these events is analyzed following the methodology described earlier. Only periods in which diurnal and nocturnal heat waves occur simultaneously and are common to all three locations are considered, since demand data are available at the regional (Sicily-wide) level. Electricity demand during heat wave periods is then compared with demand during equivalent periods outside heat waves. Table 6.6 reports the share of summer electricity demand occurring during heat wave and non–heat wave periods, along with the corresponding percentage change between the two conditions.

Table 6.6. Share of electricity demand during heat wave periods (Dem_{HW}) and non–heat wave periods (Dem_{noHW}) expressed as a percentage of total summer demand. The final column reports the percentage increase in energy demand when transitioning from non–heat wave to heat wave conditions.

Year	Period	$\mathrm{Dem_{HW/noHW}/Dem_{tot}}$ (%)	Delta (%)
2017	HW	15.5	16.2
	Outside HW	13.3	
2019	HW	8.6	-12.5
	Outside HW	9.8	
2021	HW	14.5	1.2
	Outside HW	14.3	
	HW	12.8	22.4
	Outside HW	10.5	
	HW	13.7	16.3
	Outside HW	11.8	
2022	HW	7.9	4.5
	Outside HW	7.5	
	HW	19.0	4.7
	Outside HW	18.2	
2023	HW	24.5	36.4
	Outside HW	17.9	

The results indicate that, with the exception of the summer of 2019, all identified heat wave events are associated with an increase in electricity demand relative to periods not affected by HWs. Notably, the largest demand increase occurs in the summer of 2023, even though this year does not exhibit the highest values of WSDI, WSDI-n, TX90p, or TN90p. The negative demand variation observed in

2019 can be explained by the timing of the heat wave, which took place in early June—a period typically characterized by lower electricity demand compared to later summer months. Consequently, heat wave events occurring in early June appear to have a limited impact on overall electricity demand.

Table 6.7 presents the results for summers in which nighttime heat waves occurred independently of diurnal heat waves, in all three Sicilian locations.

Table 6.7 Share of electricity demand during nighttime heat wave periods (Dem_{HW}) and outside these periods (Dem_{noHW}) expressed as a percentage of total summer demand. The final column shows the percentage change in demand from non–heat wave periods to nighttime heat wave periods

Year	Period	$\mathrm{Dem_{HW/noHW}/Dem_{tot}}$ (%)	Delta (%)
2020	HW	8.9	16.0
	Outside HW	7.7	
2022	HW	19.9	21.2
	Outside HW	16.4	

A comparison between Table 6.6 and Table 6.7 shows that nighttime heat waves lead to increases in electricity demand comparable to those observed during diurnal heat waves or periods when both diurnal and nighttime heat waves occur.

As in the annual and seasonal analyses described earlier, a simple linear regression is performed to evaluate the slope of the lines interpolating temperature–demand and humidity–demand pairs, both during heat wave periods and in their absence. Hourly electricity demand values are normalized with respect to the average hourly summer load, while meteorological data are considered separately for each location. Table 6.8 presents the regression slopes obtained using the meteorological data from Catania.

Table 6.8 Slopes of the linear regression lines for temperature–demand and humidity–demand pairs during periods encompassing heat waves common to all three Sicilian locations, based on meteorological data from Catania

Year		During HWs			Outside HWs		
		%/ °C	%/ $\%_{\mathrm{RH}}$	%/ g/kg	%/ °C	%/ $\%_{\mathrm{RH}}$	%/ g/kg
2017		1.5	-0.5	0.4	1.2	-0.2	-0.4
2019		0.8	-0.1	1.7	1.2	-0.2	0.9
2021	1	1.7	-0.4	-0.3	1.3	-0.3	-0.8
	2	1.4	-0.3	-0.2	1.4	-0.4	-2.9
	3	1.5	-0.5	-2.8	1.4	-0.3	-1.5
2022	1	1.1	-0.2	0.6	1.7	-0.3	-1.5
	2	1.4	-0.3	-0.1	1.1	-0.2	0.5
2023		2.6	-0.8	-4.8	1.7	-0.4	-3,5

The results in Table 6.8, along with those for Messina and Palermo, indicate that the impact of heat waves on electricity demand varies: depending on the specific event, the increase in demand with rising temperature can be greater or smaller than that observed during non–heat wave periods. Additionally, for all three locations, the regression slopes are largest in the summer of 2023.

The final analysis of this study focuses on assessing the hourly correlation between the atmospheric variables considered and electricity demand during heat wave periods, as well as outside of them. A daily correlation analysis is not performed, as the sample sizes would be insufficient to yield statistically meaningful results. Table 6.9 reports the results obtained with the meteorological data from Messina.

Table 6.9 Hourly correlation analysis results for the Messina location, comparing heat wave periods (HW) with periods outside heat waves (outside HW)

Year	Period	(T_{2m}, Dem)	(RH, Dem)	(SH, Dem)
2017	HW	0.53	-0.53	-0.42
	Outside HW	0.48	-0.54	-0.45
2019	HW	0.29	-0.10	0.19
	Outside HW	0.44	-0.32	-0.03*
2021	HW	0.59	-0.31	0.20
	Outside HW	0.49	-0.39	-0.11*
	HW	0.41	-0.29	-0.06*
	Outside HW	0.42	-0.46	-0.35
	HW	0.47	-0.39	-0.25
	Outside HW	0.53	-0.40	-0.08*
2022	HW	0.35	-0.19	0.09*
	Outside HW	0.64	-0.66	-0.54
	HW	0.50	-0.31	0.02*
	Outside HW	0.43	-0.28	0.02*
2023	HW	0.73	-0.61	-0.26
	Outside HW	0.63	-0.64	-0.45

*Correlations not statistically significant ($p > \alpha$)

As anticipated from the regression slope results, the strength of correlations during heat waves can be either weaker or stronger compared to periods without heat waves. Similar to the findings from the annual and seasonal hourly analyses, the relationship between SH and demand exhibits the highest proportion of statistically non-significant correlations.

6.3 Discussion and conclusions

The daily seasonal correlation analysis highlights two contrasting behaviors in the relationship between temperature and electricity demand. During spring, a negative correlation is observed, indicating that, on average, decreases in temperature are associated with increases in demand, and vice versa. In contrast, summer exhibits a positive correlation, confirming the intuitive expectation that higher temperatures lead to higher electricity demand. Moreover, the strength of the temperature–demand correlation increases substantially when moving from spring to summer, reaching values up to three times higher, and in some cases nearly an order of magnitude greater, depending on the year and the location.

On an annual basis, the positive correlation between temperature and demand suggests that the negative springtime correlation does not fully counterbalance the stronger positive summer correlation. Consequently, when averaged over the entire year, an increase in temperature is generally associated with an increase in electricity demand.

Relative humidity is physically and statistically inversely related to temperature: as temperature rises, relative humidity tends to decrease, resulting in a negative correlation between the two variables. As a consequence, when temperature and demand are positively correlated over a given time frame (annual or seasonal), relative humidity and demand are expected to exhibit a negative statistical correlation. This behavior is largely confirmed by the results of the present analysis. The only exception is the (RH, Dem_X) pair for the Catania location, where a positive correlation is observed. Conversely, the hourly correlation analysis consistently reveals a negative relationship between RH and electricity demand across all years and locations considered.

The statistically negative correlation observed between RH and electricity demand has important implications for modeling cooling demand based on RH. Although an increase in relative humidity hampers the human body's ability to dissipate heat, thereby increasing perceived temperature and potentially raising cooling demand, RH and electricity demand are statistically anti-correlated in the analyzed data. Consequently, a purely statistical approach that attempts to model increased cooling demand as a function of perceived temperature by directly incorporating RH (for instance through linear regression) may lead to misleading or incorrect results.

Consistent with the daily correlation analysis, the magnitude of the temperature–demand correlation increases markedly when moving from spring to summer periods, reaching values up to three times higher, and in some cases nearly an order of magnitude greater, depending on the year and the location. This behavior provides an indication of how much the use of cooling systems, both in residential and industrial sectors, affects electricity demand as temperatures increase. While in spring lower temperatures lead to a slight increase in demand, in summer rising temperatures cause a steeper increase in electricity demand. This shows that, for the case study analyzed, cooling systems have a greater impact than heating systems. Moreover, while cooling systems are typically electric, heating systems are not all electric. Therefore, the strong correlation between energy demand and temperature observed in summer directly reflects the behavior of residential and industrial users as temperatures rise above comfort levels.

The strong correlation observed between minimum temperatures and electricity demand highlights the relevance of nighttime thermal conditions. This behavior is further reinforced by the use of absolute thresholds, such as TRs, which show that minimum temperatures exceed both relative thresholds (e.g., TN90p) and absolute thresholds (e.g., TR25) more frequently than maximum temperatures exceed their corresponding thresholds (e.g., TX90p).

During spring periods, quantifying the relationship between humidity variables (both specific and relative humidity) and electricity demand proves to be statistically challenging. For all locations, both daily and hourly correlation analyses yield predominantly non-statistically significant results. This clearly indicates that demand models based on humidity variables and linear regression techniques are likely to perform poorly during spring, limiting their applicability in transitional seasons.

A pronounced temporal and spatial variability emerges from the analysis. For a given location and pair of variables, both the sign and magnitude of the correlation depend strongly on the selected time frame (annual, spring, or summer). Likewise, for a fixed time frame and variable pair, correlation strengths differ across locations. These findings indicate that a single linear regression model linking electricity demand to atmospheric variables cannot be considered universally valid, either across large geographical areas such as Sicily or across all seasons.

Another key result is that TRs may occur even in the absence of diurnal heat waves. This has important implications for EPS operation: forecasting reserve requirements based solely on daytime maximum temperatures would underestimate the risk of unmet demand. Grid operators should therefore account not only for daytime heat waves but also for nocturnal thermal stress.

The regression slopes describing the percentage change in demand with respect to temperature also vary from one HW to another, demonstrating that the impact of heat waves on electricity demand depends on the specific event and on the period of the summer in which it occurs. Among the characteristics of heat waves, their duration emerges as a critical factor in assessing EPS adequacy. This is exemplified by the summer of 2023, which exhibits the highest correlations between temperature and demand and the steepest demand–temperature slopes, despite not being the hottest summer in terms of standard heat wave indices (WSDI, WSDI-n, TX90p, TN90p). Notably, 2023 is characterized by the longest-lasting heat wave across all analyzed locations, highlighting the dominant role of persistence over intensity alone.

It is also interesting to conclude this section with some remarks on the possible evolution of demand in the coming years. In Italy, an increase in the installation of heat pumps is expected, which will lead to a shift in the main adequacy issues of the Italian power system increasingly from summer to winter. Moreover, peak loads are still expected to occur in summer [171]. Therefore, for future research, it would be of interest to also focus on winter, as it will be the season that, over the years, will show electricity demand increasingly influenced by lower temperatures.

7. Effect of correlated synthetic profiles of atmospheric variables on adequacy indices

Climate change can be defined as a statistically significant variation in the mean state of the climate or in its variability, with global warming representing one of its most prominent effects. Carbon dioxide emissions from human activities are the primary cause of the increase in average global temperatures observed over recent decades [3]. Within the EU, the energy supply and transport sectors are responsible for the largest shares of CO_2 emissions [14].

Despite this, GHG emissions from the energy sector have declined since 1990. By 2020, the amount of CO_2 emitted per kilowatt-hour of electricity produced had fallen to approximately half of its 1990 value. This substantial reduction has been enabled by the growing penetration of RESs in the EU energy mix [16]. Between 2009 and 2019, Europe experienced significant growth in PV power, wind power, and solid biofuel installations.

Over the same period, hydropower capacity increased only marginally, whereas PV technology exhibited the highest growth rate, rising from 1% (7.4 TWh) of installed capacity in 2008 to 13% (125.7 TWh) in 2019. This rapid expansion is largely attributable to the relative ease of deploying PV plants within EPSs. The increasing presence of RES in the EU-27 is further supported by environmental and energy policies, including the European Green Deal [13] and the REPowerEU Plan [137].

The increased deployment of RESs in generation mixes, together with the phase-out of coal, is contributing significantly to the achievement of the environmental targets set by the European Commission. However, renewable plants are inherently non-dispatchable, as their power output depends on meteorological variables that vary continuously over time. As a result, electricity generation from RES is more intermittent than that from conventional programmable sources, potentially undermining the ability to reliably meet electricity demand and posing risks to power system adequacy. Adequacy is defined as the capability of an EPS to satisfy electricity demand in every hour and in each market zone of a country [29]. From this perspective, an increasing share of RES can negatively affect adequacy levels, particularly because renewable generation often provides limited contributions during the most critical hours for adequacy. Several mitigation strategies have been proposed to address these challenges, including the deployment of energy storage systems to increase adequacy reserves [172], the strengthening of capacity market mechanisms [173], and the expansion of cross-border transmission lines to enhance mutual support among different market zones [174].

Regardless of the specific solutions adopted, adequacy analyses for future EPSs must be carried out on a probabilistic basis, given the stochastic nature of renewable generation driven by weather variability. The primary objective of adequacy analysis is to quantify both the amount of energy not supplied to loads over a year and the number of hours per year in which supply shortfalls occur. These quantities are commonly evaluated using the EENS and the LOLE indices, respectively.

In this chapter, statistical techniques are employed to synthetically generate weather variables, considering both independent and correlated formulations. A MC approach is adopted as the core algorithm to simulate weather variables starting from historical data. Among atmospheric variables, those of greatest interest for power system analyses are global solar radiation (GSR), precipitation (Pr), ambient air temperature (T_a), and wind speed (W). Accordingly, synthetic hourly profiles of these variables are generated. In the existing literature, several studies address the independent generation of these variables, whereas only a limited number of works—at least to the author's knowledge—focus on their correlated generation. From this perspective, the present study aims to advance the state of the art in the synthetic correlated generation of atmospheric variables through statistical methods, with specific application to power system adequacy analyses.

7.1 Stochastic generation of atmospheric variables

The synthetic generation of atmospheric variables represents the first step of the proposed adequacy analysis. A frequentist statistical framework is adopted to derive synthetic hourly profiles of the relevant weather variables, using ten years of historical meteorological data obtained from NASA's database [83]. The variables considered are global solar radiation (Wh/m^2), precipitation (mm/h), ambient air temperature (°C), and wind speed (m/s).

Several statistical techniques are employed to generate synthetically independent atmospheric variables, including standard MCSs, Bootstrapped Monte Carlo (BMC), and approaches based on the Pearson family of distributions. Seasonal effects and the associated annual cycles of the weather variables are explicitly modeled. The MC approach implemented in this study relies on the inverse transformation method, which requires the historical data to be fitted by an appropriate theoretical PDF.

Regarding the correlated generation of weather variables, the first step consists of performing a correlation analysis on the T_a–GSR and T_a–Pr pairs. These pairs are selected because of the strong relationship between ambient temperature and global solar radiation, and because temperature and precipitation significantly affect thermoelectric power production, which represents the largest share of the Sicilian generation mix.

Among the correlation measures available in the literature, Pearson's (P) and Spearman's (S) correlation coefficients are adopted in this study. The Pearson coefficient is used to quantify the sign and magnitude of the correlation between T_a and GSR, as these variables exhibit a predominantly linear relationship and P performs best under linear assumptions. Conversely, the Spearman coefficient is applied to the T_a–Pr pair, since their relationship is nonlinear; the S coefficient, being based on rank and monotonic dependence, is more suitable for capturing such nonlinear correlations. The expression for the Spearman coefficient is given by the following equation [175]:

$$r_s = 1 - \frac{6\sum D_i^2}{N(N^2 - 1)} \tag{7.1}$$

Where N is the total number of samples, and D_i is the difference between the i-th pair of ranked variables. An important advantage of r_s is that it is nonparametric.

The correlation values obtained from this analysis are then used to generate correlated marginal distributions of random numbers sampled from a multivariate gaussian distribution. These correlated random variables are subsequently employed to impose the desired correlation structure on the independently generated weather variables.

Once synthetic hourly profiles of GSR, Pr, T_a, and W are generated, both independently and with mutual correlations, the adequacy indices EENS and LOLE are evaluated. This is achieved by performing fifty sequential MCSs in order to obtain statistically meaningful results. The adequacy indices are then compared for the cases of correlated and independent weather variable generation. The Sicilian market zone is adopted as the reference case study, using installed generation capacity data and historical electricity demand profiles to model a single-bus power system for the simulations.

7.2 Component models of power systems and adequacy assessment

In this section, the power generation and electricity demand models are described; through these models, hourly generation and demand profiles are obtained.

7.2.1 Power output models of generation technologies

In PV systems, the generated power is approximately proportionally linear to solar irradiance when the system operates at its maximum power point (MPP) [176]. However, it should be emphasized that, in addition to solar radiation, other meteorological variables, such as wind speed and ambient air temperature, significantly affect PV efficiency and, consequently, power output [177]. In particular, PV power output depends on the cell temperature T_{cell} (°C), whose influence is quantitatively described by the power temperature coefficient α_{PV}, a parameter that depends on the specific PV cell technology. For monocrystalline silicon modules, α_{PV} typically ranges between −0.5 and −0.4 %/°C (e.g., α_{PV} = −0.5 %/°C is adopted in [28]). In this work, the equations used to model PV power production are taken from [28].

The power output of a generic wind turbine is modeled using its characteristic power curve to generate hourly wind power profiles. Wind turbine output depends on wind speed: for wind speeds below the cut-in speed v_{cut-in} (m/s), power production is zero; when wind speed exceeds the cut-off speed $v_{cut-off}$ (m/s), power output is also set to zero in order to protect the turbine from mechanical damage due to excessive wind. Let v_r (m/s) denote the rated wind speed at which the turbine delivers its nominal power. For wind speeds between v_r and $v_{cut-off}$, the power output remains equal to the nominal value, while for wind speeds between v_{cut-in} and v_r the power output follows a cubic dependence on wind speed. In this study, the characteristic wind speed values adopted are average values derived from the datasheets of 2 MW wind turbines [178]. All the considerations discussed above are formalized in the following equations:

$$P_{Out} = 0 \qquad if\ v < v_{cut-in}\ or\ v > v_{cut-off} \tag{7.2}$$

$$P_{Out} = P_{Out,n} \cdot \left(\frac{v - v_{cut-in}}{v_r - v_{cut-in}}\right)^3 \quad if\ v_{cut-in} < v < v_r \tag{7.3}$$

$$P_{Out} = P_{Out,n} \qquad if\ v_r < v < v_{cut-off} \tag{7.4}$$

where P_{Out} (W) is the power output of the wind turbine, and $P_{Out,n}$ (W) is the nominal power output of the wind turbine. The value of $P_{Out,n}$ adopted for the Sicily market zone is taken from [179].

Hourly power output profiles for thermoelectric plants are estimated using the model equations and parameters defined in [180]. However, modifications are introduced for the inlet water temperature and the water availability factor compared to [180]. The inlet water temperature model is based on a nonlinear regression equation from [181], relating the inlet water temperature (°C) to the ambient air temperature T_a (°C). For water availability, a nonlinear regression model similar to that in [181] is applied.

A nonlinear regression model mathematically similar to that of [181] is applied. In this study, an index ξ is introduced to quantify the availability of cooling water:

$$\xi = \varepsilon + \frac{\delta - \varepsilon}{1 + e^{\gamma(T_a - \beta_\xi)}} \tag{7.5}$$

Where ξ is the water availability factor (dimensionless), T_a is the ambient air temperature (°C), δ is the initial value of the water availability curve, related to hourly precipitation (dimensionless), β_ξ is the air temperature at the inflection point of the model curve (°C), and ε is the minimum value of the water availability factor (dimensionless, estimated), and γ $(1/°\mathrm{C})$ is the value of the steepest slope of the function. To model a linear behavior for most values of ambient temperature, for this study $\gamma = 1$ is set.

For hydroelectric power, the model used here is based on the installed capacity in the Sicily market zone, multiplied by the probability distribution of the plant's producibility index [179]. For a given time period (e.g., one year), the producibility index of a hydropower plant is defined as the ratio between the plant's producibility during that period and its average producibility over the same period [182]. Historically, the producibility index ranges between 0.7 and 1.4; in this study, values within this range are randomly generated using a uniform distribution with 0.7 and 1.4 as the lower and upper bounds.

7.2.2 Electricity demand model

Electricity demand represents the amount of electrical power required by the load at a given hour. Hourly demand depends on several factors, including the type of day (workday or public holiday), the season, and ambient air temperature which plays a crucial role in determining power requirements. In this study, all these influencing factors are explicitly modeled.

An "average seasonal day" is defined by selecting one representative non-holiday day in the middle of each season (e.g., 15 January for winter). The demand profile of this representative day is then replicated for all days within the corresponding season, thereby obtaining an average seasonal demand profile. Weekend demand is modeled by reducing the workday demand profile by 10%.

The impact of ambient air temperature on electricity demand is then incorporated by modifying the seasonal average demand profile according to the season, as follows. For winter, if the average hourly temperature exceeds the historical winter average, a 10% reduction in demand is applied; conversely, if the temperature is below the historical average, a 10% increase in demand is assumed. For summer, instead, the opposite behavior is modeled: a 10% increase in demand is applied when the average hourly temperature exceeds the historical summer average, while a 10% decrease is assumed when temperatures are below the seasonal average. Finally, for both spring and autumn, when hourly average temperatures are above their respective seasonal averages, a 5% increase in demand is simulated; when temperatures are below average, a 3% increase is applied.

The percentage variations adopted in this modeling framework are chosen arbitrarily. This is justified by the fact that the focus of the paper is not on the absolute values of the adequacy indices, but rather on their relative variation when atmospheric variables are synthetically generated independently or with mutual correlations.

7.2.3 Adequacy indices

The operation of an EPS is not limited to supplying electricity to end users; it must also comply with specific operational parameters and standards to ensure safe, resilient, and adequate system performance. With reference to adequacy, this concept is defined as the ability of an EPS to meet electricity demand in every hour and in each market zone of a country [29].

As reported in Chapter 2 to quantify the adequacy level of a given EPS, two widely adopted indices are used: the EENS, expressed in MWh, and the LOLE, expressed in hours. In this study, both the number of hours of inadequacy and the corresponding amount of energy not supplied are evaluated through hourly simulations covering all four seasons of the year, thereby representing a full annual cycle (8760 hours) and explicitly accounting for seasonal variability. The Time Step Simulation (TSS) tool available in the PowerWorld Simulator© is used to perform fifty simulations (i.e., fifty synthetic years), applied to the single-bus test system, considering both independently generated and correlated weather variables.

7.3 Results

The models described in Sections 7.2.1 and 7.2.2 are implemented with reference to the Sicily market zone and its power system as of 2020; however, the proposed methodology is general and can be applied to any market zone of interest. The installed generation capacities in 2020 are as follows:

5400 MW of thermoelectric generation (with no coal-fired plants), 716 MW of hydropower, 1921 MW of wind power, and 1474 MW of photovoltaic power [179].

Another aspect considered is the import and export capacity limits of the interconnection lines between the Sicily market zone and the Italian mainland (Calabria market zone). The import capacity limit—particularly relevant for adequacy assessments—is set to 700 MW from Calabria to Sicily, in accordance with [183]. Moreover, the interconnection capacity is assumed to remain unchanged until 2025. Consistently, the electricity demand data adopted in this study correspond to the preliminary projections for the target year 2025 released by ENTSO-E in the ERAA 2022 assessment [184].

Ten years of meteorological data, spanning the period 2007–2016, are considered. Probability distributions are fitted to these data, and the same data are then used for the correlation analysis. With regard to the choice of the geographical reference, Catania (CT) is selected as the representative location for the weather datasets, since a large share of the high-voltage transmission infrastructure and thermoelectric generation capacity in Sicily is located in its vicinity. The single-bus system adopted to simulate hourly import and export power flows is illustrated in Figure 7.1.

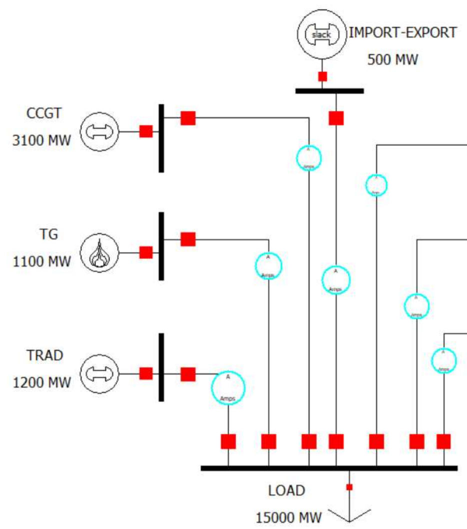

Figure 7.1. Single-bus grid implemented in the PowerWorld Simulator©. CCGT denotes Combined Cycle Gas Turbine, TG denotes Turbine Generator, and TRAD denotes Traditional generation.

Specifically, power imports and exports are simulated by modeling a generator as the system slack bus. Generator outages and transmission line outage rates are not considered in this study.

7.3.1 Stochastic profiles of atmospheric variables and correlation analysis

The results of the methodologies described in Section 7.1 for the synthetic generation of independent weather variables relevant to adequacy analyses are presented first. Based on the characteristics of the data, ambient air temperature and wind speed are modeled using normal and gamma distributions, respectively. For hourly GSR profiles, no satisfactory fit with a theoretical PDF is achieved; therefore, an empirical PDF and its corresponding CDF are constructed and used within the inverse method, with a final application of the BMC technique. Precipitation is synthetically generated using the Pearson distribution approach, with the mean, standard deviation, skewness, and kurtosis of the historical data as inputs. All the adopted procedures share a common random sampling stage, in which random numbers are drawn from a uniform distribution over the interval (0,1).

Figure 7.2 shows the histogram of the synthetically generated GSR, obtained using both the MC and BMC approaches, highlighting the good agreement between the synthetic distributions and the historical data.

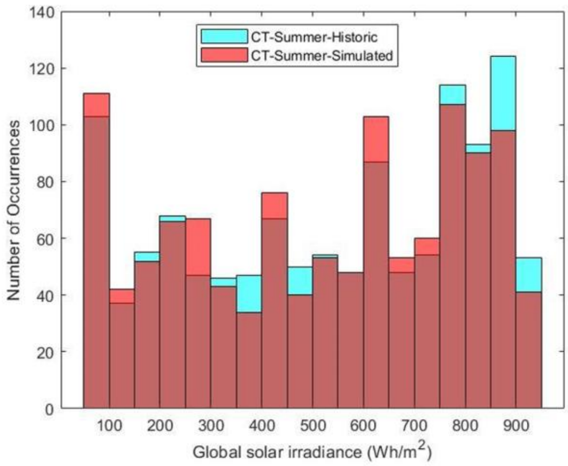

Figure 7.2. Comparison between the histograms of historical (cyan) and synthetically generated independent (red) GSR distributions for the CT location during summer.

Regarding the synthetic correlated generation, the procedure is applied to the pairs of variables identified in Section 7.1. Table 7.1 reports the correlation coefficients obtained from this analysis.

Table 7.1 Results of the correlation coefficient analysis for the CT case study

Correlation coefficient	Ta-GSR	Ta-Pr
Winter	0.64	-0.09
Spring	0.68	-0.26
Summer	0.73	-0.04
Autumn	0.61	-0.1

The results reported in Table 7.1 indicate that the correlation coefficients vary with the season for both variable pairs. The T_a–GSR pair exhibits a strong positive correlation, which is consistent with the physical relationship between ambient air temperature and global solar radiation, as temperature variations are largely driven by changes in irradiance (for example, the day–night cycle). Conversely, the T_a–Pr pair shows a negative correlation (anticorrelation), indicating that days with temperatures above the seasonal average tend to be associated with lower-than-average precipitation.

For completeness, Figure 7.3 illustrates how closely the synthetically generated T_a–GSR joint distribution matches the corresponding historical joint distribution.

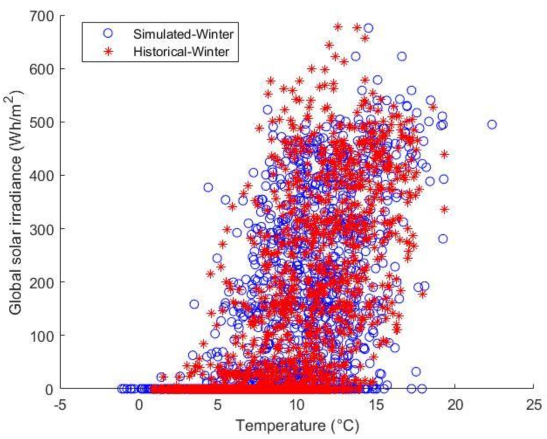

Figure 7.3. Comparison between the joint distributions of the historical (red stars) and synthetically generated correlated (blue circles) T_a–GSR pair for CT during winter.

7.3.2 Evaluation of adequacy indices for independent and correlated synthetic profiles

Considering the models described in Sections 7.2.1 and 7.2.2, synthetic profiles of energy production and demand are evaluated. With regard to thermoelectric generation and the modeling of the inlet water temperature, the regression curve for the Sicily market zone is defined. For this purpose, the maximum and minimum inlet water temperatures are set to 40°C and 1.5°C, respectively, while the air temperature at the curve's inflection point is set to 20°C. With regard to water availability, considering Equation (7.4), the following parameter values are fixed: δ varies linearly from 2 during intense precipitation (above 3.6 mm/h) to 0.8 when there is no precipitation; β_ξ is set to 35°C, and ε to 0.2.

Once the production and demand profiles are obtained, Monte Carlo simulations are run to evaluate the adequacy indices reported in Section 7.2.3. In this study, fifty MCSs are performed, each representing a generic year, to obtain statistically significant sets of EENS and LOLE values. To calculate these indices for each simulated year, the Net Transfer Capacity (NTC) of the interconnection lines must be considered, as it limits import and export power flows (obtained here using the TSS tool). By subtracting the actual flows from the NTCs, an annual hourly power deficit profile (8760 hours, in MW) is generated. Converting this profile to hourly energy (MWh), the system is considered inadequate in any hour where the energy deficit is greater than zero, with the corresponding energy not supplied to the loads. Figure 7.4 illustrates the annual hours of inadequacy for both independently generated and correlated weather variables. The focus on hours of inadequacy is justified because the ENS trends directly follow those of the inadequacy hours, as they are intrinsically linked.

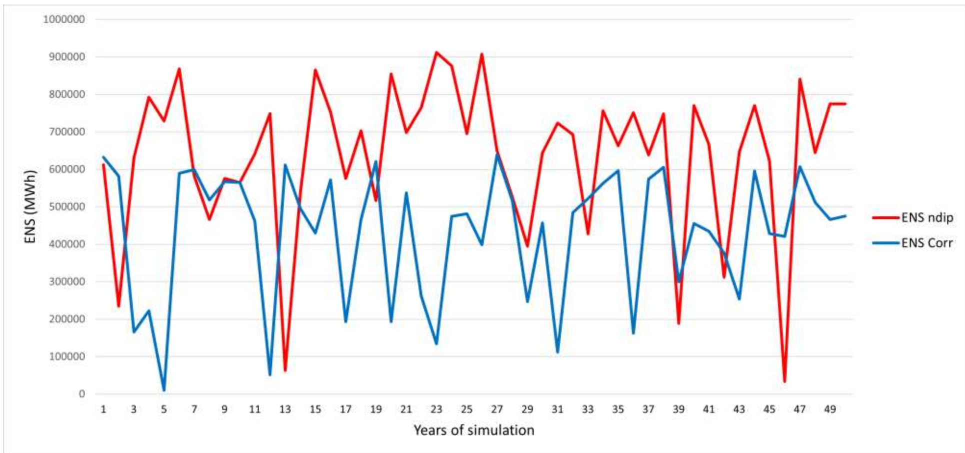

Figure 7.4. Trends in the annual hours of inadequacy across the fifty simulations (each representing a generic year), comparing independently generated weather variables (solid red line) with correlated weather variables (dashed blue line).

The difference between the two trends in Figure 7.4 highlights the impact of synthetically generating T_a-GSR and T_a-Pr as correlated variables on the adequacy analysis of the studied power system. Simulations using the correlated synthetic profiles of atmospheric variables result in fewer hours of inadequacy compared to simulations using meteorological variables generated independently of each other. Specifically, for independently generated variables, the LOLE and EENS values are 554 hours and 636,600 MWh, respectively, whereas for correlated variables, the LOLE is 381 hours, and the EENS is 433,000 MWh.

7.4 Final considerations

The different statistical methods used to synthetically generate independent weather variables produced hourly probability profiles that closely approximate the historical data.

A key novelty of this paper is the incorporation of correlations between weather variables into adequacy analyses. By applying Pearson's and Spearman's coefficients to the T_a–GSR and T_a–Pr pairs, the magnitude and direction of the correlations were quantified. Using these results, synthetic correlated weather variable profiles were generated, producing joint distributions that closely match historical data. Unlike most previous studies, these correlated weather profiles were used as inputs to the power generation models.

The generation models considered include both nonprogrammable renewable sources and fossil-fueled plants, while demand models and line transfer capacity constraints were also incorporated. Together, these factors provide a more refined adequacy analysis. However, generator and transmission line outage rates were not included. Future studies could enhance the analysis by modeling these failure rates probabilistically.

A novel water availability index is introduced in this study, which accounts for hourly precipitation (following a linear law) and varies with ambient temperature according to a nonlinear regression model.

Fifty simulations were conducted, each representing a generic year, using both independently and correlated generated weather variables. When correlated variables were used, significant differences were observed in LOLE, EENS, and trends in hours of inadequacy compared to the independent case. This demonstrates that the correlated generation of weather variables can notably influence adequacy analysis results. Future work could explore whether the impact of correlated weather generation depends on the specific variable pairs considered.

Overall, the results indicate that adequacy analyses should account for the correlated generation of weather variables that affect both power generation and electricity demand.

8. Final remarks

In this thesis, statistical methods were used to study the relationship between electricity demand and generation with atmospheric variables and to model the impacts of climate change on the adequacy of a power system. Adequacy is an aspect of power systems that involves not only energy generation plants, but also energy demand, as well as transmission network elements. The studies reported in this thesis therefore concerned the impacts of climate change on renewable energy production, on energy demand, and on network elements such as transformers. The methods used proved effective in modeling the randomness of the link between atmospheric variables and energy production and demand and power grid. In addition, a Monte Carlo algorithm was proposed to generate independent and correlated synthetic time series of atmospheric variables.

Specifically, it was observed that the correlation indices used made it possible to study the link between energy demand and atmospheric variables even during extreme heat events such as heatwaves. A Monte Carlo approach was then used to simulate the impacts of climate change on the production of an offshore turbine at three locations off the coast of Sicily. The generation of synthetic time series of wind speed made it possible to simulate hourly production profiles of the OWT, and this can be an integral part of an adequacy analysis for the evaluation of the relevant indices. The generation of synthetic temperature profiles then made it possible to model stochastic time series of transformer winding temperatures, proving to be a useful tool for simulating the randomness of temperature impacts on network components. An algorithm was then proposed for generating correlated time series of atmospheric variables. This algorithm, based on Monte Carlo methods such as the inverse transform method and bootstrapping, made it possible to observe how the results of adequacy indices change depending on whether atmospheric variables are generated stochastically as independent or correlated. This thesis work therefore shows how Monte Carlo methods can be used to refine the assessment of climate change impacts on the adequacy levels of a power system, compared to what is currently proposed in the state of the art of adequacy analyses.

For future research, climate change impact analyses could be conducted on hybrid systems such as offshore FPV and offshore wind. Concerning the methodology for generating correlated time series of atmospheric variables, it could be further refined by introducing autocorrelation into the stochastically simulated time series. The stochastic approach used could later be modified by considering measures of dependence between variables that are non-parametric and therefore do not require specific conditions to be optimally applied. Additionally, more climate models and emission scenarios could be used beyond those already employed in the studies of this thesis.

List of acronyms and symbols

ATR	Autotransformer
BMC	Bootstrapped Monte Carlo
CDF	Cumulative Distribution Function
CM	Climate Model
CPDF	Continuous Probability Distribution Functions
DTR	Dynamic Thermal Rating
EENS	Expected Energy Not Supplied
ENS	Energy Not Supplied
ENTSO-E	European Network of Transmission System Operators for Electricity
EPS	Electric Power System
ETCCDI	Expert Team on Climate Change Detection and Indices
EU	European Union
FPV	Floating Photovoltaic
GHG	Greenhouse Gas
GOF	Goodness-Of-Fit
HW	Heat Wave
ICDF	Inverse Cumulative Distribution Function
IPCC	Intergovernmental Panel on Climate Change
i.i.d.	independent and identically distributed
JJA	June, July, and August
χ^2	Chi-Square test
KS	Kolmogorov–Smirnov test
LOLE	Loss Of Load Expectation
MAM	March, April, and May
MC	Monte Carlo
MCS	Monte Carlo Simulation
MLE	Maximum Likelihood Estimation
ND-RES	Non-Dispatchable Renewable Energy Source
NMAE	Normalized Maximum Absolute Error
NRMSE	Normalized Root Mean Square Error
NTC	Net Transfer Capacity

OWT	Offshore Wind Turbine
P95	95th percentile
p	P-value
PDF	Probability Density Function
PM	Penman–Monteith
PV	Photovoltaic
R^2	Coefficient of determination
RES	Renewable Energy Source
SSP	Shared Socioeconomic Pathway
STD	Standard Deviation
TR	Tropical Night
TR25	Tropical Night (25°C threshold)
TS	Tap Staggering
TSO	Transmission System Operator
WSDI	Warm Spell Duration Index
WSDI-n	nocturnal WSDI

Funding

The author acknowledges that this thesis and the studies reported received financial support from the project PR FSE+ Sicilia 2021/2027 (AVVISO 1/2022) and fall within the framework of this project, grant number G61I22001350006.

Acknowledgments

A heartfelt thank you goes to my mother. Special thanks to my supervisor, Professor G. M. Tina, who allowed me to grow and transition from being a student to almost a researcher. It has also been wonderful, during these difficult years of sacrifice, to meet new souls, some of whom have become dear friends. An important and unexpected role was played by flowers. Over these three years, I discovered the true beauty of the Sunflower. I will always carry the cherished memory of this flower with me, wherever I go, wherever I am.

References

[1] WMO, "Climate," WMO, 2021. [Online]. Available: https://public.wmo.int/en/our-mandate/climate. [Accessed 23 11 2021].

[2] E. Ahlonsou, Y. Ding, D. Schimel, A.P.M. Baede, B. Bolin, S. Pollonais, "The Climate System: an Overview," IPCC, 2018.

[3] IPCC, "Climate Change 2021, The Physical Science Basis," IPCC, 2021.

[4] IEA- International Energy Agency, "Global Energy Review 2025 - CO2 emissions," 2025. [Online]. Available: https://www.iea.org/reports/global-energy-review-2025/co2-emissions. [Accessed 25 01 2025].

[5] British Petroleum, "BP Energy outlook 2020," BP, 2020.

[6] IRENA, "Renewable energy statistics 2021," IRENA, 2021.

[7] IRENA, "Renewable Capacity Statistics 2025," IRENA, 2025.

[8] Jacob D., Kotova L., Teichmann C., Sobolowski S.P., Vautard R., Donnelly C., Koutroulis A.G., Grillakis M. G., Tsanis I. K., Damm A., Sakalli A. van Vliet M.T.H., "Climate Impacts in Europe Under +1.5°C Global Warming," *AGU-Advancing Earth and Space Science,* vol. Earth's Future, no. 6, pp. 264-285 (https://doi.org/10.1002/2017EF000710), 2018.

[9] Panteli M., Mancarella P., "Influence of extreme weather and climate change on the resilience of power systems: Impacts and possible mitigation strategies," *Elsevier,* vol. Electric Power Sytems Research, no. 127, pp. 259-270 (http://dx.doi.org/10.1016/j.epsr.2015.06.012), 2015.

[10] J. Huisman, R. Martyr, R. Rott, J.. Smits, "Projections of climate change vulnerability along the Shared Socioeconomic Pathways 2020–2100," *Scientific Data,* vol. 12, no. 1, pp. 1527, (10.1038/s41597-025-05732-z), 2025.

[11] Zinaman, Owen, Miller, Mackay, Adil, Ali, Arent, Douglas, Cochran, Jaquelin, Vora, Ravi, Aggarwal, Sonia, Bipath, Minnesh, Linvill, Carl, David, Ari, Kauffman, Richard, Futch, Matt, Villanueva Arcos, Efraín, Valenzuela, José MarÃ Âa, Martinot, Eric et al, "Power Systems of the Future: A 21st Century Power Partnership Thought Leadership Report," *DOE-US Department of Energy,* pp. 1-53, (https://doi.org/10.2172/1171135), 01 02 2015.

[12] Craig Michael T., S. Cohen, Jordan Macknick, Caroline Draxl, Omar J. Guerra, Manajit Sengupta, Sue Ellen Haupt, Sue Ellen Haupt, Sue Ellen Haupt, "A review of the potential impacts of climate change on bulk power

system," *Elsevier,* vol. Renewable and Sustainable Energy Reviews, no. 98, pp. 255-267, (https://doi.org/10.1016/j.rser.2018.09.022), 2018.

[13] European Commision, "The European Green Deal," EU-Commission, 2019.

[14] European Environment Agency, "Greenhouse gas emissions by aggregated sector," 19 12 2019. [Online]. Available: https://www.eea.europa.eu/data-and-maps/daviz/ghg-emissions-by-aggregated-sector-5/#tab-dashboard-02. [Accessed 10 01 2022].

[15] European Environment Agency, "Greenhouse gas emission intensity of electricity generation in Europe," 18 11 2021. [Online]. Available: https://www.eea.europa.eu/ims/greenhouse-gas-emission-intensity-of-1. [Accessed 10 01 2022].

[16] Eurostat, "Renewable energy statistics," EU, 08 01 2022. [Online]. Available: https://ec.europa.eu/eurostat/statistics-explained/index.php?title=Renewable_energy_statistics. [Accessed 10 01 2022].

[17] Hydropower-Europe, "Hydropower in Europe," Hydropower-Europe-EU, 2020. [Online]. Available: https://hydropower-europe.eu/about-hydropower-europe/hydropower-energy/. [Accessed 10 01 2022].

[18] H. C. Bloomfield, D. J. Brayshaw, L. C. Shaffrey, P. J. Coker, H. E. Thornton, "Quantifying the increasing sensitivity of power systems to climate variability," *IOP Science,* vol. Environmental Research Letters, no. 11, pp. 1-12, (http://dx.doi.org/10.1088/1748-9326/11/12/124025), 2016.

[19] P.E. Bett, H. E. Thornton, "The climatological relationships between wind and solar energy supply in Britain," *Elsevier,* vol. Renewable Energy, no. 87, pp. 96-110, (https://doi.org/10.1016/j.renene.2015.10.006), 2016.

[20] K. van der Wiel, H. C. Boomfield, R. W. Lee, L. P., Stoop, R. Blackport, J. A. Screen, F. M. Selten , "The influence of weather regimes on European renewable energy production and demand," *IOP Science,* vol. Environmental Research Letters, no. 14, pp. 1-14, (https://doi.org/10.1088/1748-9326/ab38d3), 2019.

[21] K. van der Wiel, L.P. Stoop, B. R. H., van Zuijlen, R. Balckport, M.A. van der Broek, F.M. Selten, "Meteorological conditions leading to extreme low variable renewable energy production and extreme high energy shortfall," *Elsevier,* vol. Renewable and Sustainable Energy Reviews, no. 111, pp. 261-275, (https://doi.org/10.1016/j.rser.2019.04.065), 2019.

[22] M., Marinelli, P. Maule, A. N. Hahmann, O. Gehrke, P. B. Nørgard, N. A. Cutululis, "Wind and Photovoltaic Large-Scale Regional Models for Hourly Production Evaluation," *IEEE-Transactions on Sustainable Energy,* vol. 6, no. 3, pp. 916-923, (10.1109/TSTE.2014.2347591), 2015.

[23] Jakob Peter, "How does climate change affect electricity system planning and optimal allocation of variable renewable energy?," *Applied Energy,* vol. 252, no. 0306-2619, pp. 113397, (https://doi.org/10.1016/j.apenergy.2019.113397), 2019.

[24] A. I. Osman,, L. Chen, M. Yang,, G. Msigwa,, M. Farghali,, S. Fawzy, D. W. Rooney, P.-S. Yap, "Cost, environmental impact, and resilience of renewable energy under a changing climate: a review," *Environmental Chemistry Letters,* vol. 21, no. 2, pp. 741-764, (https://doi.org/10.1007/s10311-022-01532-8), 2023.

[25] Shankar N. Chandramowli and Frank A. Felder, "Impact of climate change on electricity systems and markets – A review of models and forecasts," *Sustainable Energy Technologies and Assessments,* vol. 5, no. 2213-1388, pp. 62-74, (https://doi.org/10.1016/j.seta.2013.11.003), 2014.

[26] Inès Harang and Fabian Heymann and Laurens P. Stoop, "Incorporating climate change effects into the European power system adequacy assessment using a post-processing method," *Sustainable Energy, Grids and Networks,* vol. 24, no. 2352-4677, pp. 100403, (https://doi.org/10.1016/j.segan.2020.100403), 2020.

[27] G.M. Tina, C.F. Nicolosi, "Assessment of the Impacts of Climate Change on Power Systems: The Italian Case Study," *MDPI,* vol. Applied Sciences, no. 11, pp. 1-28, (https://doi.org/10.3390/app112411821), 2021.

[28] Tobin I., Greuell W., Jerez S., Ludwing F., Vautard R., van Vliet M.T.H., Bréon F.M., "Vulnerabilities and resilience of European power generation to 1.5 °C, 2 °C and 3 °C warming," *IOP Science - Environ. Res. Lett.,* vol. 13, no. 4, pp. 1-9, ((https://doi.org/10.1088/1748-9326/aab211)), 2018.

[29] Terna, "Rapporto adeguatezza Italia 2021," Terna, Roma, 2021.

[30] FTI France S.A.S., Elering, "Study to Establish an Estonian Reliability Standard," FTI France S.A.S., 2020.

[31] R. Billinton, R. Karki, Y. Gao, D. Huang, P. Hu and W. Wangdee, "Adequacy Assessment Considerations in Wind Integrated Power Systems," *IEEE Transactions on Power Systems,* vol. 27, no. 4, pp. pp. 2297-2305, (doi: 10.1109/TPWRS.2012.2205022), 2012.

[32] G. Liu and P. Mancarella, "Adequacy Assessment of Renewables-Dominated Power Systems with Large-Scale Energy Storage," *2019 29th Australasian Universities Power Engineering Conference (AUPEC),* pp. pp. 1-6, (doi: 10.1109/AUPEC48547.2019.211877), 2019.

[33] S. Murphy, J. Apt, J. Moura, F. Sowell, "Resource adequacy risks to the bulk power system in North America," *Elsevier,* vol. Applied Energy, no. 212, pp. pp. 1360-1376, (https://doi.org/10.1016/j.apenergy.2017.12.097), 2018.

[34] Claudio F. Nicolosi, "MODELIZATION OF METEOROLOGICAL VARIABLES FOR ADEQUACY ANALYSIS OF RENEWABLES-BASED POWER SYSTEMS," Catania, Italy, Academic year 2020/2021.

[35] Franzese M., and Iuliano A., "Correlation analysis," in *Encyclopedia of bioinformatics and computational biology: ABC of bioinformatics*, Elsevier, 2018, pp. 706-721.

[36] Navidi, W. C., Statistics for engineers and scientists, New York: McGraw-Hill, 2011.

[37] V. Bewick, L. Cheek, J. Ball, "Statistics review 7: Correlation and regression," *Critical Care,* vol. 7, no. 6, pp. 451, (https://doi.org/10.1186/cc2401), 2003.

[38] Akoglu H., "User's guide to correlation coefficients," *Turkish Journal of Emergency Medicine,* vol. 18, no. 3, pp. 91-93, (https://doi.org/10.1016/j.tjem.2018.08.001), 2018.

[39] Majumder P., Ray P. P., "A systematic review and meta-analysis on correlation of weather with COVID-19," *Scientific Reports,* vol. 11, no. 1, pp. 1-10, (10.1038/s41598-021-90300-9), 2021.

[40] Battista G., de Lieto Vollaro R., "Correlation between air pollution and weather data in urban areas: Assessment of the city of Rome (Italy) as spatially and temporally independent regarding pollutants," *Atmospheric Environment,* vol. 165, pp. 240-247, (https://doi.org/10.1016/j.atmosenv.2017.06.050), 2017.

[41] Modoni G. E., Tosi D., "Correlation of Weather and Moods of the Italy Residents through an Analysis of Their Tweets," *2016 IEEE 4th International Conference on Future Internet of Things and Cloud Workshops (FiCloudW),* pp. 216-219, (10.1109/W-FiCloud.2016.53), 2016.

[42] Guan L., Yang J., Bell J. M:, "Cross-correlations between weather variables in Australia," *Building and Environment,* vol. 42, no. 3, pp. 1054-1070, (https://doi.org/10.1016/j.buildenv.2006.01.010), 2007.

[43] Berg, P. Haerter, J. O., Thejll P., Piani C., Hagemann S., Christensen, J. H., "Seasonal characteristics of the relationship between daily precipitation intensity and surface temperature," *Journal of Geophysical Research: Atmospheres,* vol. 114, no. D18, pp. 1-9, (https://doi.org/10.1029/2009JD012008), 2009.

[44] Tina, G.M.; Nicolosi, C.F.; Stefanelli, D., "The impacts of synthetic correlated generation of weather variables on adequacy analyses," *IEEE, AEIT International Annual Conference (AEIT),* vol. 2022, pp. 1-6; (10.23919/AEIT56783.2022.9951820), Rome, Italy, 3–5 October 2022.

[45] H. Bulut, O. Büyükalaca, "Simple model for the generation of daily global solar-radiation data in Turkey," *Elsevier - Applied Energy,* vol. 84, no. 5, pp. 477-491, (https://doi.org/10.1016/j.apenergy.2006.10.003), 2007.

[46] A. Linares-Rodríguez, J. A., Ruiz-Arias, D. Pozo-Vázquez, J. Tovar-Pescador , "Generation of synthetic daily global solar radiation data based on ERA-Interim reanalysis and artificial neural networks," *Elsevier - Energy,* vol. 36, no. 8, pp. 5356-5365, (https://doi.org/10.1016/j.energy.2011.06.044), 2011.

[47] G.M. Tina, C. Ventura, D. Stefanelli, "Meteorological probabilistic models for power system adequacy and resiliency assessment," *IEEE-Xplore-2020 AEIT International Annual Conference (AEIT),* pp. 1-6, (10.23919/AEIT50178.2020.9241093), 2020.

[48] Shu Geng, Frits W.T., Penning de Vries, Iwan Supit, "A simple method for generating daily rainfall data,," *Elsevier - Agricultural and Forest Meteorology,* vol. 36, no. 4, pp. 363-376, (https://doi.org/10.1016/0168-1923(86)90014-6), 1986.

[49] A. F. M. K. Chowdhury, N. Lockart, G. Willgoose, G. Kuczera, A. S. Kiem, N. Parana Manage, "Development and evaluation of a stochastic daily rainfall model with long-term variability," *Hydrol. Earth Syst. Sci.,* vol. 21, pp. 6541–6558, (https://doi.org/10.5194/hess-21-6541-2017), 2017.

[50] M. Dubrovsky, J. Buchtele, Z. Zalud, "High-Frequency and Low-Frequency Variability in Stochastic Daily Weather Generator and Its Effect on Agricultural and Hydrologic Modelling," *Springer - Climatic change,* vol. 63, pp. 145-179, (https://doi.org/10.1023/B:CLIM.0000018504.99914.60), 2004.

[51] R. Mehrotra, A. Sharma, "A semi-parametric model for stochastic generation of multi-site daily rainfall exhibiting low-frequency variability," *Elsevier - Journal of Hydrology,* vol. 335, no. 1-2, pp. 180-193, (https://doi.org/10.1016/j.jhydrol.2006.11.011), 2007.

[52] F. Chabane, N. Moummi, A. Brima, A. Moummi, "Prediction of the theoretical and semi-empirical model of ambient temperature," *Springer - Frontiers in energy,* vol. 10, pp. 268-276, (https://doi.org/10.1007/s11708-016-0413-y), 2016.

[53] H. Aksoy, Z. F. Toprak, A. Aytek, N. E. Ünal , "Stochastic generation of hourly mean wind speed data," *Renewable Energy,* vol. 29, no. 14, pp. 2111-2131, (https://doi.org/10.1016/j.renene.2004.03.011), 2004.

[54] R. Carapellucci, L. Giordano, "A methodology for the synthetic generation of hourly wind speed time series based on some known aggregate input data," *Elsevier - Applied Energy,* vol. 101, pp. 541-550, (https://doi.org/10.1016/j.apenergy.2012.06.044), 2013.

[55] B.Y.H. Liu, R.C. Jordan, "The interrelationship and characteristic distribution of direct, diffuse and total solar radiation," *Solar Energy - Elsevier,* vol. 4, no. 3, pp. 1-19, (https://doi.org/10.1016/0038-092X(60)90062-1), 1960.

[56] MathWorks, "Generate Correlated Data Using Rank Correlation," MathWorks, [Online]. Available: https://it.mathworks.com/help/stats/generate-correlated-data-using-rank-correlation.html. [Accessed 02 2022].

[57] MathWorks, "Copulas: Generate Correlated Samples," MathWorks, [Online]. Available: https://it.mathworks.com/help/stats/copulas-generate-correlated-samples.html. [Accessed 02 2022].

[58] X. Wang, D. Jiang, X. Lang, "Future changes in Aridity Index at two and four degrees of global warming above preindustrial levels," *International Journal of Climatology,* vol. 41, no. 1, pp. 278-294, (https://doi.org/10.1002/joc.6620), 2021.

[59] D. Carvalho, S. C. Pereira, R. Silva, A. Rocha, "Aridity and desertification in the Mediterranean under EURO-CORDEX future climate change scenarios," *Climatic Change,* vol. 174, no. 3, pp. 28, (https://doi.org/10.1007/s10584-022-03454-4), 2022.

[60] M. Sajid, I. Hassan, and A. Rahman, "An overview of cooling of thermoelectric devices," *Renewable and Sustainable Energy Reviews,* vol. 78, no. 1364-0321, pp. 15-22, (https://doi.org/10.1016/j.rser.2017.04.098), 2017.

[61] K. S. Hayibo, J. M. Pearce, "Foam-based floatovoltaics: A potential solution to disappearing terminal natural lakes," *Renewable Energy,* vol. 188, no. 0960-1481, pp. 859-872, (https://doi.org/10.1016/j.renene.2022.02.085), 2022.

[62] Y. Jin, S. Hu, A. D. Ziegler, L. Gibson, J. E. Campbell, R. Xu, D. Chen, K. Zhu, Y. Zheng, B. Ye, F. Ye, Z. Zeng, "Energy production and water savings from floating solar photovoltaics on global reservoirs," *Nature Sustainability,* vol. 6, no. 7, pp. 865-874, (https://doi.org/10.1038/s41893-023-01089-6), 2023.

[63] Maarten Dörenkämper and Arifeen Wahed and Abhishek Kumar and Minne de Jong and Jan Kroon and Thomas Reindl, "The cooling effect of floating PV in two different climate zones: A comparison of field test data from the Netherlands and Singapore," *Solar Energy,* vol. 219, no. 0038-092X, pp. 15-23, (https://doi.org/10.1016/j.solener.2021.03.051), 2021.

[64] C. D. Rodríguez-Gallegos, O. Gandhi, H. Sun, C. Paton, J. Zhang, J. M. Y. Ali, M. S. Alvarez-Alvarado, W. Zhang, C. A. Rodríguez-Gallegos, L. H. C. Chua, "Global floating PV status and potential," *Progress in Energy,* vol. 7, no. 1, pp. 1-41, (10.1088/2516-1083/ad9074), 2024.

[65] V. Ramasamy and R. Margolis, "Floating Photovoltaic System Cost Benchmark: Q1 2021 Installations on Artificial Water Bodies," National Renewable Energy Laboratory, NREL/TP-7A40-80695 (https://www.nrel.gov/docs/fy22osti/80695.pdf), Golden, CO, 2021.

[66] Nabil A.S. Elminshawy and Amr Osama and Antonio Gagliano and Erkan Oterkus and Giuseppe Marco Tina, "A technical and economic evaluation of floating photovoltaic systems in the context of the water-energy nexus," *Energy,* vol. 303, no. 0360-5442, pp. 131904, (https://doi.org/10.1016/j.energy.2024.131904), 2024.

[67] M.E. Taboada and L. Cáceres and T.A. Graber and H.R. Galleguillos and L.F. Cabeza and R. Rojas, "Solar water heating system and photovoltaic floating cover to reduce evaporation: Experimental results and modeling," *Renewable Energy,* vol. 105, no. 0960-1481, pp. 601-615, (https://doi.org/10.1016/j.renene.2016.12.094), 2017.

[68] Hamza Nisar and Abdul Kashif Janjua and Hamza Hafeez and Sehar shakir and Nadia Shahzad and Adeel Waqas, "Thermal and electrical performance of solar floating PV system compared to on-ground PV system-an experimental investigation," *Solar Energy,* vol. 241, no. 0038-092X, pp. 231-247, (https://doi.org/10.1016/j.solener.2022.05.062), 2022.

[69] Rodrigo Cáceres González and Cristóbal Sarmiento-Laurel and Hernán Alcayaga and Andrés J. Díaz and Alonso Pizarro and Juan Crespo Fuentes and Alicia Moya Caro and Camila Vásquez Páez and Fabián {Bustos Olavarría} and Roberta Boscolo and Hamid Bast, "Exploring climate-driven performance of floating photovoltaic systems: Energy production enhancement and evaporation reduction," *Applied Energy,* vol. 386, no. 0306-2619, pp. 125556, (https://doi.org/10.1016/j.apenergy.2025.125556), 2025.

[70] Lewis W. Farrar and AbuBakr S. Bahaj and Patrick James and Arif Anwar and Nafn Amdar, "Floating solar PV to reduce water evaporation in water stressed regions and powering water pumping: Case study Jordan," *Energy Conversion and Management,* vol. 260, no. 0196-8904, pp. 115598, (https://doi.org/10.1016/j.enconman.2022.115598), 2022.

[71] Zainab Akhtar and Mahendra Lalwani and K.V.S. Rao, "Estimation of energy potential and evaporation in 20 lakes with FPV in Rajasthan India," *Renewable Energy,* vol. 256, no. 0960-1481, pp. 124297, (https://doi.org/10.1016/j.renene.2025.124297), 2026.

[72] Hussain, Tanveer and Phillips, Tyler B. and Sun, Mucun and Gallego-Calderon, Juan, "Impact of Floating PV (FPV) System on Water Evaporation: Case Study of an Open Loop Reservoir in North Carolina," *2024 IEEE Kansas Power and Energy Conference (KPEC),* pp. 1-4, (10.1109/KPEC61529.2024.10676208), 2024.

[73] Ali Mahmoudi Aznaveh and Hossein Yousefi and Fatemeh Razi Astaraei, "Mitigating water evaporation and enhancing renewable energy with floating photovoltaic systems: An integrated approach to resource sustainability," *Energy Nexus,* vol. 21, no. 2772-4271, pp. 100683, (https://doi.org/10.1016/j.nexus.2026.100683), 2026.

[74] Javier Farfan and Christian Breyer, "Combining Floating Solar Photovoltaic Power Plants and Hydropower Reservoirs: A Virtual Battery of Great Global Potential," *Energy Procedia,* vol. 155, no. 1876-6102, pp. 403-411, (https://doi.org/10.1016/j.egypro.2018.11.038), 2018.

[75] Marc Perez and Richard Perez and Craig R. Ferguson and James Schlemmer, "Deploying effectively dispatchable PV on reservoirs: Comparing floating PV to other renewable technologies," *Solar Energy,* vol. 174, no. 0038-092X, pp. 837-847, (https://doi.org/10.1016/j.solener.2018.08.088), 2018.

[76] G. Kakoulaki and R. Gonzalez Sanchez and A. Gracia Amillo and S. Szabo and M. De Felice and F. Farinosi and L. De Felice and B. Bisselink and R. Seliger and I. Kougias and A. Jaeger-Waldau, "Benefits of pairing floating solar photovoltaics with hydropower reservoirs in Europe," *Renewable and Sustainable Energy Reviews,* vol. 171, no. 1364-0321, pp. 112989, (https://doi.org/10.1016/j.rser.2022.112989), 2023.

[77] Rocio Gonzalez Sanchez and Ioannis Kougias and Magda Moner-Girona and Fernando Fahl and Arnulf Jäger-Waldau, "Assessment of floating solar photovoltaics potential in existing hydropower reservoirs in Africa," *Renewable Energy,* vol. 169, no. 0960-1481, pp. 687-699, (https://doi.org/10.1016/j.renene.2021.01.041), 2021.

[78] Ciel et Terre, "Ciel et Terre - The floating solar company," 2025. [Online]. Available: https://ciel-et-terre.net/. [Accessed 2025].

[79] NRG Island, "NRG Island We design and build floating photovoltaic systems," 2025. [Online]. Available: https://www.nrgisland.com/. [Accessed 2025].

[80] Ocean Sun, "A bold solution to our global energy needs," 2025. [Online]. Available: https://oceansun.no/. [Accessed 2025].

[81] Monteith J. L., "Evaporation and environment," *Symposia of the society for experimental biology,* vol. 19, no. Cambridge University Press (CUP) Cambridge, pp. 205-234, 1965.

[82] Penman, H. L., "Natural evaporation from open water, bare soil and grass," *Proceedings of the Royal Society of London. A. Mathematical and Physical Sciences,* vol. 193, no. 1032, pp. 120-145, (10.1098/rspa.1948.0037), 1948.

[83] NASA Langley Research Center (LaRC) , "The POWER Project," 02 2024. [Online]. Available: https://power.larc.nasa.gov/.

[84] D.L. McJannet, I.T. Webster, M.P. Stenson, B.S. Sherman, "Estimating open water evaporation for the Murray-Darling Basin - A report to the Australian Government from the CSIRO Murray-Darling Basin Sustainable Yields Project," CSIRO, Australia, 2008.

[85] Abdelrady, Ahmed and Timmermans, Joris and Vekerdy, Zoltán and Salama, Mhd. Suhyb, "Surface Energy Balance of Fresh and Saline Waters: AquaSEBS," *Remote Sensing,* vol. 8, no. 7, pp. 1-17, (10.3390/rs8070583), 2016.

[86] Shaotao Fan and Zhaorong Ma and Tianhui Liu and Can Zheng and Hongqing Wang, "Innovations and development trends in offshore floating photovoltaic systems: A comprehensive review," *Energy Reports,* vol. 13, no. 2352-4847, pp. 1950-1958, (https://doi.org/10.1016/j.egyr.2025.01.053), 2025.

[87] Francesco Superchi and Riccardo Travaglini and Alessandro Bianchini, "Critical issues for the deployment of floating offshore hybrid energy systems comprising wind and solar: a case study analysis for the Mediterranean Sea," *Renewable Energy,* vol. 260, no. 0960-1481, pp. 125194, (https://doi.org/10.1016/j.renene.2026.125194), 2026.

[88] M. López, N. Rodríguez, G. Iglesias, "Combined Floating Offshore Wind and Solar PV," *Journal of Marine Science and Engineering,* vol. 8, no. 8, pp. 576, (10.3390/jmse8080576), 2020.

[89] Masson-Delmotte, V., P. Zhai, A. Pirani, S.L. Connors, C. Péan, S. Berger, N. Caud, Y. Chen, L. Goldfarb, M.I. Gomis, M. Huang, K. Leitzell, E. Lonnoy, J.B.R. Matthews, T.K. Maycock, T. Waterfield, O. Yelekçi, R. Yu, and B. Zhou (eds.), " IPCC, 2021: Summary for Policymakers. In: Climate Change 2021: The Physical Science Basis. Contribution of Working Group I to the Sixth Assessment Report of the Intergovernmental Panel on Climate Change," Cambridge University Press, Cambridge, United Kingdom and New York, NY, USA, pp. 3−32, doi:10.1017/9781009157896.001, 2021.

[90] G. M. Tina, C. F. Nicolosi, "Assessment of the Impacts of Climate Change on Power Systems: The Italian Case Study," *Applied Sciences,* vol. 11, no. 24, pp. 1-28, (10.3390/app112411821), 2021.

[91] "COMMUNICATION FROM THE COMMISSION TO THE EUROPEAN PARLIAMENT, THE EUROPEAN COUNCIL, THE COUNCIL, THE EUROPEAN ECONOMIC AND SOCIAL COMMITTEE AND THE COMMITTEE OF THE REGIONS The European Green Deal," European Commission, Brussels, 2019.

[92] IRENA, "Future of wind: Deployment, investment, technology, grid integration and socio-economic aspects (A Global Energy Transformation paper)," International Renewable Energy Agency, Abu Dhabi, 2019.

[93] T. Görmüş B. Aydoğan, B. Ayat, "Offshore wind power potential analysis for different wind turbines in the Mediterranean Region, 1959–2020," *Energy Conversion and Management,* vol. 274, no. 0196-8904, pp. 116470, (https://doi.org/10.1016/j.enconman.2022.116470), 2022.

[94] M. Majidi Nezhad, A. Heydari, M. Neshat, F. Keynia, G. Piras, D. A. Garcia, "A Mediterranean Sea Offshore Wind classification using MERRA-2 and machine learning models," *Renewable Energy,* vol. 190, no. 0960-1481, pp. 156-166, (https://doi.org/10.1016/j.renene.2022.03.110), 2022.

[95] M. Majidi Nezhad and M. Neshat and D. Groppi and P. Marzialetti and A. Heydari and G. Sylaios and D. Astiaso Garcia, "A primary offshore wind farm site assessment using reanalysis data: a case study for Samothraki island," *Renewable Energy,* vol. 172, no. 0960-1481, pp. 667-679, (https://doi.org/10.1016/j.renene.2021.03.045), 2021.

[96] D. Carvalho and A. Rocha and X. Costoya and M. deCastro and M. Gómez-Gesteira, "Wind energy resource over Europe under CMIP6 future climate projections: What changes from CMIP5 to CMIP6," *Renewable and Sustainable Energy Reviews,* vol. 151, no. 1364-0321, pp. 111594, (https://doi.org/10.1016/j.rser.2021.111594), 2021.

[97] V. Eyring, S. Bony, G. A. Meehl, C. A. Senior, B. Stevens, R. J. Stouffer, and K. E. Taylor, , "Overview of the Coupled Model Intercomparison Project Phase 6 (CMIP6) experimental design and organization," *Geosci. Model Dev.,* vol. 9, pp. 1937–1958, (https://doi.org/10.5194/gmd-9-1937-2016), 2016.

[98] H. Ezpeleta, A. Ulazia, G. Ibarra-Berastegi, J. Sáenz, S. Carreno-Madinabetia, O. Aristondo, "Future offshore wind energy evolution in the Bay of Biscay," *Sustainable Energy Technologies and Assessments,* vol. 65, no. 2213-1388, pp. 103776, (https://doi.org/10.1016/j.seta.2024.103776), 2024.

[99] E. Barkanov, M. Penalba, A. Martinez, A. Martinez-Perurena, A. Zarketa-Astigarraga, G. Iglesias, "Evolution of the European offshore renewable energy resource under multiple climate change scenarios and forecasting horizons via CMIP6," *Energy Conversion and Management,* vol. 301, no. 0196-8904, pp. 118058, (https://doi.org/10.1016/j.enconman.2023.118058), 2024.

[100] G. Esnaola, A. Ulazia, J. Sáenz, and G. Ibarra-Berastegi, "Future changes of global Annual and Seasonal Wind-Energy Production in CMIP6 projections considering air density variation," *Energy,* vol. 307, no. 0360-5442, pp. 132706, (https://doi.org/10.1016/j.energy.2024.132706), 2024.

[101] G. Kim and J. Hur, "Probabilistic modeling of wind energy potential for power grid expansion planning," *Energy,* vol. 230, no. 0360-5442, pp. 120831, (https://doi.org/10.1016/j.energy.2021.120831), 2021.

[102] J. C. Lee, and M. J. Fields, "An overview of wind-energy-production prediction bias, losses, and uncertainties," *Wind Energy Science,* vol. 6, no. 2, pp. 311-365, (10.5194/wes-6-311-2021), 2021.

[103] K. Kim, B. Kim, and H. Kim, "A decision-making model for the analysis of offshore wind farm projects under climate uncertainties: A case study of South Korea," *Renewable and Sustainable Energy Reviews,* vol. 94, no. 1364-0321, pp. 853-860, (https://doi.org/10.1016/j.rser.2018.06.061), 2018.

[104] C. Hübler, and R. Rolfes, "Analysis of the influence of climate change on the fatigue lifetime of offshore wind turbines using imprecise probabilities," *Wind Energy,* vol. 24, no. 3, pp. 275-289, (https://doi.org/10.1002/we.2572), 2021.

[105] Sadiah M.A. Aljeddani and M.A. Mohammed, "A novel approach to Weibull distribution for the assessment of wind energy speed," *Alexandria Engineering Journal,* vol. 78, no. 1110-0168, pp. 56-64, (https://doi.org/10.1016/j.aej.2023.07.027), 2023.

[106] A. Altamimi, P. P. Kesuma, "Long-term Reliability and Degradation Analysis of a Microgrid with Wind Farms Subjected to Climate Change Conditions and Age," *Arabian Journal for Science and Engineering,* vol. 48, no. 5, pp. 6577-6593, (https://doi.org/10.1007/s13369-022-07439-4), 2023.

[107] A. Bonou, A. Laurent, and S. I. Olsen, "Life cycle assessment of onshore and offshore wind energy-from theory to application," *Applied Energy,* vol. 180, no. 0306-2619, pp. 327-337, (https://doi.org/10.1016/j.apenergy.2016.07.058), 2016.

[108] A. C. Caputo, A. Federici, P. M. Pelagagge and P. Salini, "Offshore wind power system economic evaluation framework under aleatory and epistemic uncertainty," *Applied Energy,* vol. 350, no. 0306-2619, pp. 121585, (https://doi.org/10.1016/j.apenergy.2023.121585), 2023.

[109] Ki-Yong Oh and Woochul Nam, "A fast Monte-Carlo method to predict failure probability of offshore wind turbine caused by stochastic variations in soil," *Ocean Engineering,* vol. 223, no. 0029-8018, pp. 108635, (https://doi.org/10.1016/j.oceaneng.2021.108635), 2021.

[110] B. K. Saxena, K. V. S. Rao, "Comparison of Weibull parameters computation methods and analytical estimation of wind turbine capacity factor using polynomial power curve model: case study of a wind farm," *Renewables: Wind, Water, and Solar,* vol. 2, no. 1, pp. 1-11, (10.1186/s40807-014-0003-8), 2015.

[111] R. Liu, L. Peng, G. Huang, X. Zhou, Q. Yang, and J. Cai, "A Monte Carlo simulation method for probabilistic evaluation of annual energy production of wind farm considering wind flow model and wake effect," *Energy Conversion and Management,* vol. 292, no. 0196-8904, pp. 117355, (https://doi.org/10.1016/j.enconman.2023.117355), 2023.

[112] New European Wind Atlas, "New European Wind Atlas, a free, web-based application developed, owned and operated by the NEWA Consortium," NEWA Consortium, 2022. [Online]. Available: see www.neweuropeanwindatlas.eu, https://map.neweuropeanwindatlas.eu/about#terms-of-use. [Accessed 11 2025].

[113] Copernicus Climate Change Service, "Climate and energy related variables from the Pan-European Climate Database derived from reanalysis and climate projections. Copernicus Climate Change Service (C3S) Climate Data Store (CDS)," 20 09 2024. [Online]. Available: DOI: 10.24381/cds.f323c5ec. [Accessed 13 05 2025].

[114] A. S. Benabadji, K. Rahmoun, F. A. Bahar, A. Dahani, A. Martinez, and G. Iglesias, "Geospatial LCOE analysis for floating offshore wind energy in SW Mediterranean Sea," *Renewable Energy,* vol. 245, no. 0960-1481, pp. 122797, (https://doi.org/10.1016/j.renene.2025.122797), 2025.

[115] E. Faraggiana and A. Ghigo and M. Sirigu and E. Petracca and G. Giorgi and G. Mattiazzo and G. Bracco, "Optimal floating offshore wind farms for Mediterranean islands," *Renewable Energy,* vol. 221, no. 0960-1481, pp. 119785, (https://doi.org/10.1016/j.renene.2023.119785), 2024.

[116] G. Ferri and E. Marino, "Site-specific optimizations of a 10 MW floating offshore wind turbine for the Mediterranean Sea," *Renewable Energy,* vol. 202, no. 0960-1481, pp. 921-941, (https://doi.org/10.1016/j.renene.2022.11.116), 2023.

[117] A. Martinez and G. Iglesias, "Multi-parameter analysis and mapping of the levelised cost of energy from floating offshore wind in the Mediterranean Sea," *Energy Conversion and Management,* vol. 243, no. 0196-8904, pp. 114416, (https://doi.org/10.1016/j.enconman.2021.114416), 2021.

[118] M. Al-Khayat and M. AL-Rasheedi, "A new method for estimating the annual energy production of wind turbines in hot environments," *Renewable and Sustainable Energy Reviews,* vol. 195, no. 1364-0321, pp. 114343, (https://doi.org/10.1016/j.rser.2024.114343), 2024.

[119] J. F. Manwell, J. G. McGowan, A. L. Rogers, Wind Energy Explained: Theory, Design and Application, Copyright © 2009 John Wiley & Sons, Ltd, 2009.

[120] G. Amirinia, B. Kamranzad, and S. Mafi, "Wind and wave energy potential in southern Caspian Sea using uncertainty analysis," *Energy,* vol. 120, no. 0360-5442, pp. 332-345, (https://doi.org/10.1016/j.energy.2016.11.088), 2017.

[121] X. Yang, X. Jiang, S. Liang, Y. Qin, F. Ye, B. Ye, J. Xu, X. He, J. Wu, T. Dong, X. Cai, R. Xu, and Z. Zeng, "Spatiotemporal variation of power law exponent on the use of wind energy," *Applied Energy,* vol. 356, no. 0306-2619, pp. 122441, (https://doi.org/10.1016/j.apenergy.2023.122441), 2024.

[122] G. Li, A. Zhang, Q. Zhang, D. Wu, C. Zhan, "Pearson Correlation Coefficient-Based Performance Enhancement of Broad Learning System for Stock Price Prediction," *IEEE Transactions on Circuits and Systems II: Express Briefs,* vol. 69, no. 5, pp. 2413-2417, (10.1109/TCSII.2022.3160266), 2022.

[123] Claudio F. Nicolosi and Giuseppe Marco Tina, "Monte Carlo and bootstrap approaches for power system adequacy: a study on atmospheric variables correlations," *International Journal of Electrical Power & Energy Systems,* vol. 169, no. 0142-0615, pp. 110827, (https://doi.org/10.1016/j.ijepes.2025.110827), 2025.

[124] Claudio F. Nicolosi and Giuseppe Marco Tina, "Monte Carlo and bootstrap approaches for power system adequacy: a study on atmospheric variables correlations," *International Journal of Electrical Power & Energy Systems,* vol. 169, no. 0142-0615, pp. 110827, (https://doi.org/10.1016/j.ijepes.2025.110827), 2025.

[125] L. Guo, H. Wu, X. Yu, and T. Zhou, "Monte Carlo fPINNs: Deep learning method for forward and inverse problems involving high dimensional fractional partial differential equations," *Computer Methods in Applied Mechanics and Engineering,* vol. 400, no. 115523, pp. 115523, (https://doi.org/10.1016/j.cma.2022.115523), 2022.

[126] B. K. Kamel, A. Y. Abdelaziz, M. A. Attia, A. K. Khamees, "A novel approach to wind energy modeling in the context of climate change at Zaafrana region in Egypt," *Scientific Reports,* vol. 15, no. 1, pp. 7548, (https://doi.org/10.1038/s41598-025-90583-2), 2025.

[127] G. Abbas, A. Ali, M. T. B. Othman, M. W. Nawaz, A. U. Rehman, H. Hamam, "A novel energy pattern factor-based optimized approach for assessing Weibull parameters for wind power applications," *Scientific Reports,* vol. 15, no. 1, pp. 37, (https://doi.org/10.1038/s41598-024-80929-7), 2025.

[128] Fábio Sandro dos Santos and Kerolly Kedma Felix do Nascimento and Jader da Silva Jale and Sílvio Fernando Alves Xavier and Tiago A.E. Ferreira, "Brazilian wind energy generation potential using mixtures of Weibull distributions," *Renewable and Sustainable Energy Reviews,* vol. 189, no. 1364-0321, pp. 113990, (https://doi.org/10.1016/j.rser.2023.113990), 2024.

[129] Lin Da and Qingshan Yang and Min Liu and Ling Zhao and Teng Wu and Baolong Chen, "Estimation of extreme wind speed based on upcrossing rate of mean wind speeds with Weibull distribution," *Journal of Wind Engineering and Industrial Aerodynamics,* vol. 240, no. 0167-6105, pp. 105495, (https://doi.org/10.1016/j.jweia.2023.105495), 2023.

[130] W. Wang and T. Okaze, "Statistical analysis of low-occurrence strong wind speeds at the pedestrian level around a simplified building based on the Weibull distribution," *Building and Environment,* vol. 209, no. 0360-1323, pp. 108644, (https://doi.org/10.1016/j.buildenv.2021.108644), 2022.

[131] W. Wang, Y. Gao, N. Ikegaya, "Approximating wind speed probability distributions around a building by mixture weibull distribution with the methods of moments and L-moments," *Journal of Wind Engineering and Industrial Aerodynamics,* vol. 257, no. 0167-6105, pp. 106001, (https://doi.org/10.1016/j.jweia.2024.106001), 2025.

[132] E. Makalic, D. F. Schmidt, "Maximum likelihood estimation of the Weibull distribution with reduced bias," *Statistics and Computing,* vol. 33, no. 3, pp. 69, (https://doi.org/10.1007/s11222-023-10236-0), 2023.

[133] The MathWorks Inc., "MATLAB version: R2019a," The MathWorks Inc., (https://www.mathworks.com), Natick, Massachusetts, United States, 2019.

[134] NREL (National Renewable Energy Laboratory), "2020ATB_NREL_Reference_15MW_240," Alliance for Sustainable Energy, LLC, 2020. [Online]. Available: https://nrel.github.io/turbine-models/2020ATB_NREL_Reference_15MW_240.html. [Accessed 11 2025].

[135] NREL, "System Advisor Model™ Version 2025.4.16 (SAM™ 2025.4.16)," National Renewable Energy Laboratory, (https://https://sam.nrel.gov), Golden, CO, 2025.

[136] Terna - Snam, "Documento di Descrizione degli Scenari," Roma, 2022.

[137] European Commission, "COMMUNICATION FROM THE COMMISSION TO THE EUROPEAN PARLIAMENT, THE EUROPEAN COUNCIL, THE COUNCIL, THE EUROPEAN ECONOMIC AND SOCIAL COMMITTEE AND THE COMMITTEE OF THE REGIONS - REPowerEU Plan," Brussels, 2022.

[138] Terna, "2023 Development Plan Overview (in italian)," Terna S.p.A., Roma, 2023.

[139] C. Sigauke, M. M. Nemukula, "Modelling extreme peak electricity demand during a heatwave period: a case study," *Energy Systems,* vol. 11, no. 1, pp. 139-161, (10.1007/s12667-018-0311-y), 2020.

[140] Terna, "2023 Development Plan - State of the Electrical System," Terna S.p.A., Roma, 2023.

[141] Terna, "Incentivo per la riduzione dei costi di dispacciamento," Terna S.p.A., Roma, 2022.

[142] S. Quaia; A. Mauri; A. Marchesin; P. Manià, "Actions to Handle Increasing Distributed Generation and Rising Voltage during Low-Demand Periods: Tap Staggering Practices and Field Tests in the Italian Transmission Network," *Energies,* vol. 16, no. 6258, pp. 1-13, (https://doi.org/10.3390/en16176258), 2023.

[143] D. Wang, L. Chen, H. Li, Z. Wang, V. Turnham, "Impacts of tap stagger on currents of power transformers," *2017 IEEE PES Innovative Smart Grid Technologies Conference Europe (ISGT-Europe),* pp. 1-6, (10.1109/ISGTEurope.2017.8260204), 2017.

[144] A. Pasricha, M. L. Crow, "A method of improving transformer overloading beyond nameplate rating," *2015 North American Power Symposium (NAPS), Charlotte, NC, USA,* pp. 1-6, (10.1109/NAPS.2015.7335148), 2015.

[145] I. Daminov, A. Prokhorov, R. Caire, M.-C. Alvarez-Herault, "Assessment of dynamic transformer rating, considering current and temperature limitations," *International Journal of Electrical Power & Energy Systems,* vol. 129, no. 0142-0615, pp. 106886, (https://doi.org/10.1016/j.ijepes.2021.106886), 2021.

[146] Y. Wang, W. Tao, Z. Yan, R. Wei, "Uncertainty analysis of dynamic thermal rating based on environmental parameter estimation," *EURASIP Journal on Wireless Communications and Networking,* vol. 2018, no. 1, pp. 1-10, (https://doi.org/10.1186/s13638-018-1181-7), 2018.

[147] IEEE standards association, "IEEE Guide for Loading Mineral-Oil-Immersed Transformers and Step-Voltage Regulators," IEEE, 3 Park Avenue, New York, NY 10016-5997, USA, 2012.

[148] J. Myung, "Tutorial on maximum likelihood estimation," *Journal of Mathematical Psychology,* vol. 47, no. 1, pp. 90-100, (https://doi.org/10.1016/S0022-2496(02)00028-7), 2003.

[149] I. Pobočíková, Z. Sedliačková, M. Michalková, "Application of Four Probability Distributions for Wind Speed Modeling," *Procedia Engineering,* vol. 192, no. 1877-7058, pp. 713-718, (https://doi.org/10.1016/j.proeng.2017.06.123), 2017.

[150] Shcherbakov, M. V., Brebels, A., Shcherbakova, N. L., Tyukov, A. P., Janovsky, T. A., & Kamaev, V. A. E., "A survey of forecast error measures," *World applied sciences journal,* vol. 24, no. 24, pp. 171-176, 2013.

[151] IEC 60076-7, "Power transformers - Part 7: Loading guide for mineral-oil-immersed power transformers," INTERNATIONAL ELECTROTECHNICAL COMMISSION, 2018.

[152] IEA, "Renewables 2023 - Analysis and forecast to 2028," IEA - International Energy Agency, 2023.

[153] Engeland K., Borga M., Creutin J.-D., François B., Ramos M.-H., Vidal J.-P., "Space-time variability of climate variables and intermittent renewable electricity production – A review," *Renewable and Sustainable Energy Reviews,* vol. 79, no. 1364-0321, pp. 600-617, (https://doi.org/10.1016/j.rser.2017.05.046), 2017.

[154] Apadula F., Bassini A., Elli A., Scapin S., "Relationships between meteorological variables and monthly electricity demand," *Applied Energy,* vol. 98, no. 0306-2619, pp. 346-356, (https://doi.org/10.1016/j.apenergy.2012.03.053), 2012.

[155] Alberini, A., Prettico G., Shen C., Torriti J., "Hot weather and residential hourly electricity demand in Italy," *Energy,* vol. 177, no. 0360-5442, pp. 44-56, (https://doi.org/10.1016/j.energy.2019.04.051), 2019.

[156] Mirasgedis, S., Sarafidis, Y., Georgopoulou, E., Lalas, D.P., Moschovits, M., Karagiannis, F., Papakonstantinou, D., "Models for mid-term electricity demand forecasting incorporating weather influences," *Energy,* vol. 31, no. 2, pp. 208-227, (https://doi.org/10.1016/j.energy.2005.02.016), 2006.

[157] Staffell, I.. Pfenninger S., "The increasing impact of weather on electricity supply and demand," *Energy,* vol. 145, no. 0360-5442, pp. 65-78, (https://doi.org/10.1016/j.energy.2017.12.051), 2018.

[158] hing-Lai Hor, Watson, S.J., Majithia, S., "Analyzing the impact of weather variables on monthly electricity demand," *IEEE Transactions on Power Systems,* vol. 20, no. 4, pp. 2078-2085, (10.1109/TPWRS.2005.857397), 2005.

[159] Thornton, H. E., Scaife, A. A., Hoskins, B. J., Brayshaw, D. J., "The relationship between wind power, electricity demand and winter weather patterns in Great Britain," *Environmental Research Letters,* vol. 12, no. 6, pp. 1-11, (10.1088/1748-9326/aa69c6), 2017.

[160] Aisyah, S., and Simaremare, A. A., "Correlation between Weather Variables and Electricity Demand," *Conf. Ser.: Earth Environ. Sci.,* vol. 927, pp. 1-6, (10.1088/1755-1315/927/1/012015), 2021.

[161] Bartos, M. D., Chester, M. V., "Impacts of climate change on electric power supply in the Western United States," *Nature Climate Change,* vol. 5, no. 8, pp. 748-752, (10.1038/nclimate2648), 2015.

[162] Abdin, A.F., Fang, Y.-P., Zio E., "A modeling and optimization framework for power systems design with operational flexibility and resilience against extreme heat waves and drought events," *Renewable and Sustainable Energy Reviews,* vol. 112, no. 1364-0321, pp. 706-719, (https://doi.org/10.1016/j.rser.2019.06.006), 2019.

[163] Burillo, D., Chester, M. V., Ruddell, B., Johnson, N., "Electricity demand planning forecasts should consider climate non-stationarity to maintain reserve margins during heat waves," *Applied Energy,* vol. 206, pp. 267-277 (https://doi.org/10.1016/j.apenergy.2017.08.141), 2017.

[164] Pechan, A., and Eisenack, K., "The impact of heat waves on electricity spot markets," *Energy Economics,* vol. 43, no. 0140-9883, pp. 63-71, (https://doi.org/10.1016/j.eneco.2014.02.006), 2014.

[165] Sigauke, C., Nemukula, M. M., "Modelling extreme peak electricity demand during a heatwave period: a case study," *Energy Systems,* vol. 11, no. 1, pp. 139-161 (10.1007/s12667-018-0311-y), 2020.

[166] Perkins, S. E. , "A review on the scientific understanding of heatwaves—Their measurement, driving mechanisms, and changes at the global scale," *Atmospheric Research,* Vols. 164-165, no. 0169-8095, pp. 242-267, (https://doi.org/10.1016/j.atmosres.2015.05.014), 2015.

[167] Lionello P., Scarascia L, "The relation between climate change in the Mediterranean region and global warming," *Regional Environmental Change,* vol. 18, no. 5, pp. 1481-1493, (10.1007/s10113-018-1290-1), 2018.

[168] Notton G. , "Importance of islands in renewable energy production and storage: The situation of the French islands," *Renewable and Sustainable Energy Reviews,* vol. 47, no. 1364-0321, pp. 260-269, (https://doi.org/10.1016/j.rser.2015.03.053), 2015.

[169] ENTSO-E, "entso-e Transparency Platform," ENTSO-E, 2024. [Online]. Available: https://transparency.entsoe.eu/. [Accessed 02 2024].

[170] CCl/CLIVAR/JCOMM Expert Team (ET), "ETCCDI Climate Change Indices," Xuebin Zhang, 06 10 2020. [Online]. Available: https://etccdi.pacificclimate.org/index.shtml. [Accessed 03 2024].

[171] Terna, "Italy adequacy report 2025 (in italian)," Terna, Roma, 2026.

[172] A. Bagchi, L. Goel and P. Wang, "Adequacy Assessment of Generating Systems Incorporating Storage Integrated Virtual Power Plants," *IEEE Transactions on Smart Grid,* vol. 10, no. 3, pp. 3440-3451, (doi: 10.1109/TSG.2018.2827107), 2019.

[173] B. F. Hobbs, M. Hu, J. G. Inon, S. E. Stoft and M. P. Bhavaraju, "A Dynamic Analysis of a Demand Curve-Based Capacity Market Proposal: The PJM Reliability Pricing Model," *IEEE Transactions on Power Systems,* vol. 22, no. 1, pp. 3-14, (doi: 10.1109/TPWRS.2006.887954), 2007.

[174] Teng Zhao, Yizhe Jiang, Han Jiang, Yi Gao, Wei Wu, Chen Wang, Jinxiang Zhu, "Index system and methods for comprehensive assessment of cross-border power grid interconnection projects," *Global Energy Interconnection,* vol. 3, no. 6, pp. 532-544, (doi.org/10.1016/j.gloei.2021.01.006), 2020.

[175] Myers, Leann and Sirois, Maria J., "Spearman Correlation Coefficients, Differences between," *Wiley StatsRef: Statistics Reference Online,* pp. 1-13, (https://doi.org/10.1002/9781118445112.stat02802), 2014.

[176] M. A. Abdullah, Siti Fauziah Toha, Salmiah Ahmad, "Investigation on the Maximum Power Point in Solar Panel Characteristics Due to Irradiance Changes," *IOP Conf. Ser. ,* vol. Mater. Sci. Eng., no. 184, pp. 12-20, (doi:10.1088/1757-899X/184/1/012020), 2017.

[177] Perez J.C., Gonzalez A., Diaz J.P., Exposito F. J., Felipe J. , "Climate change impact on future photovoltaic resource potential in an orographically complex archipelago, the Canary Islands," *Elsevier,* vol. Renewable Energy, no. 133, pp. 749-759 (https://doi.org/10.1016/j.renene.2018.10.077), 2019.

[178] Vestas, "2 MW Platform," 2021. [Online]. Available: https://www.vestas.com/en/products/2-mw-platform. [Accessed 10 02 2022].

[179] Terna SpA, "Pubblicazioni statistiche," Terna, 06 2022. [Online]. Available: https://www.terna.it/it/sistema-elettrico/statistiche/pubblicazioni-statistiche. [Accessed 06 2022].

[180] B. Wang, Y. Zhou, P. Mancarella, M. Panteli, "Assessing the impacts of extreme temperatures and water availability on the resilience of the GB power system," *IEEE International Conference on Power System Technology (POWERCON),* pp. 1-6, (10.1109/POWERCON.2016.7754047), 2016.

[181] Mohseni O., Stefan H.G., Erickson T.R., "A nonlinear regression model for weekly stream temperatures," *AGU - Water Resources Research,* vol. 34, no. 10, pp. 2685-2692, (https://doi.org/10.1029/98WR01877), 1998.

[182] Terna, "Impianti idroelettrici," Roma, 1999.

[183] Terna, "Mercato della Capacità-Allegato 1 alla DTF n.2," Roma, 2022.

[184] ENTSO-E, "ERAA 2022 Call-for-Evidence on Preliminary Input Data," 03 2022. [Online]. Available: https://consultations.entsoe.eu/entso-e-general/eraa2022-call-for-evidence-preliminary-data-inputs/consult_view/. [Accessed 05 2022].